Experiments and theory of selective assembly using topography and ultrasonically-induced fluid forces

By
Sunghwan Jung

B.S. Mechanical Engineering
University of Iowa, 1993

M.S. Mechanical Engineering
Massachusetts Institute of Technology, 1995

SUBMITTED TO THE DEPARTMENT OF MECHANICAL ENGINEERING IN PARTIAL FULFILLMENT OF THE REQUIREMENTS FOR THE DEGREE OF DOCTOR OF PHILOSOPHY IN MECHANICAL ENGINEERING
AT THE
MASSACHUSETTS INSTITUTE OF TECHNOLOGY

FEBRUARY 2007

Signature of Author:_____
Department of Mechanical Engineering
September 28, 2006

Certified by:_____
Carol Livermore
Assistant Professor of Mechanical Engineering
Thesis Supervisor

Accepted by:_____
Lallit Anand
Chairman, Department Committee on Graduate Students

Experiments and theory of selective assembly using topography and ultrasonically-induced fluid forces

By
Sunghwan Jung

Submitted to the Department of Mechanical Engineering
on September, 2006 in Partial Fulfillment of the Requirements for the
Degree of Doctor of Philosophy in Mechanical Engineering

ABSTRACT

A site-selective self-assembly technique called templated assembly by selective removal (TASR) is introduced and demonstrated. A theory is created to describe its operation, and its correspondence with experiments is shown. In the experiments, the topography of the template is modified to match the shapes of micron-sized microsphere components at the locations where the components are intended to assemble; then the components and template are coated with a hydrophobic layer. The substrate and components are then placed in a fluid environment for the assembly process, and megahertz frequency ultrasound is applied to the fluidic bath to selectively remove components from undesired sites. Experiments successfully demonstrated highly selective assembly of the

microcomponents with the diameters in the range from 1.6 μm to 0.4 μm into the shape-matched holes in the template.

Based on the understanding of hydrophobic interfacial energy and the flow fields created by ultrasound, a theory was proposed to describe the mechanism of component removal and was carefully verified with additional experiments. In the present work, scalability and repeatability of the present approach were also addressed and experimentally investigated. Additionally, component circulation was qualitatively assessed in association with near-boundary acoustic streaming flow, and its contribution to the present assembly process is discussed.

Thesis Supervisor: Carol Livermore
Title: Experiments and theory of selective assembly using topography and ultrasonically-induced fluid forces

Table of Contents

List of Figures

List of Tables

Acknowledgment

First and foremost, I would like to thank Professor Carol Livermore, for her advice, guidance and supports on the presented research over the past four years. With her insight, enthusiasm and patience, she constantly supported me to be able to further explore challenging tasks, which sometimes led me to achieve invaluable results. Her extensive knowledge and skills in experimentations were invaluably useful for successfully completing my thesis. She also encouraged me to unboundedly utilize my previous skills and knowledge, which made my four years at MIT more exciting and meaningful time of my life.

Additionally, I would like to thank Professor Thomas Peacock and Professor Paula Hammond, members of my doctoral committees for their advices and comments on my works and thesis.

I would also like to thank Feras Eid and Hinmeng Au for being wonderful group mates all the while. I enjoyed conversations with them on a variety of topics, from which I widened my views on different cultures. Also, I am grateful to my friends in the Korean Graduate Student Association. I would like to specially thank Hyungil Lee, Junbeom Kim, Taejung Kim, Kontong Pahng, Hunwook Lim, Hyuksang Kwon, Chiwon Kim, Eunjong Hong, Sunho Park, Kyujin Cho, Jaejeen Choi and many more for their company. Without them, my life at MIT would have been half the experience.

I am also grateful to Professor Kwan Rim, Professor Nam Pyo Suh, and Professor Sang-Gook Kim for their supports and guidance in my study and career.

My last and the most precious thanks must go to my parents, Soyoung Jung and Soonam Cho. Without constant unbounded love and supports of my parents, none of this would have been possible. Also, I would like to thank my brother Dohwan Jung for his heartfelt supports. I am also indebt to my uncle, Chun Cho and my aunt, Sungja Moon for their constant supports ever since I came to US for the first time. Lastly, I would like to express deep appreciation to my beloved Jieha Lee, who constantly and unlimitedly supported me in many ways ever since we met.

1 Introduction

Miniaturization of devices to the micrometer or nanometer scale is challenging because of their many and varied functional requirements. In order to accommodate the need for small scale devices, micro- and nano manufacturing technology needs to enable a variety of system architectures. Conventional layer-by-layer, top-down approaches suffer from technical limitations such as chemical and thermal incompatibilities and, therefore, the variety of achievable architectures with the conventional technology is limited. As an alternative, assembly approaches in which components are fabricated separately and assembled in a final system have been proposed and extensively studied.[1-12]

Whereas serial assembly techniques are commonly used at the macroscopic scale, at the micro-scale, self assembly techniques operate in parallel and are more appropriate for mass manufacturing. Self assembly involves free energy minimization in a given potential field such as electrical, magnetic or molecular interaction field, which is relatively weak at the large scale but becomes significant at the micro-scale. This free energy minimization of self assembly allows autonomous and simultaneous arrangement of large numbers of microcomponents and also precise positioning of them by carefully tailoring the relevant potential fields. Many challenges of self assembly techniques still remain and will be addressed in the first part of this chapter. In the second part of this chapter, a

unique assembly technique that bridges mechanical force, 3D shape matching and surface chemistry is presented. This technique along with its quantitative description is the subject of this thesis.

1.1 Self Assembly

Creating systems of diverse nanocomponents is challenging for traditional top-down manufacturing because of the small size scale and commonly encountered thermal and chemical constraints. A variety of self assembly techniques have been created to address the challenge of creating small systems, and some representative examples are referenced here.[1-4,7,9-13] However, significant challenges still remain, especially for components that lie between the molecular scale, where chemistry offers a valuable level of control, and the macroscopic scale, where conventional manipulation techniques become possible. Selective incorporation of different types of components is critical for electronics (memory, logic, interconnects, displays), where including components with different functionalities is essential for system operation.[5,8,14] The ability to form arbitrary architectures (non-periodic arrays) is also critical for many electronic systems.

Self assembly of components into templates has been demonstrated at various scales. Some selectivity at each scale has been achieved, and self assembly shows the potential to

replace conventional top-down micro-fabrication when thermal and chemical constraints are encountered. At the meso-scale, from 100 μm to millimeters, many conventional mechanical forces have been adopted for the assembly of components into templates, and diverse architectures (even to 3D level) have been created. At the molecular scale, chemistry and biology have been successfully adopted for the assembly into templates. However, at the intermediate scales, from a few nanometers to 100 μm, self assembly is much more challenging because of uncertainties in intermolecular mechanisms, lack of control, and challenges of inspection and measurement at this scale. The uncertainties of this scale make self assembly much more challenging to achieve, although self assembly techniques are also potential and more beneficial at the intermediate because of the demands of diverse architectures.

Several examples of assembly at the intermediate scales are shown in Figure 1. 1.[1,2,4,12,15] Common elements include forces that promote adhesion (chemical adhesion, electrostatic forces, capillary force, etc), and geometric patterning to help guide the assembly. One example[15] of a periodic array by assembly shows that, in a controlled environment, uniform objects tend to order into array. Many of the forces adopted to drive the assembly process are relatively weak or short-ranged at the macroscopic scale, but

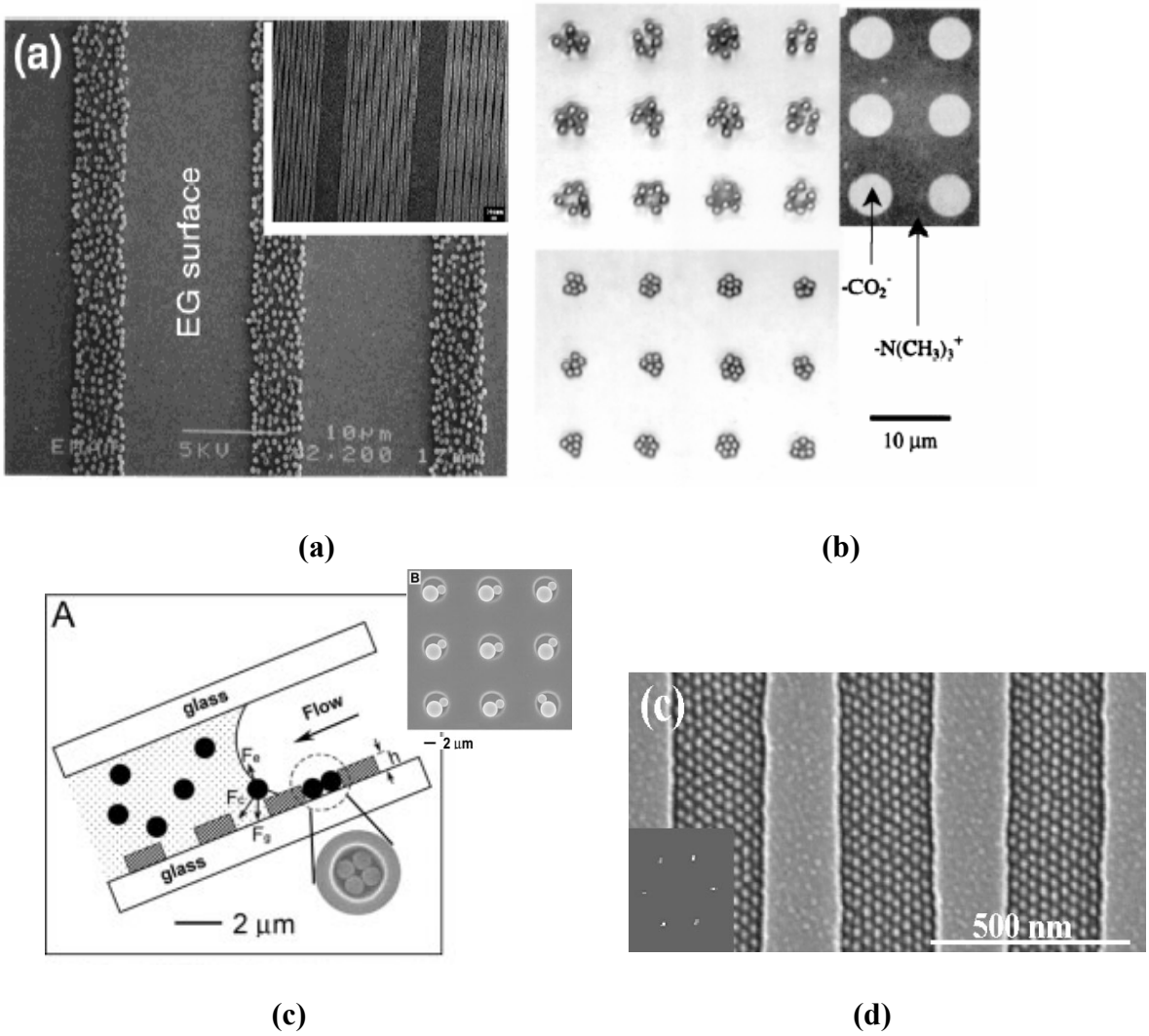

Figure 1. 1 Examples of self assembly at intermediate length scales. (a) Assembly of colloids onto patterned polyelectrolyte templates demonstrated by Chen et al. using electrostatic force and secondary interactions.[2] (b) Assembly of charged colloids onto patterned templates demonstrated by Aizenberg et al. using electrostatic force and capillary force.[1] (c) Assembly of colloids onto templates patterned with holes demonstrated by Xia et al. using capillary force and surface topography.[12] (d) Assembly of block co-polymer demonstrated by Cheng et al.[15] using spin casting a block co-polymer over surfaces patterned with grooves.

become significant at the intermediate scale. In the work of Chen *et al.*,[2] electrostatic and secondary interactions drive selective organization of microspheres onto those regions of a

substrate that are patterned with polyelectrolyte multilayer films. In the work of Aizenberg *et al.*,[1] electrostatic forces, which were introduced at binding sites, drive selective assembly of microspheres in a liquid; subsequently, during drying of the liquid, capillary forces precisely position the microspheres at the centers of the binding sites. In the work of Cheng *et al.*,[15] self assembly of block co-polymers is used to create periodic in-plane arrays of nanospheres with long range order. In the works of Xia *et al.*[12] and Cui *et al.*[4], capillary forces drag and pack microspheres into holes predefined on the surface of a template, and the number of microspheres packed in each hole is determined by the relative sizes of the microspheres and the holes. All the preceding works demonstrated some assembly capabilities at intermediate scale. However, practical applications require additional capabilities, such as precision, selectivity, scalability, compatibility, etc. Although individual self assembly techniques offer different subsets of these capabilities, there does not yet exist a self assembly approach that simultaneously offers all of them.

This work introduces a flexible, site selective self assembly technique that addresses many of these challenges. Called templated assembly by selective removal (TASR), it offers the ability to simultaneously assemble a diverse set of components into arbitrary, not necessarily periodic architectures. It offers a high degree of positional precision and the ability to locate multiple different types of components without the need for interlayer

alignment. The key elements of TASR are as follows. First, the topography of the substrate is modified to match the components' 3D shapes at the locations where the components are intended to assemble. Then, the substrate and components are coated with an adhesion promoter, such as a hydrophobic self assembled monolayer for adhesion in a water-based environment. The components and substrate are placed in a fluid environment for the assembly process, and megahertz frequency ultrasound is applied to the fluidic bath. Components contact the substrate randomly and adhere wherever they land. Components that are not in shape-matched sites are removed by fluid forces or torques induced by ultrasound. Very high frequency ultrasound is used to better interact with the tiny components by high inertial fluidic forces; in addition, megahertz frequency ultrasound offers good uniformity because it is not prone to cavitation. Figure 1. 2 shows a schematic diagram of the experimental set up for assembly by TASR and a schematic cross section of the patterned substrate and assembling components.

1.2 Work Scope

Firstly, the concept of the TASR approach is presented and the major elements of the approach are introduced and described. Then, the experimental implementation of the major elements into the assembly set-up is presented. Two types of experiments were

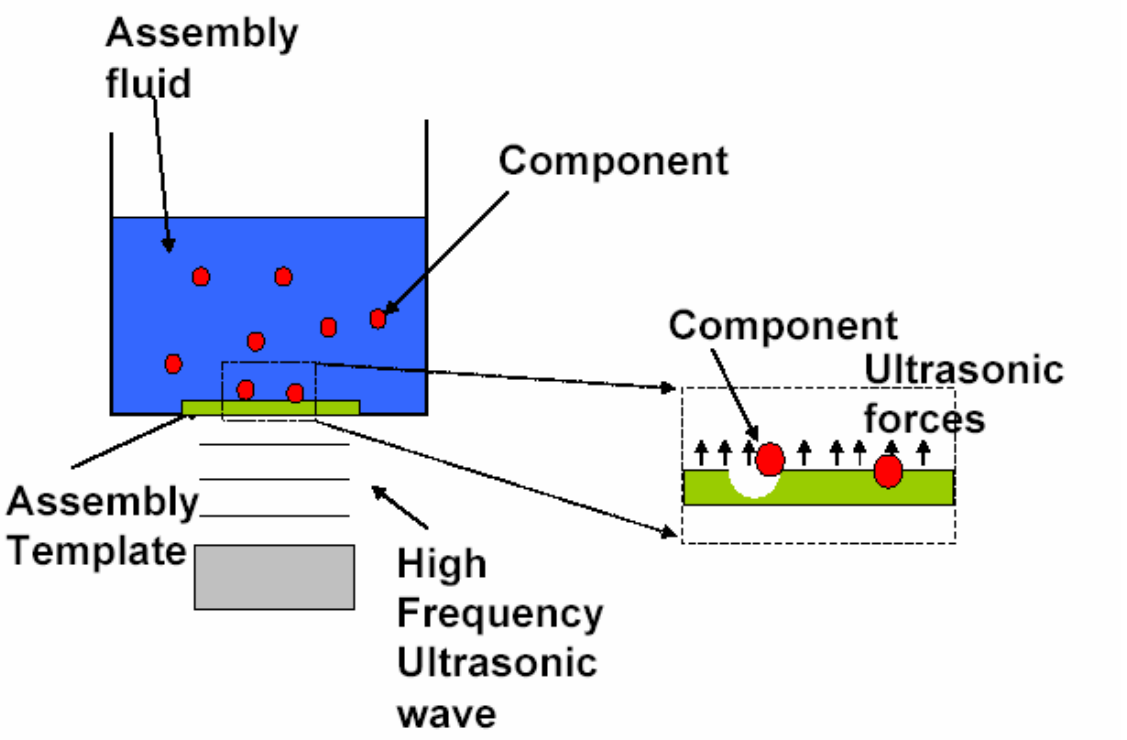

Figure 1. 2 Schematic diagram of TASR showing assembly setup and enlarged cross-sectional view of ultrasonic forces and substrate.

conducted. First, a preliminary experiment was conducted to prove the concept of the present assembly approach. Then, subsequent experiments were conducted to explore the limits of the approach. Preliminary experimental results successfully demonstrated the feasibility of the concept of selective removal by ultrasound. Based on the preliminary experimental observations, a theoretical model of the mechanism was presented to adequately describe the selectivity of the assembly. The subsequent experiments confirm the repeatability of the present assembly set-up and provide an extensive set of data with which to confirm validity of the theoretical model. The limits of the present approach and

the theoretical model were also addressed and explored with different assembly conditions, including components size variation and ultrasonic power variation.

Chapter 2 introduces basic concepts of the present approach, which are adhesion between a microsphere and a hole and fluidic forces induced by ultrasound. Chapter 3 presents template fabrication, microsphere preparation, and the design of the assembly system. Chapter 4 demonstrates the assembly results of the preliminary experiment, then, correlates the yield rates of the assembly to a quantified measured of the shape matching quality between a microsphere and a hole. Chapter 5 presents a selective removal theory with which to adequately describe the selectivity of the assembly and later addresses the scalability of the present approach. Chapter 6 validates the theory with results of additional experiments, investigates the repeatability of the assembly to estimate a statistical range of the data, and qualitatively assesses component circulation and its contribution to the assembly. Chapter 7 addresses limitations and remaining challenges of the present assembly.

2 Concept of templated assembly by selective removal

Templated assembly by selective removal places different types of components selectively into their proper sites on the patterned surface of a template with high positional precision and potentially low cost. In this chapter, the basic steps of this assembly approach are presented in order to provide a conceptual understanding of the approach. Also, the forces that can potentially be involved in the assembly and selective removal of small scale components are briefly addressed.

2.1 Basic steps of assembly

The TASR assembly approach is a series of steps in which components are guided to the surface, adhere to the surface, and are selectively removed from all but the correct locations on the surface. Each step is associated with a different combination of the key elements of fluidic forces, shape matching and surface chemistry. The fluidic forces are induced by ultrasound. The shape matching is set by the shape of the holes, which are complementary to the shapes of the target assembly components and are pre-created at the desired binding sites using lithography. The surface chemistry involves the interaction between the fluid in which assembly occurs and the adhesion-promoting self assembled

monolayer coating on the surfaces of the assembly components and the patterned templates. A different combination of these elements guides each step.

1) The guidance of assembly components to binding sites is provided by fluidic forces and shape matching. Fluidic forces circulate the assembly components and bring them into the binding sites (holes). Upon the arrival of the assembly component at the binding site, the shape match between the hole and the assembly component helps to precisely position the component in the hole. Excessive assembly components are used to avoid missing any binding sites.

2) The adhesion of the component to the hole is controlled by surface chemistry and shape match quality. Proper chemical coating on the surfaces of the components and the template tunes interfacial energy in association with the composition of the assembly fluid; higher interfacial energy induces stronger adhesion. The interfacial energy must be properly controlled to prevent adhesion between and aggregation of assembly components. Also, along with the interfacial energy, better shape match quality between the hole and the component determines the strength of adhesion.

3) The selective removal of the component from the hole is driven by the fluidic forces. If the fluidic effects are greater than the adhesive effects, the component is removed from the hole. In the work described here, shape match quality, surface chemistry and fluidic forces are carefully controlled to ensure that the adhesive effects are greater than the removal effects only for components in binding sites for which the hole shapes are well matched to the component shapes. Consequently, the removal is made selective; only those components that are poorly-matched to the holes are removed.

2.2 Surface-component adhesion

Self assembly between two specific objects occurs only when the free energy of the whole system after assembly is smaller than the free energy was before assembly, in which case the free energy reduction due to assembly creates adhesion between the objects. The free energy change by assembly is often presented in terms of free energy change per unit area and is known as the interfacial energy. The use of interfacial energy excludes the area change involved in the assembly.

In the present self assembly approach, the interfacial energy needs to be optimized for a successful demonstration of the assembly. The optimal value of the interfacial energy is achieved in the experiments by functionalizing the surfaces of assembly objects and

properly choosing the assembly fluid. First, silicon dioxide-coated wafers and micron-sized silica spheres are adopted for the template and assembly components, respectively. They are then functionalized with a self assembled monolayer (trichlorosilane-based) at their surfaces, which create adhesive forces based on hydrophobic effects in water-based solutions Figure 2. 1. The terminals (CH_3-) of the self assembled monolayer's long chain molecules are electrically neutral, leading to a higher interfacial energy with solutions containing polar water molecules and thereby to hydrophobic force. Hydrophobicity is driven by hydrogen bonding and entropic effects.[16] A hydrophobic surface (electrically neutral) cannot participate in hydrogen bonds, so water molecules will orient themselves around it to maximize the number of hydrogen bonds that they can make with neighboring water molecules. This orientational ordering is entropically unfavorable and is primarily

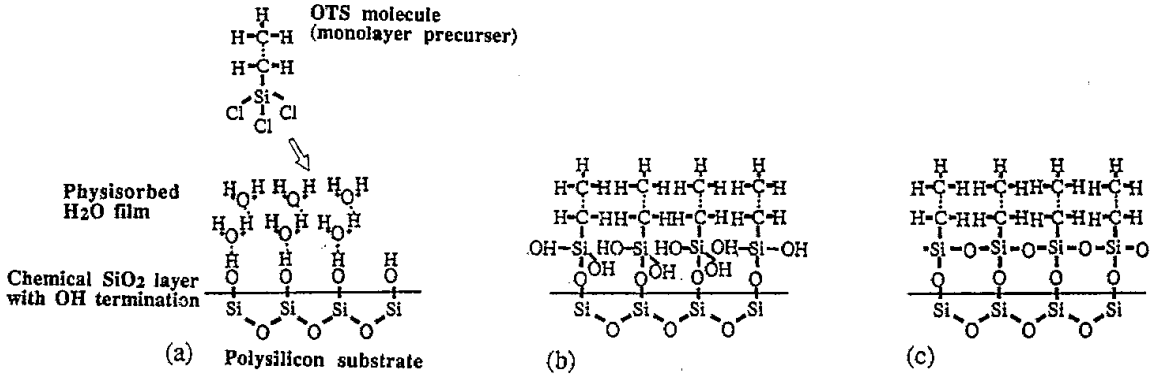

Figure 2. 1. Hydrophobic functionalization using trichlorosilane. (from [16]) (a) Hydrophilic oxide surface is covered with OH^- and a layer of water molecules before functionalization by trichlorosilane. (b) Trichlorosilane reacts with oxide and replaces Cl^- terminals with OH^-. (C) After OH^- groups condense to form H_20, a hydrophobic surface with terminals of CH_3 is created.

responsible for the high interfacial energy.

However, in the present assembly experiments, plain water solutions cannot be used because they lead to excessive aggregation of the hydrophobically-functionalized microspheres, which makes it impossible for the microspheres to be individually separated in the plain water solution for assembly. In order to prevent aggregation of microspheres, the idea of mixing water with acetone was proposed. Acetone molecules do not form hydrogen bonds with other acetone molecules, but they do form hydrogen bonds with water by "accepting" water's "donor" protons. By controlling the mixture ratio of water and acetone, the interfacial energy can be tuned to values greater than those arising from purely Van der Waals interactions, but less than those arising from hydrophobic interactions in pure water. With this tuning ability, the interfacial energy was optimized such that the interfacial energy was made small enough to prevent excessive aggregation of components, but still large enough to drive individual assembly of the microspheres to each designated hole. The interfacial energies of mixtures of water and acetone were estimated by contact angle measurements and adjusted by the method described by Adamson[17]. The details of calculation and measurement of the interfacial energy are presented in Chapter 3.

The idea of mixing water and acetone to control interfacial energy can be extended with other liquids as far as they can be mixed. For example, because water molecules are

polar, water can be mixed not only with acetone but also with ethanol, which has polar molecules. Ethanol is non-toxic and less volatile as compared to acetone. Therefore, mixtures with ethanol were used for real time observation of the assembly (see Chapter 6), where the container holding the assembly mixture is not sealed in order to let an immersed objective lens be placed inside the container.

2.3 Fluid removal forces

Megasonic excitation is employed to remove incorrectly-placed components from the template surface. Megasonic excitation is ultrasound applied at very high frequencies, in the megahertz range. A major application of megasonic excitation is to clean submicron particles off of semiconductor wafers. The high frequency regime is also above the cavitation threshold, and the lack of cavitation improves the spatial uniformity.

Megasonic excitation induces various ultrasonic forces that can potentially play a role in component removal. Depending on the incidence angle of the megasonic wave with respect to the template, fluid forces induced by the megasonic excitation on the template surface could have different directions and magnitudes. In the experimental set-up employed here, the assembly side of the template was set to face upward and away from the megasonic transducer (Figure 1. 3). In this set-up, some forces act perpendicularly to the

surface, so that they can lift objects directly off the surface; the perpendicular forces include the added mass force, stokes drag force, Basset force, and radiation force. Other forces act parallel to surface, so that they can roll or slide an object off the surface. In the present set-up, the acoustic streaming drag is the only parallel force. Acoustic streaming drags components due to a thin layer of continuous flow along the surface.[18] The acoustic streaming can potentially facilitate in-plane circulation of microspheres at the surface of the template because it rolls or slides the components along flat surfaces. The in-plane circulation increases the chance of components hitting the binding sites on the surface. This circulation issue will be discussed in more detail during the discussion of validation of the selective removal model.

3 Experimental procedure

This chapter presents the micro-fabrication procedures that are used to create patterns on the surface of the template and subsequently describes chemical coating procedures to render the surfaces of templates and microspheres hydrophobic. Also, the integration of the template, microspheres, assembly fluid and ultrasonic source into a functional experimental set up is illustrated and described.

3.1 Template fabrication and microsphere preparation

The template fabrication procedure used in these experiments is illustrated in Figure 3. 1. A silicon wafer is thermally oxidized to form a 1 μm thick silicon dioxide layer. This oxide layer is subsequently patterned using e-beam lithography (VS26, IBM) and a wet etch process; the platform of the e-beam lithography machine is only able to mount wafers 4 inches in diameter or smaller. Therefore, if the oxidized wafer is 6 inches in diameter, it is diced into four smaller pieces. For e-beam lithography, layers of 900k polymethylmethacrylate (PMMA) with thickness between 100nm and 200nm, depending on experiments, are spin coated onto the wafer and baked in an oven for 60 minutes at 200C. The spin speed is set to 500 rpm for the first 10 seconds and then set to 3000 rpm for 90 seconds. Various exposed spot sizes are defined in the PMMA using e-beam

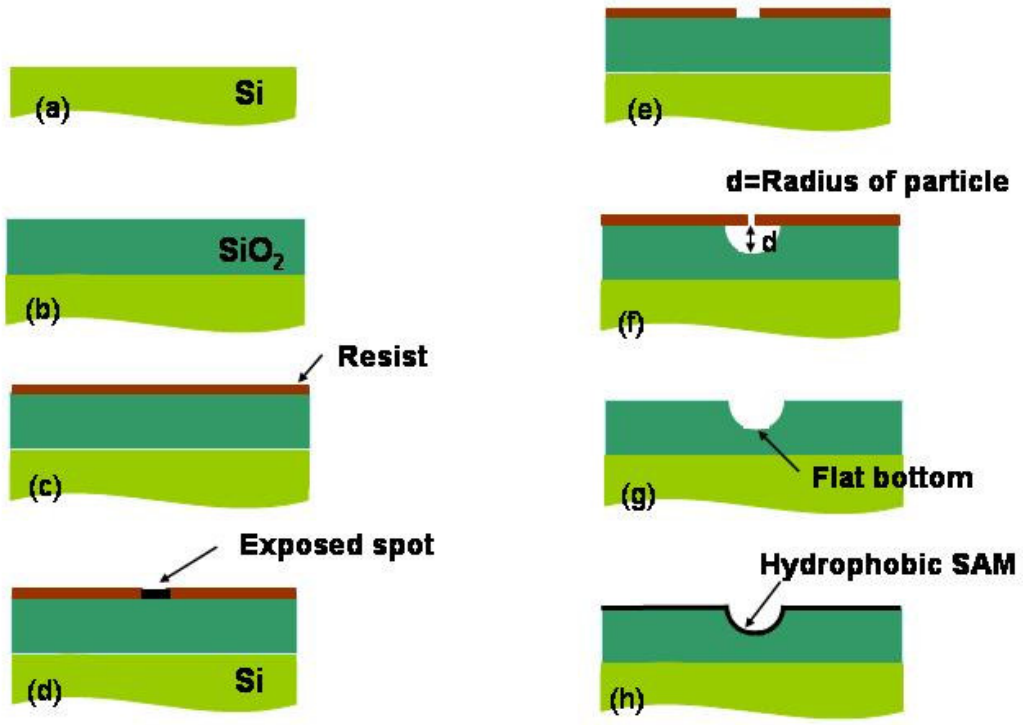

Figure 3. 1 Template fabrication procedure. (a) Bare silicon wafer. (b) Thermal oxidation. (c) Resist (PMMA) coating. (d) E-beam writing. (e) PMMA development. (f) Oxide isotropic etching. (g) PMMA strip. (h) Coating with a self-assembled monolayer

lithography. A pattern input is provided to the e-beam lithography machine in a KIC file format, which is generated by MATLAB subroutines[19]. In the subroutine, exposed spot size and spacing between spots are the variables to be defined and the whole set of the pattern is also repeatedly written by e-beam with a spacing of 5 mm to provide multiple templates for repeating assembly experiments with the (nominally) same template. The patterns of spot size and spot spacing varied from experiment to experiment to best

accomplish the purpose of each experiment, and specific patterns will be described in Chapter 4 and Chapter 6. In the e-beam writing step, spatial uniformity and maintaining good focus of the e-beam across the wafer surface are critical to the quality of the writing results. Therefore, the flatness of the wafer on the platform for the e-beam write needs to be thoroughly inspected and proved; even minimal tilting of the wafer greatly degrades spatial uniformity of focus. In the present e-beam writing set-up, for the inspection of flatness, the quality of focus was checked at every corner of the wafer, using a gold dot of a few millimeters that is placed there in order to guide the focusing. Also, the backside of wafer was inspected by eye for the presence of any PMMA residue, which would introduce significant tilting and needs to be removed to improve flatness.

After the e-beam write, the pattern is developed by a 90 second immersion in a 2:1 mixture of MIBK:IPA to expose the corresponding spots of the underlying oxide. The template is then immersed in degassed 7:1 buffered oxide etchant, which etches nominally isotropically out from the exposed oxide spots. The etch time (and hence the etch depth) are carefully controlled to ensure that the hole radius matches the microsphere radius. After etching, the smaller openings in the resist are converted to slightly flat-bottomed holes in the oxide as indicated in Figure 3. 1 (g). The larger the ratio of etch depth to the exposed PMMA spot size, the better the hole shape approximates a hemisphere. After

etching, the wafer is diced to separate it into nominally identical chips. The size of each chip (containing each whole set of the pattern) is 5mm by 5mm. Then the PMMA layer of each chip is removed with a 3:1 mixture of hydrogen peroxide and sulfuric acid. After the PMMA is stripped, the template is rinsed with water and then the water residue on the surface of the template is removed with an air gun. Subsequently, the template is dried in air inside a clean room for 5 minutes and immersed in toluene-based 10% octadecyltrichlorosilane solution for 30 minutes. Octadecyltrichlorosilane reacts with silicon dioxide, creating a hydrophobic monolayer. During the immersion, the solution containing the template is sonicated in order to prevent polymerization of octadecyltrichlorosilane on the surface of the template. Prevention of polymerization is necessary because octadecyltrichlorosilane is highly reactive with even trace amounts of water, creating polymerized structures. Then the template is removed from the solution and rinsed first with dichloromethane and subsequently with acetone.

For the assembly components, silica microspheres with diameters of 1.58μm +/-0.06 (Duke scientific), 0.88μm +/-0.0264 (Corpscular), and 432μm +/-0.0213 (Corpscular) are chosen and coated with toluene-based octyltrichlorosilane. Octyltrichlorosilane also produces a hydrophobic monolayer on top of silicon dioxide, but the hydrophobicity of the layer is less strong than that of octadecyltrichlorosilane-based layer because the has a

smaller number of -CH_2- groups (terminated with CH_3-) than the latter. The coating procedure for the silica microspheres is presented as follows.

1. Silica microspheres are precipitated from silica suspension (in a micro-tube) with a centrifuge (Microfuge 18 centrifuge, Beckman Coulter). The precipitates collect at the bottom of the tube.

2. Careful removal of the suspension liquid with a pipette starts from the top of the tube until only a minimal amount of the liquid residue is left on the microspehres precipitate at the bottom of the tube. Further removal of the liquid could remove microspheres.

3. Methanol or ethanol is added to the precipitated silica.

4. The silica suspension is stirred by vortex until the silica is fully dispersed in the liquid. (Vortex-Genie 2, Scientific Industries).

5. Repeat step 1-4 twice.

6. Silica microspheres are precipitated from the silica suspension (in a micro-tube) with the centrifuge.

7. The suspension liquid is removed.

8. The precipitated silica is placed in oven at 150 C for more than 12 hours in the tube.

9. Toluene-based (~15%) octyltrichlorosilane is added to the precipitated silica.

10. The silica suspension is stirred by vortex until it is fully dispersed.

11. The silica suspension is sonicated in a sonic bath for 30 minutes

12. Repeat step 1-4 three times, but with dichloromethane instead of methanol or ethanol.

13. Repeat step 1-4 three times, but with acetone instead of methanol or ethanol.

14. The silica microspheres are stored in acetone.

With this arrangement of surface coating, the adhesion between the silica microspheres is less strong than the adhesion between the silica microspheres and the template because the template surface is coated by octadecyltrichlorosilane, which produces a more hydrophobic layer than octyltrichlorosilane. This discriminate coating of the silica microspheres and the template is intended to maintain strong adhesion between the silica microspheres and template for the assembly while minimizing aggregation between the microspheres.

3.2 Design of assembly system

A schematic of the assembly system and a picture of the real set-up are demonstrated in Figure 3. 2. The chip, microspheres and assembly fluid are placed in an inner beaker (the assembly beaker). The assembly beaker is suspended directly above a 1.7 MHz ultrasonic transducer (MMDIT-1.7, Advanced Sonics) in a larger, water-filled outer beaker. The transducer's power is controlled by an input voltage from 0 to 120 volts by a variable

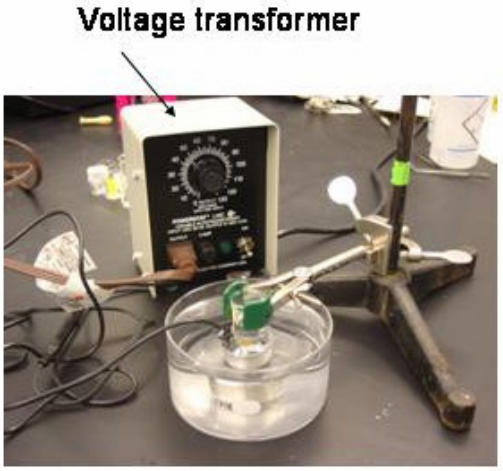

(a)

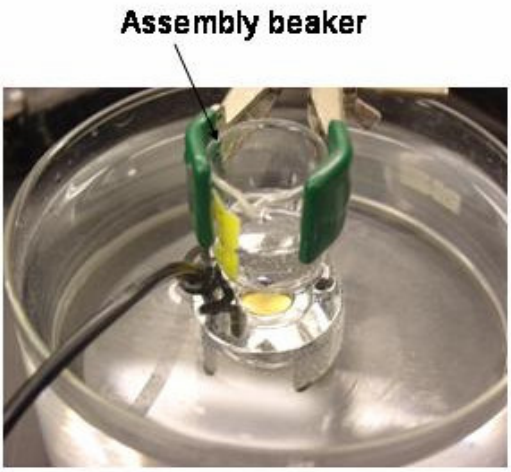

(b)

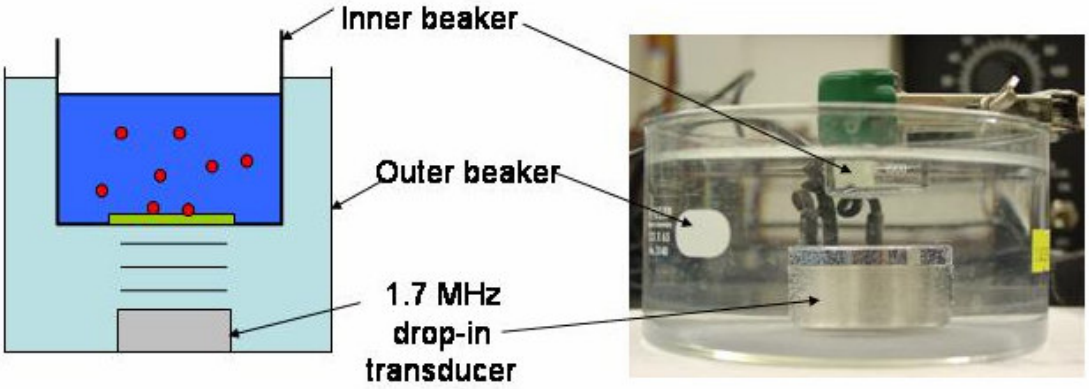

(c)

Figure 3. 2 Assembly system. (a) Overall view of assembly system set-up including voltage transformer. (b) Top view of the assembly beaker and transducer. (c) Schematic (left) and real set-up (right) of the assembly system.

voltage transformer (L10C, The Super Electronic Company).

The assembly beaker was filled with water and acetone; the water fraction ranges from 5% to 25%. The range of water fraction corresponds to interfacial energies between 5mJ/m^2 and 7mJ/m^2 as described in Section 3.3 and demonstrated in Figure 3. 3 The hydrophobically-coated chip was immersed in the assembly liquid (mixture of acetone and water) contained in the assembly beaker. Then, a dispersion of the hydrophobically-coated silica microspheres in acetone was dropped into the fluid of the assembly beaker using a pipette. A high density of silica microspheres was used to ensure many "hits" between microspheres and template. The transducer was turned on immediately after the addition of the microspheres, and the system was left undisturbed during the assembly time, which is always 3 minutes for the experiments described here. During the assembly time,

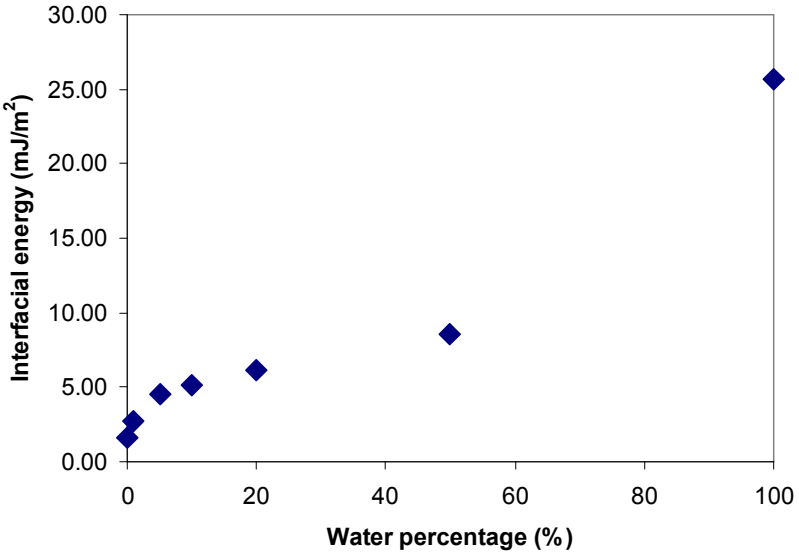

Figure 3. 3 Measured interfacial energy versus water fraction of assembly liquid

the small beaker was capped to keep the acetone from vaporizing and to keep the fluid level constant during the assembly process. After the assembly time, the template was quickly removed from the fluid (~0.1 sec). The number of microspheres assembled in each size hole was then computed using images from an optical microscope. Also, an optical micrograph was captured of each array and saved for later review.

After each experiment, the template was placed in a beaker filled with ethanol and sonicated in a sonic bath for about 1 minute. The excitation frequency of the sonic bath is set to a few kHz, where cavitation bubbles are generated and effectively and completely remove all the present assembled microspheres on the surface of the template. Cavitation is more likely to occur at lower frequency (a few kHz) as compared to the assembly operating frequency of 1.7 MHz, where cavitation is strongly suppressed. The refreshed template was then reused for the next experiment. This recycling of the template is intended to improve the repeatability of the experiment and the ability to vary assembly conditions in a more controlled way.

3.3 Interfacial energy calculation

The interfacial energy was calculated based on contact angle measurement and is plotted against water fraction of the assembly liquid in Figure 3. 3. For contact angle

measurement, one pattered template coated with octadecyltrichlorosilane was prepared. A single drop of an acetone-water mixture with the water fraction varying from 0 to 100% was placed on the prepared surface using a syringe. The contact angle of each drop with the surface of the template was measured by a tensiometer (Kruss, DSA100). Two drops of each mixture were sequentially measured on the surface of the template; after the measurement of contact angle for each drop, the residue of the drop on the surface was completely cleaned or dried out for the next measurement. Two contact angle measurements for each mixture were averaged. Then, the interfacial energy of the solid-liquid interface was computed by invoking the Young-Laplace equation, which is given by

$$\gamma_{SL} = \gamma_s - \gamma_L \cos\theta \tag{3.1}$$

where γ_S is the surface energy of solid, γ_L is the surface energy of liquid and θ is the (measured and averaged in the present case) contact angle of the liquid with respect to the surface of the solid (Figure 3. 4). The interfacial energy γ_S of a hydrophobic surface terminated with (CH_3-) is 21.8 mJ/m^2. The interfacial energy γ_L of each sampled water-acetone mixture was interpolated based on its water fraction between the interfacial energies of pure water (72 mJ/m^2) and pure acetone (23.1mJ/m^2).[16] Because of the high volatility of acetone in air, the contact angle with the acetone mixture must be measured

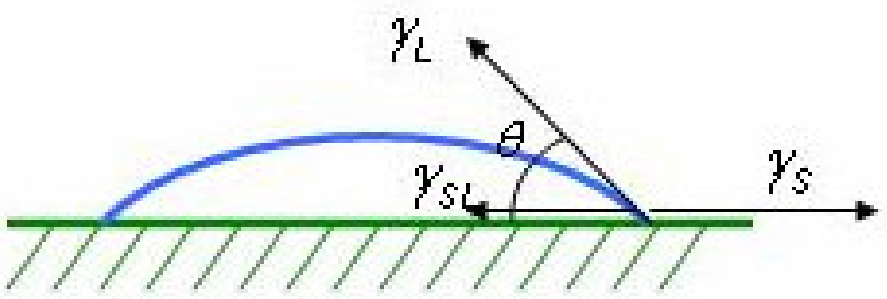

Figure 3. 4 Contact angle of a drop with surfaces forces presented. Surface forces are statically in equilibrium.

immediately after the mixture drop lands on the surface and before the original ratio of the mixture is rendered invalid by the evaporation of acetone. Also, the instant measurement helps catch the stationary contact angle rather than the receding angle, which develops after the evaporation starts, and which is less than stationary angle. The interfacial energy of the Young-Laplace equation is computed based on a stationary contact angle.

4 Proof of concept experiment

In order to demonstrate the concept of TASR, an assembly experiment was conducted with microspheres of the diameter of 1.58 +/- 0.06μm. In this chapter, the layout of the patterns of binding sites (holes) on the surface of the template for the experiment is described. The assembly results are presented and are analyzed to assess how the assembly selectivity varies with contact area between the holes and the microspheres. Calculation of adhesion based on contact area is briefly introduced.

4.1 Layout pattern of holes

The main purpose of this proof of concept experiment was to investigate how well microspheres of one single size assemble into a large number of holes, which vary slightly in size from one to another. As was described previously, the template fabrication technique produces nearly-hemispherical holes that diverge from a hemisphere in two ways. First, each hole has a slightly flattened area at the bottom, which arises from the finite size of the initial exposed spot in the resist. Second, each hole may also have slightly rounded edge profiles due to imperfect adhesion of the PMMA to the surface during the etch process. The first effect, the small flat-bottomed part of the hole shape can be controlled in order to create better-matched holes (smaller flat bottomed regions) or worse-matched holes (larger

flat-bottomed regions). For this first experiment, a range of hole shapes from well-matched to poorly matched were created by varying the size of the exposed spot in the PMMA layer (with the thickness of 220nm) and hence the size of the flat-bottomed area. To create this pattern of many slightly-varying holes, an exposure pattern and an e-beam protocol were created. The e-beam protocol allows the size of the exposed spot in the PMMA (and hence the hole shape) to vary in two ways, by the nominal size of the exposed spot and by the exposure dose. After the oxide etching, both a higher exposure dose and a larger exposed region will create a larger flat area at the bottom of the hole and a larger opening width at the top of the hole. A pattern layout was designed to create a range of hole sizes and shapes by the proposed protocol (varying nominal exposed spot size and exposed dose), and the arrangement is illustrated in Figure 4. 1. The pattern includes twenty arrays. Each array contains the same four nominal exposed spot sizes, but each array is exposed with a different dose to create larger or smaller flat areas at the bottoms of the holes. These will be referred to array number, where one has the lowest exposure dose and twenty has the highest exposure dose. The four different nominal exposed spot sizes within each array are 15, 50, 100, and 150nm (spot size A, B, C, and D, respectively). Because different hole shapes offer a better or worse match to the microsphere shape, the twenty different arrays allow careful examination of how shape matching affects assembly.

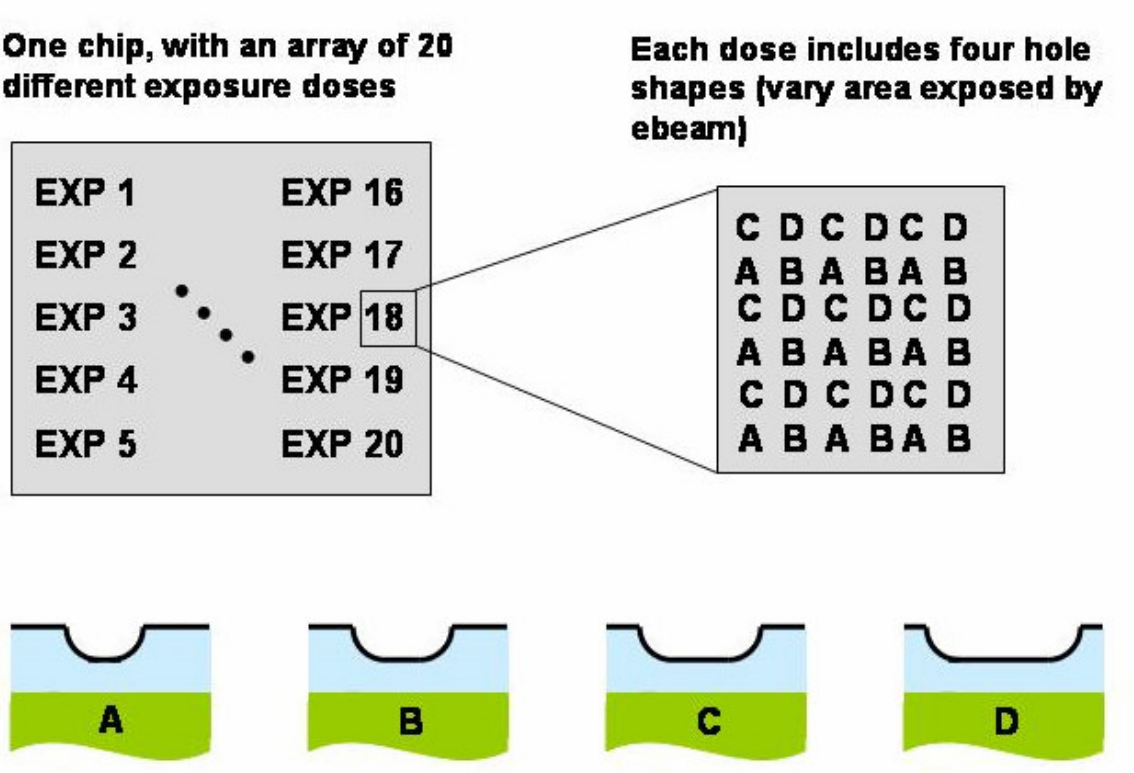

Figure 4. 1 Pattern layout includes 20 arrays, identical, but with increasing exposure dose to form increasingly large holes; close-up of an array showing repeated pattern of four hole shapes (A, B, C, D) corresponding to four different-sized exposure regions. Schematics of four hole shapes (A, B, C, D) after etching are displayed at the bottom.

The four different nominal sizes within each array control for spatial non-uniformities in the assembly set-up. The present pattern layout was designed to provide good opportunity to have different sized holes next to each other, but a great number of holes sizes overall.

4.2 Experimental results

The microspheres used in this experiment are 1.58μm+/- 0.06μm diameter silica (Duke scientific) and are coated as described in 3.1. The template layout is described in

4.1, and it was fabricated as described in 3.1. The holes were etched to a depth of 800nm, which closely matches the radius of the microspheres. The assembly fluid was a mixture of 95 % acetone and 5% water. For this composition, the interfacial energy between template and fluid was estimated at 5 mJ/m^2 (see 2.2). The variable voltage source driving the megasonic excitation was set to 45 volts. The details of the experimental protocol and assembly system are presented in 3.2.

Figure 4. 2 shows an optical micrograph of one of the twenty arrays (the highest exposure dose) after assembly, along with the corresponding template layout. Some of the etched holes are empty, and some of the etched holes contain a sphere; atomic force microscopy was used to confirm the identity of spheres and empty holes. This partial assembly is as expected because the array includes four nominally different exposure spot sizes and hence four different hole shapes. Grid lines are drawn as a guide to the eye to indicate groups of four different hole shapes. Most of the two smallest-sized holes (A and B, etched from nominally 15 nm and 50 nm exposed spots) contain a sphere, while most of the two larger-sized holes (C and D, etched from nominally 100 nm and 150 nm exposed spots) are empty. This reflects the varying quality of sphere-hole match in the different-shaped holes, whose cross-sectional profiles are schematically demonstrated in Figure 4. 1. The fact that assembly occurs in the holes from both the 15 nm and the 50 nm exposed

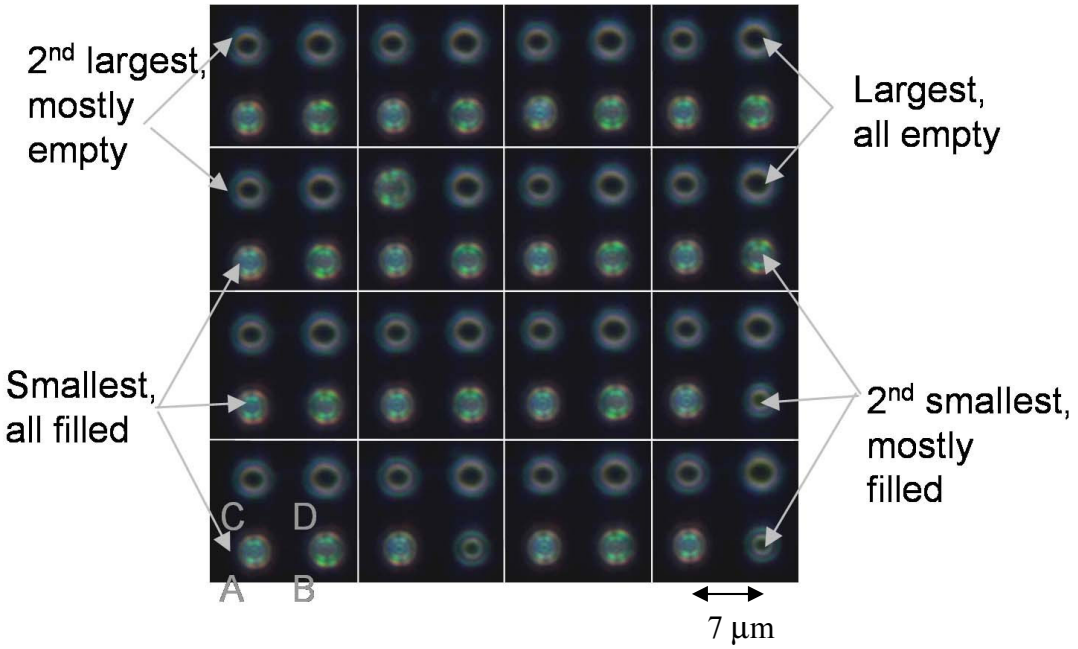

(a)

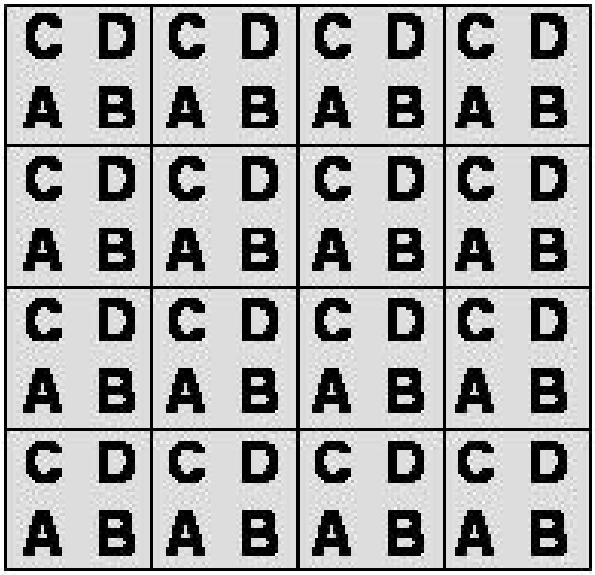

(b)

Figure 4. 2 Assembly results. (a) Optical micrograph of assembly results for the array with largest exposure dose. Filled holes appear solid, and empty holes appear hollow. Grid lines are guides to the eye and identify groups of type A, B, C, and D holes. (b) The corresponding layout of the template presented in (a). The holes shapes of A, B, C, and D are schematically demonstrated in Figure 4. 1.

spots reflects the limited resolution of the e-beam pattern at high exposure dose.

Figure 4. 3 shows the yield (fraction of holes of a given type that contain a sphere) versus array number (where each array number corresponds to a particular exposure dose). Array number 20 was defined with the largest does and so has the largest holes, while array number 1 was defined with the lowest dose and so has the smallest holes. Data are included for each of the four types of holes A, B, C, and D. The quality of the shape match between spheres and holes depends on both the array number and the hole type; this is reflected in the measured yields. Figure 4. 4 shows micrographs of assembly results at four exposure doses whose corresponding array numbers are 2, 8, 16, and 19. The layout

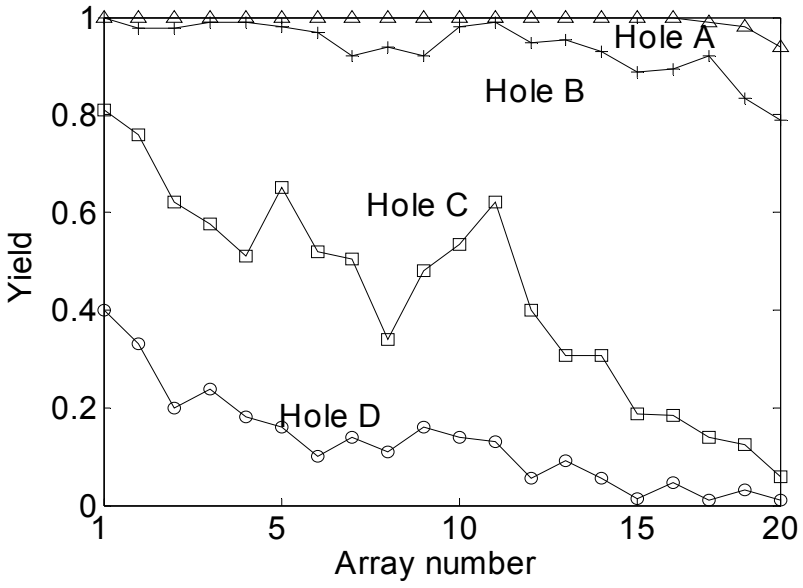

Figure 4. 3 Yield versus exposure number for type A, B, C, and D holes. Higher array number indicates higher exposure.

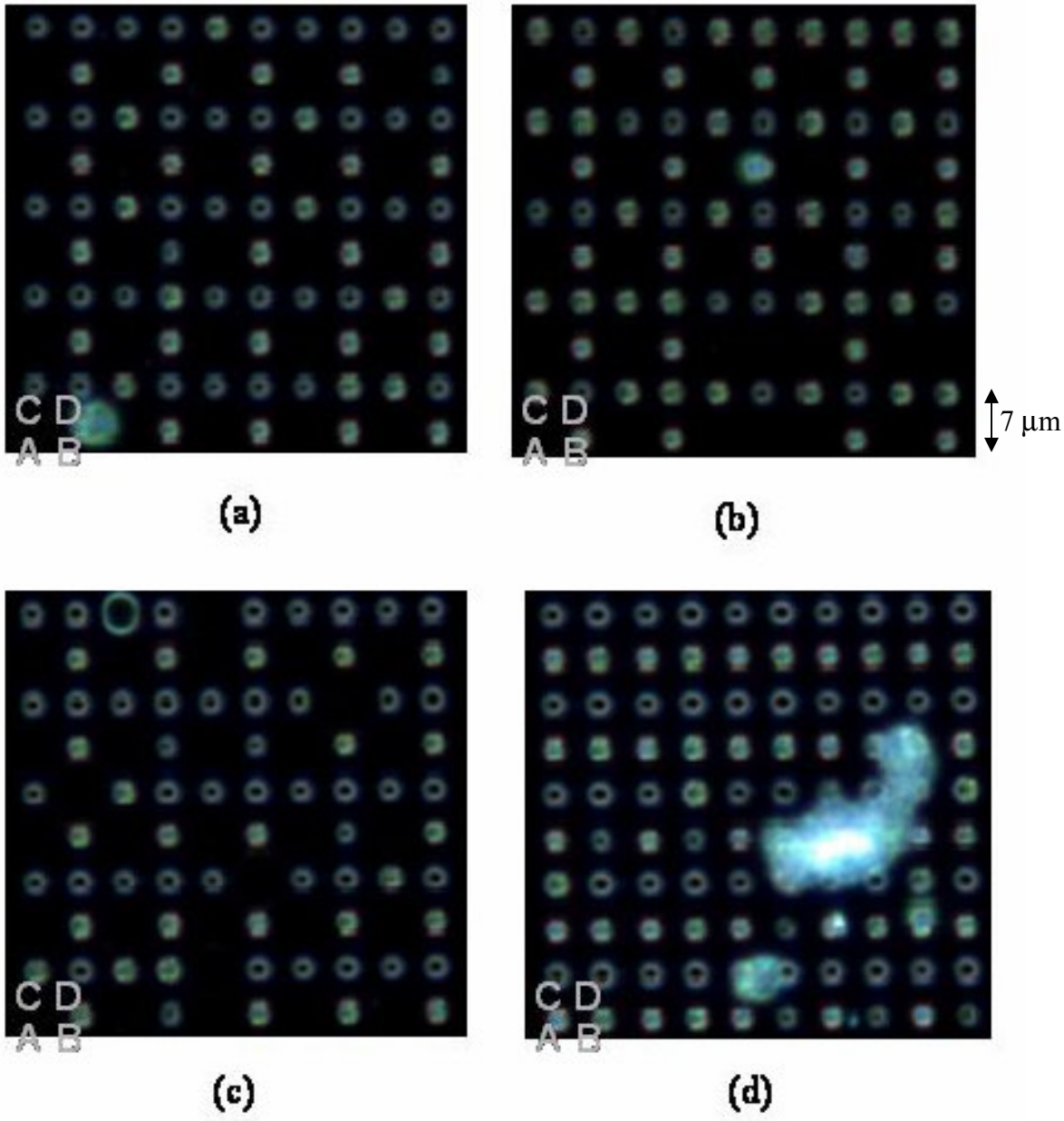

Figure 4. 4 Micrograph of assembly result at the array of (a) 2, (b) 8, (c) 16, and (d) 19.

pattern of each template follows the same manner as described with Figure 4. 2. The repeating pattern of four types of holes as shown in Figure 4. 2 is additionally demonstrated in Figure 4. 4 for the pattern identification. As shown in Figure 4. 4, no holes of type A

were created at the lower doses. These missing holes at the lower doses indicate that the lower exposure doses did not suffice to expose the smallest exposed spots (associated with type A). Since the holes were not fully exposed, the oxide layer was protected from etch by a remaining layer of PMMA, and no hole formed. Holes of type C and D were also found to be invisible in Figure 4. 4 (c), but the reason is different. Surface profiles (provided by atomic force microscopy (AFM)) of the locations where holes of type C and D are expected but appear to be missing shows holes greatly expanded in width. This possibly results from local PMMA layer de-lamination during the etching. This is an artifact of the fabrication process and is of no significance. In Figure 4. 4, holes of type B, C and D at the lower doses (smaller sizes) were found fully or partially filled whereas, at array 20 (larger sizes), holes of type C and D are mostly empty. The yields for C and D decrease with higher dose, whereas those with A and B remain nearly at 100%. A cluster of microspheres was captured with a "cloud" image in Figure 4. 4(d). Figure 4. 4 (c) also illuminates a defect and a cluster of microspheres on the surface that possibly results from adhesive interaction between microspheres.

The quality of the sphere-hole match can be quantified by calculating the contact area between the sphere and the hole. Figure 4. 5 plots the yield vs. fractional contact area, defined as the ratio of the nominal contact area to one half the total surface area of the

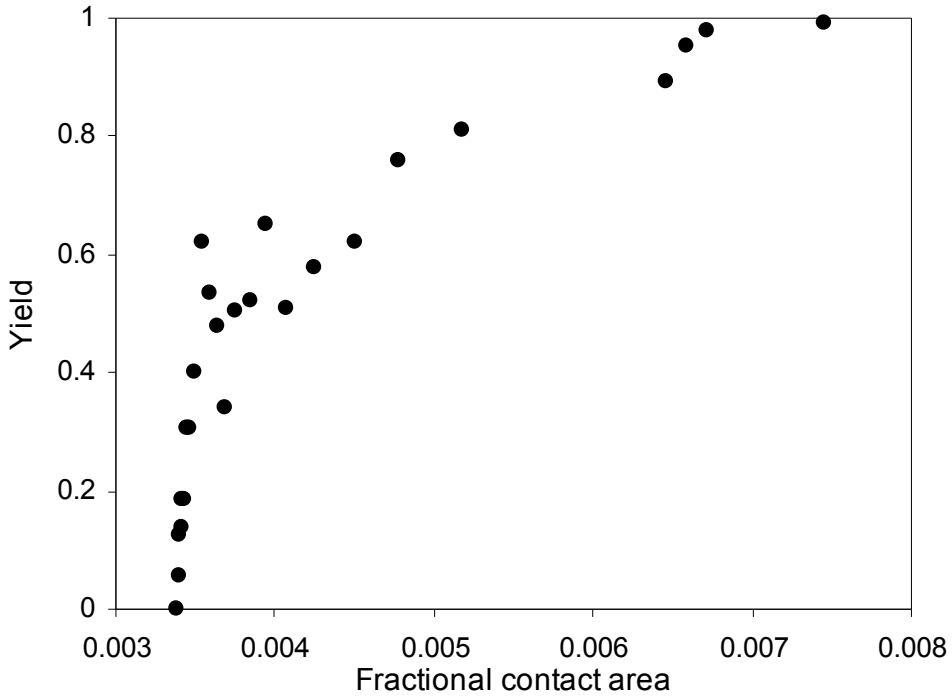

Figure 4. 5 Measured yield versus fractional contact area

sphere. The "nominal" contact area was calculated as follows: if any two points on the sphere surface and the template surface are separated by a distance of 1.5 nm or less (the assumed characteristic distance of the hydrophobic force), they are considered to be in contact. The estimation method is also schematically presented in Figure 4. 6. The nominal contact area omits the effects of surface roughness, which will be considered later. All other points on the sphere are considered to be out of contact with the template surface. Because the hole geometry is not an ideal hemisphere, the actual geometry was measured using atomic force microscopy (AFM). Figure 4. 7 shows typical hole profiles resulting from two different exposure conditions. A numerical technique was used to compute the

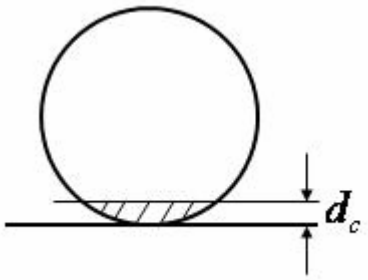

Figure 4. 6 Nominal contact area presented with shadow area.

contact area; the details of the numerical method are presented in Appendix A and B. Several nominally identical holes were profiled for each array number. The results were averaged and fit to a third order polynomial shape function; this function was used as the input for the numerical contact area computation. The coefficients of determination, *r*, of the curves with the sidewall profile data were estimated in the range of 0.95 and 0.98, implying that the method of the third order polynomial curve fit adequately describes the sidewall profile.; the coefficient of determination provides a summary of statistics that measures how well the regression equation fits the data, and the coefficient is equal to one when a curve fit and data are perfectly matched.[20] Because of the isotropic etching of oxide, the holes are created axially symmetric. The nominal contact area depends on the sphere's position within the hole. The maximum contact area occurs when the sphere is on the curved sidewall, between 125 nm and 180 nm from the edge of the flat bottom, depending on the array number. This distance is related to the eccentricity, the horizontal

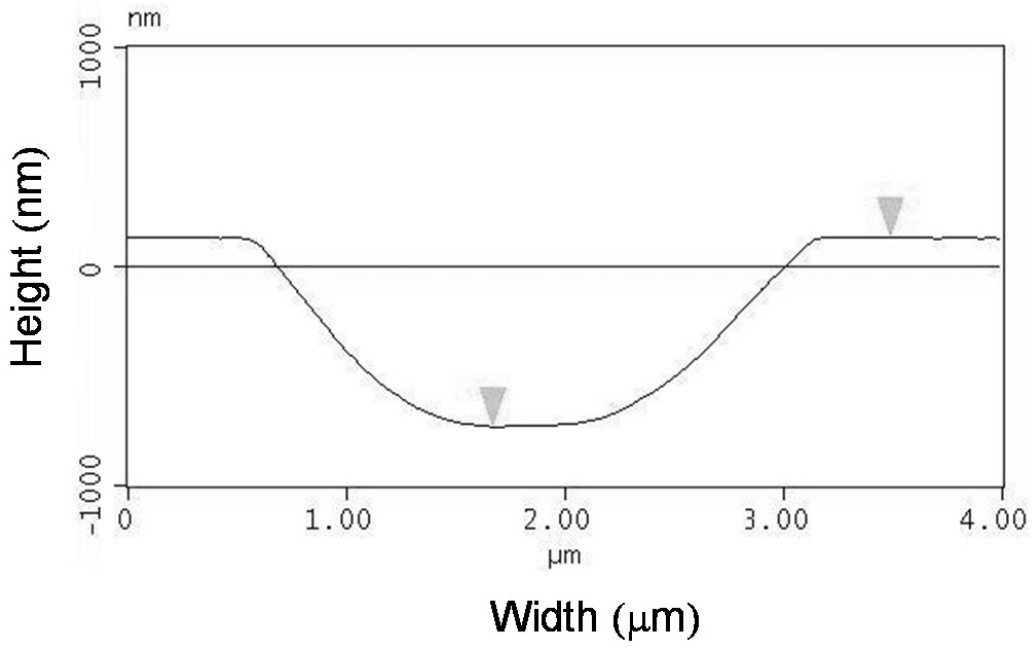

(a)

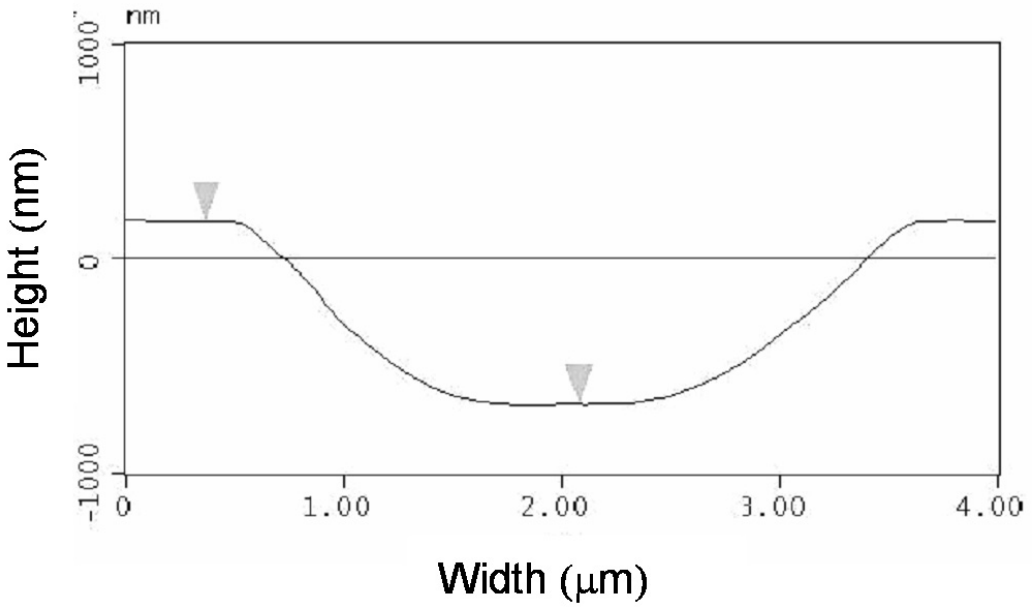

(b)

Figure 4. 7 Profile of (a) a sample type A hole and (b) a sample type D hole, measured by AFM.

distance between the center of mass of the sphere and the point at which it contacts the curved sidewall. In Chapter 5, it will be seen that a torque, which selectively rolls spheres out of poorly-matched holes, can be estimated by the cross product of a vertical force and the eccentricity.

The "nominal" contact area is not the true contact area because it omits the effects of surface roughness. To calculate true contact area, the asperities of both sphere and sidewall surfaces must be considered. The surfaces were scanned in detail with an AFM, and the data were flattened in a surface analysis software package (SPIP, Image Metrology) to obtain rms and peak roughness. The AFM surface scanned data on roughness are well described by normal distributions. For simplicity, these two nominally flat surfaces with random roughness are replaced with one perfectly smooth surface and a single surface with an equivalent roughness that reflects the roughness of the two surfaces (Figure 4. 9 (a) and (b)), which is also given by

$$\sigma_{eq} = \sqrt{\sigma_s^2 + \sigma_h^2} \tag{4.1}$$

where σ_s and σ_h are the rms roughness for the sphere and hole surfaces, respectively.[21] The engagement of the two surfaces is more realistically set by allowing the interpenetration of two maximum peaks from both sphere and sidewall surfaces, h_s and h_h by 0.5 nm. Based on the simplified roughness model, "true" contact area is

statistically estimated using bearing ratio[22], which is the ratio of all the area existing above a given depth from a reference line to the whole scanned area. In the simplified model, the bearing ratio is set to the ratio of "true" contact area (as shown with blue lines in Figure 4. 9 (c)) to the whole scanned area. The depth associated with the "true" contact area is set to the characteristic length of the hydrophobic force, d_c. The reference line is set with the peak of the equivalent surface at full contact and it is shifted up when a separation is imposed. Assuming that the roughness of equivalent roughness surface is normally distributed, the bearing ratio C_r is estimated by

$$C_r = 1 - \int_{-\infty}^{\frac{0.5(h_s+h_h)-0.5-d_c+z}{\sigma_{eq}}} \frac{1}{\sqrt{2\pi}} e^{-w^2/2} dw \qquad (4.2)$$

where z is the nominal separation (omitting roughness) of two points on the microsphere surface and the hole surface as schematically presented in Figure 4. 8. By using d_c in this equation, we are approximating the exponential reduction in the hydrophobic force over distance by a step function, so that any two points are either in contact or out of contact. In (4.2), z varies from 0 to 1.5 nm because contacted surfaces of the present case (involving microspheres and near-hemispherical holes) are curved and additionally any two points on the two contacted surfaces with the separation less than d_c (=1.5 nm) are considered to be in contact by the definition. However, full incorporation of the z

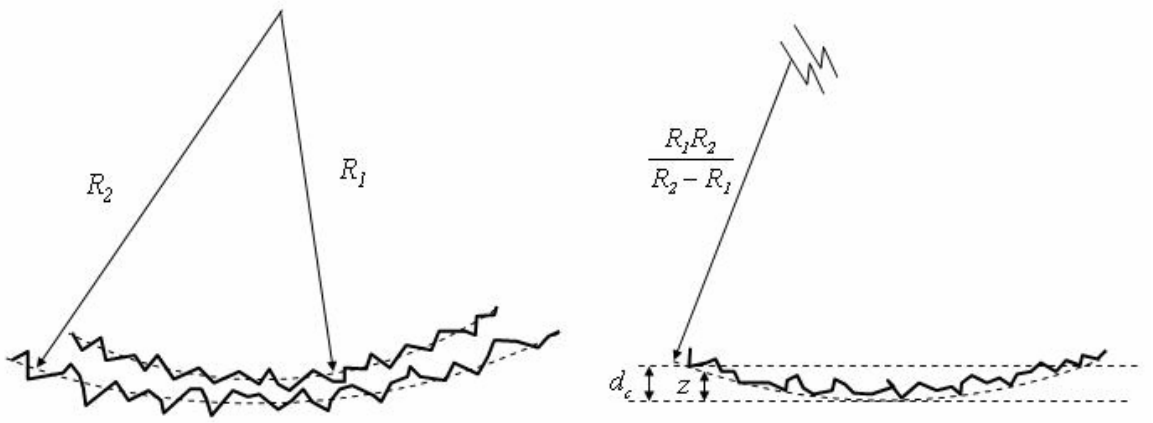

Figure 4. 8 Schematic presentation of the nominal separation, *z*. Diagram (left) of two curved surfaces in contact and the equivalent diagram (right) with one flat surface and one surface with equivalent roughness and equivalent curvature.

variation into (4.2) for each case of microsphere-hole contact requires a significant amount of computational effort. Here, instead of invoking full numerical computation for each case of contact, C_r was estimated based on an ideal case, where a microsphere of 1.6 μm is in contact with a flat surface; from now on, the value of C_r estimated based on the ideal case was directly applied to all subsequent analyses. With $h_s = 3.83nm$, $h_h = 2.37nm$, $\sigma_s = 0.681nm$, $\sigma_h = 0.508nm$, $d_c = 1.5nm$, and the variation of *z* of the ideal case, eq. (4.2) yields C_r=0.02, i.e. the true contact area is only 0.8% of the nominal contact area. Then, the "true" contact area, A_t is given as a function of the nominal contact area A_n and the bearing ratio C_r as

.

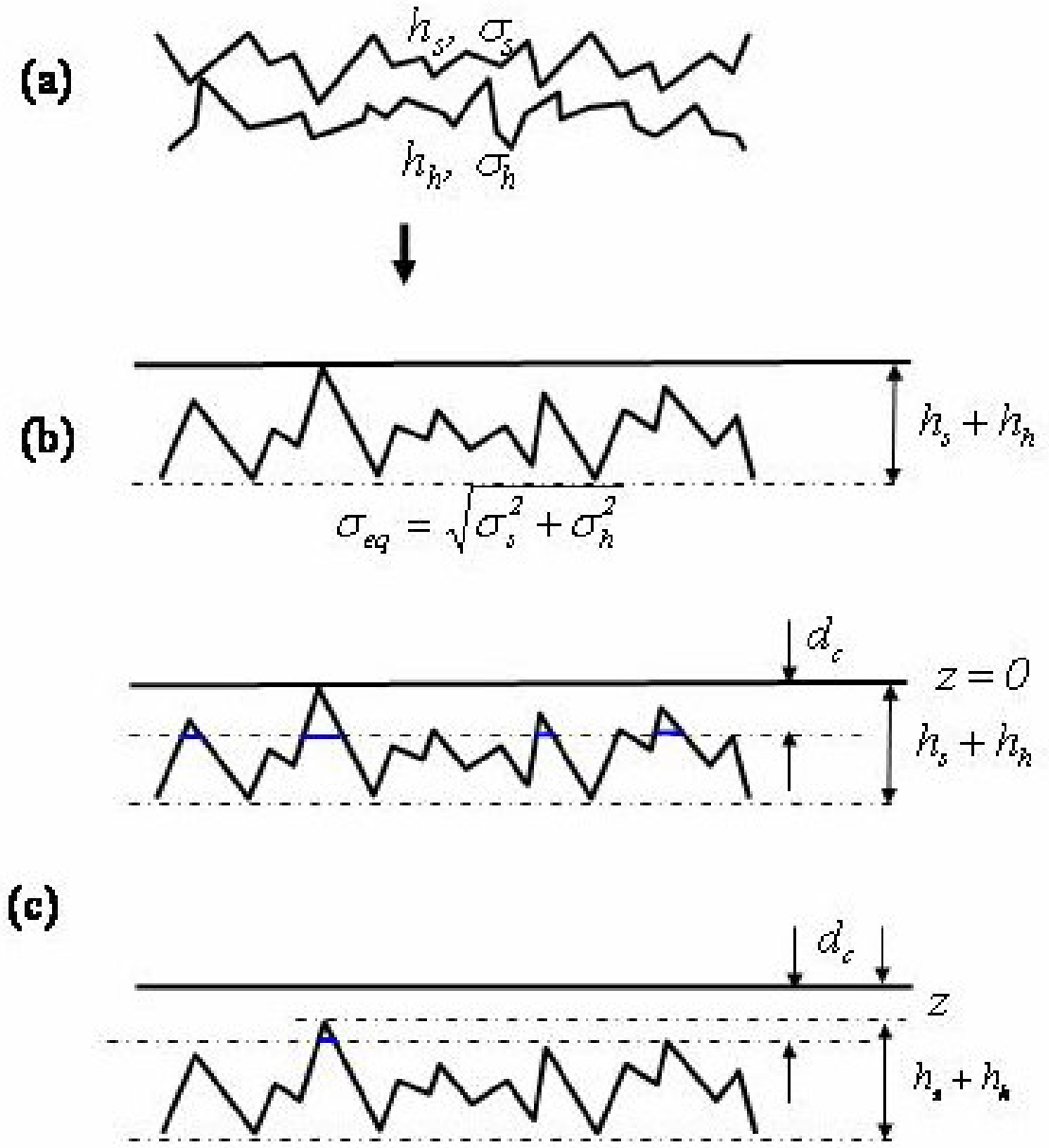

Figure 4. 9 "True" contact area estimation. (a) Two contacted surfaces with random distribution of roughness (b) Simplified roughness model. Equivalent surface (bottom) reflecting roughness of the two surfaces and perfectly smooth surface (top).[21] (c) Bearing ratio and "true" contact area (indicated with blue lines) at full contact (top) and with separation (bottom).[22]

$$A_t = C_r A_n . \tag{4.3}$$

From this point on, the words “contact area” will refer to the true contact area, including the effects of roughness. Further, the change in the contact area when the microspheres encounter the holes changes the free energy, thereby inducing adhesive force between the microspheres and the template. These adhesive forces and their quantitative assessments are extensively described in the context of the theoretical model of selective removal mechanism in Chapter 5.

5 Selective removal mechanism

In this section, the basic theory describing selective removal is first presented. Then, the forces arising from the hydrophobic interaction and the forces from the megasonic excitation are respectively described and their relevance for the selective removal processes is quantitatively assessed. Finally, based on the quantitative assessment of the interactions between the holes and the microspheres, the most feasible model of the present assembly is proposed, and its scalability is discussed.

5.1 Analysis and modeling of the selective removal mechanism

The ultrasonic field produces forces perpendicular to and parallel to the substrate surface. These forces can drive different removal mechanisms in which spheres either move along the surface or lift off the surface. For each removal mechanism there is a corresponding retention mechanism that opposes the motion. Two criteria must be met in order for a removal/retention mechanism to adequately describe the observed selective removal.

1) The magnitude of the removal force/torque must be comparable to the magnitude of the corresponding retention force/torque.

2) The removal process must be irreversible and complete; in other words, the mean value of the ultrasonic force/torque must be non-zero.

The first criterion is important because the magnitudes must be roughly comparable to ensure that conditions can be adjusted so that removal effects exceed retention effects to ensure removal, or so that retention effects exceed removal effects to ensure retention. However, this selective removal may be only momentary if the removal force/torque is oscillatory. With an oscillatory force/torque, the removal occurs momentarily, only for the half cycle when the direction of the force/torque is in favor of the removal. For the other half cycle the microsphere is pushed back into the hole. Consequently, to achieve complete (not temporary) removal, the removal force/torque must satisfy the second criterion. The first criterion is also often adopted in previous assembly studies to confirm feasibility of a proposed mechanism for assembly on an order of magnitude comparison basis, where detailed estimations are not possible.

Two motions that can contribute to the removal of the microspheres are lift-off (removal perpendicular to the surface) and roll-off (removal along the surface). Lift-off is driven by forces perpendicular to the surface and can be reversible or irreversible. If lift-off is driven by an oscillatory force with zero mean value, the sphere will be alternately

removed from and returned to the surface, with no net removal. If lift-off is instead driven by a nonlinear force with a non-zero mean value, the sphere may be irreversibly removed from the surface. Roll-off, too, may be driven by nonlinear forces. However, it may also be driven by oscillatory vertical forces because torque associated with an oscillatory force is not necessarily averaged out. Figure 5. 1 illustrates one case in which a net torque is provided by an oscillatory vertical force. As shown in Figure 5. 1, a vertical force acting on a microsphere in a hole with non zero eccentricity creates a torque that tends to roll the microsphere out of the hole. However, once a microsphere has rolled out completely out of the hole and onto the flat surface, it has zero eccentricity and experiences no more torque. The two half cycles, when combined, possibly result in a net torque. However, one constraint must be additionally imposed in order for the present case to fully satisfy the irreversibility criterion. That constraint is that the roll-off must be completed in one half cycles before the vertical force starts to be oriented downward. Otherwise, it would be fully reversible.

For lift-off, consider a sphere that is fully in contact with the surface, so that the nominal vertical separation z between the microsphere and the surface is zero. The retention force that opposes liftoff is calculated based on the rate of change of the contact area with separation,

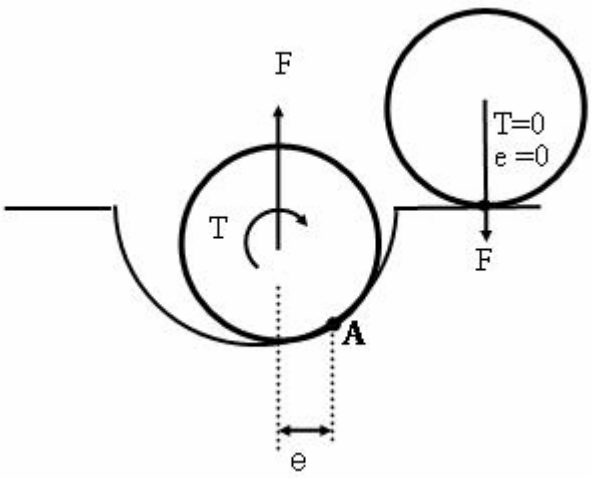

Figure 5. 1 Irreversible roll-off mechanism. When a microsphere is inside a hole, the upward vertical force acting at the center of the sphere with an eccentricity of e creates a torque around the effective contact point, A, that tends to roll the sphere up the sidewall. When the microsphere is outside the hole and on the flat surface, the downward vertical force creates no torque, which results in a net torque overall.

$$\frac{dA_t}{dz} = C_r \frac{dA_n}{dz} + A_n \frac{dC_r}{dz}. \tag{5.1}$$

The second term, $\frac{dC_r}{dz}$, of eq. (5.1) is schematically presented in Figure 4. 8. Using the calculated nominal contact area and assuming a normally distributed roughness, equation (5.1) becomes

$$\frac{dA_t}{dz} \approx C_r \frac{A_n}{d_c} + A_n \frac{1}{\sqrt{2\pi}\sigma_{eq}} exp\left(-\frac{1}{2}\left(\frac{0.5(h_s + h_h) - 0.5 - d_c + z}{\sigma_{eq}} \right)^2 \right). \tag{5.2}$$

Here, the free energy engaged in the assembly and removal is proportional to the contact area. Therefore, the rate of change of the contact area results in the retention force. However, it should be noted that the contact area-based free energy estimation is only

allowed when the force characteristic length is much smaller than the component size. When the size of the component and the force characteristic length are comparable, the spatial variation of the force strength of the engaged field needs to be accommodated, requiring additional computational efforts. Using this estimation, the magnitude of the vertical retention force is then

$$F_r = \gamma dA_t / dz \,. \tag{5.3}$$

The value of $\frac{dA_t}{dz}$ given by (5.2) becomes the maximum at z=0, consequently implying that retention force against lift off peaks at the initial contact, z=0. Further, in order for any removal force to induce lift-off, the magnitude of the removal force must be greater than that of the maximum retention force (although this condition is not sufficient for lift-off to take place). Evaluating the retention force for holes and assuming all of the values given above, the maximum vertical retention forces of the holes in the proof-of-concept experiment as described in Chapter 4 are in the range of 4.4×10^{-7} N to 0.9×10^{-8} N.

For roll-off, consider a sphere that is fully in contact ($z = 0$ at the point of closest approach) with the surface as described above. There will be a retention force that opposes roll-off because the contact area varies with position along the surface. Because rolling is parallel to the surface, the rate of change of contact area comes primarily from the "nominal" area change and is

$$\frac{dA_t}{d\theta} = C_r \frac{dA_n}{ds}\frac{ds}{d\theta} \tag{5.4}$$

which may be readily evaluated numerically as

$$\frac{dA}{d\theta} \approx C_r \frac{\Delta A_n}{\Delta s} R_s \tag{5.5}$$

where s is the position along the surface, θ is the angle of rotation that corresponds to s, and R_s is the radius of sphere as described in Figure 5. 2. Based on (5.5), theoretically, if the hole is an ideal hemisphere, the local radius of the side wall and contact area would be fixed, allowing no retention torque in response to the rolling motion as the sphere travels up the sidewall. Only when the effective contact point (A in Figure 5. 1) is at the edge would the contact area change greatly with the rolling motion, creating a large retention torque. However, because the present hole shapes as seen in Figure 4. 7 are not ideal hemispheres, the contact area changes gradually from the bottom of the hole to the edge as shown in Figure 4. 7, thereby introducing a retention torque in response to the rolling motion over the sidewall. Figure 5. 3 shows fractional contact area versus the distance of the contact point on the sidewall in x-direction from the point where the sidewall starts. In order for the given contact area data of Figure 5. 3 to be used for calculation of the contact area rate of change with respect to the angle θ, eq. (5.5) needs to be extended as

$$\frac{dA}{d\theta} \approx C_r \frac{\Delta A_n}{\Delta x}\frac{\Delta x}{\Delta s} R_s \ . \tag{5.6}$$

In the present case, the value of $\frac{\Delta A_n}{\Delta x}$ was estimated by reading the slopes from

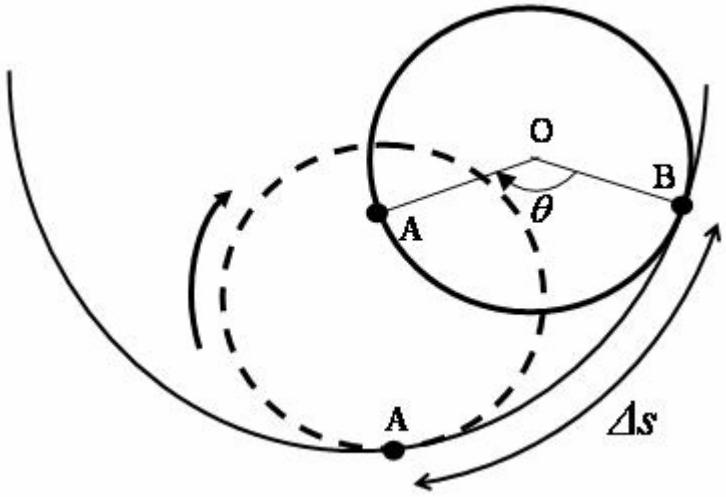

Figure 5. 2 Schematic of a sphere rolling inside a hole and the rolling angle, θ. The dotted line sphere represents a microsphere at a previous time and the solid line sphere represents the microsphere at the current time. The rolling angle is formed by two different lines, connecting the center of rotation, O, to a current effective contact point, B and to the previous contact point, A, respectively.

Figure 5. 3. After the rate of change of contact area is computed, the adhesive torque opposing roll-off is readily calculated as

$$T_r = \gamma \frac{dA}{d\theta}. \tag{5.7}$$

The torque calculated from eq. (5.7) is conjugate to the rolling motion with respect to the effective contact point. Evaluating the retention torque for holes of 20 different sizes with d_c=1.5 nm and γ=5 mJ/m^2 yields maximum retention torques for the proof-of-concept experiment described in Chapter 4 in the range of $1.5\text{x}10^{-17}$ ~ $4.4\text{x}10^{-17}$ Nm. Kinetic energies of the microspheres associated with their inertia are excluded in the present analysis because they are very small at the micro-scale. Also, elastic energy associated

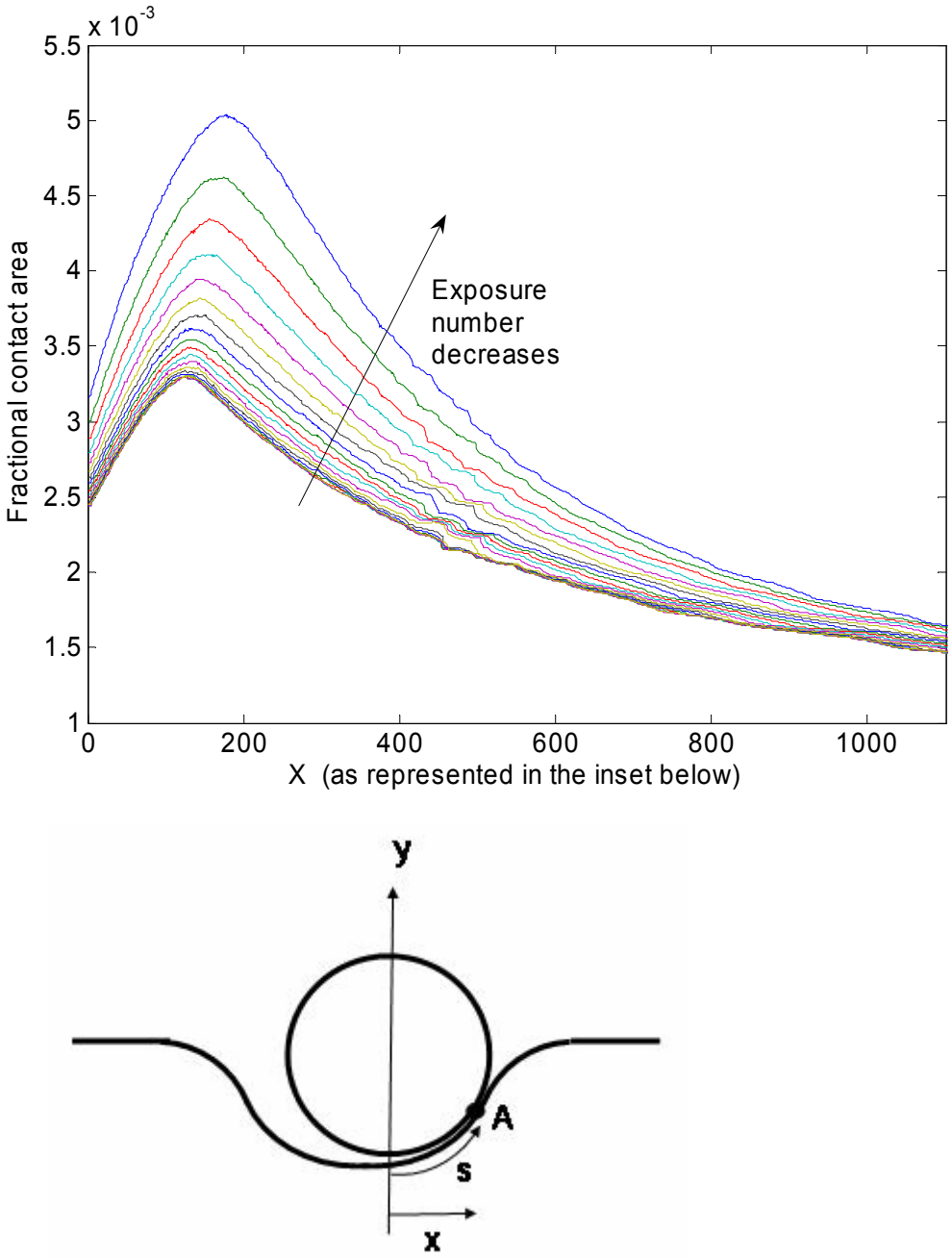

Figure 5. 3 Plot of fractional contact area versus the distance of the contact point A on the sidewall in x-direction from the point where the sidewall starts as illustrated in the inset below.

with deformation is excluded because significant elastic deformation of a high stiffness material such as silica is unlikely. More fundamentally, elastic energy does not count as

free energy change because elastic deformation is thermodynamically reversible; the detail is presented in Chapter 7.

The removal forces stem from the fluidic forces associated with the ultrasonic field. In the experiments described here, the ultrasonic plane wave was set to strike the fluid-solid interface at normal incidence to minimize the boundary layer thickness on the surface. The fluidic forces associated with normal incidence are either vertical forces, which induce lift-off and rolling up the sidewalls of holes, or parallel forces[23-26]. Both were described and summarized by Qi *et al.*[26] for the high frequency case. The relevant forces are summarized below, following the naming conventions of Qi *et al.*[26] However, some of definitions are expressed in an alternate form in order to be more consistent with the present case.

The vertical forces include the added mass, drag, Basset, and radiation forces. The added mass, drag, and Basset forces are all linear and oscillatory; the radiation force is non-oscillatory. The linear forces are *linearly* proportional to the oscillatory velocity in the wave field, thereby resulting in zero mean after one full cycle. Also, because they are dependent on the velocity of the first order term (i.e. the oscillatory velocity), they are greater in magnitude than the nonlinear forces, which are associated with the second order term. Based on the ratio of inertia to viscous effects, the linear forces are divided into

added mass, Basset forces, and drag. It should be noted that Reynolds number does not apply to assess the ratio of inertia to viscous effects in the oscillatory (unsteady) flow field, unlike steady flow fields.[24] In the oscillatory field at the microscale, the inertia effects are more represented by the temporal term $\rho\frac{du}{dt}$ than the spatial term $\rho u\frac{du}{dx}$ (also known as the convective term). Therefore, for the comparison of inertial effects with viscous effects for the oscillatory field, the relevant non-dimensional ratio is the ratio of the viscous term $\mu\frac{d^2u}{dy^2}$ to the temporal term $\rho\frac{du}{dt}$, which is given by,

$$\frac{\mu\frac{d^2u}{dy^2}}{\rho\frac{du}{dt}} \approx \frac{\mu\frac{u}{R^2}}{\rho\frac{u}{t}} = \frac{\frac{\mu}{\rho}t}{R^2} = \frac{\upsilon t}{R^2} = \left(\frac{\delta}{R}\right)^2 \tag{5.8}$$

Eq. (5.8) implies that the ratio $\frac{\delta}{R}$ of the boundary layer thickness $\delta \sim \sqrt{\upsilon t}$ to the characteristic length *R* properly represents the relative significances of inertia and viscosity in the oscillatory flow field. In the inertia dominated regime (thin boundary layer), $\frac{\delta}{R} << 1$, the added mass force is dominant, whereas the drag is dominant in the viscous dominated regime, $\frac{\delta}{R} >> 1$. The Basset force plays a role when the viscous and inertial effects are competitive.[24]

The added mass force on the sphere stems from the acceleration of nearby fluid, and its magnitude is given by

$$F_{mass} \sim \frac{2}{3}\pi\rho R_s^3\left|\frac{du}{dt}\right| = \left(\frac{2}{3}\pi\rho R_s^3\right)\left(2\pi f|u|\right) \tag{5.9}$$

where R_s is the radius of the sphere, $u = \sqrt{I/\rho c}e^{i2\pi ft}$ is the oscillatory velocity, ρ is the density of the liquid, I is the intensity of the incident acoustic wave, c is the wave speed, and f is the wave frequency. The added mass force comes from the temporal (unsteady) inertia term, $\rho\frac{du}{dt}$, but not from the spatial inertia term, $\rho u\frac{du}{dx}$. For $\frac{\delta}{R} >> 1$, the drag force is dominated by viscosity, and its magnitude is given by

$$F_{drag} \sim 6\pi\mu R_s|u_{rel}| \tag{5.10}$$

where u_{rel} is the velocity of the microsphere relative to the host liquid. The relative velocity u_{rel} results from the differences of magnitude and phase between the oscillatory flow and the oscillatory motion of the microsphere. However, it would be inappropriate to exactly estimate u_{rel} because of the inherent complexity of the flow field. Rather in the present work, u_{rel} is replaced with u, which means that the microsphere is set to be stationary for the drag force computation. The phase of the drag force is $\frac{\pi}{2}$ behind the added mass force. The Basset force comes from the combination of the unsteady shear stress and the added mass force. This is significant when $\delta / R_s \sim 1$. The boundary layer (where viscosity is dominant) is on the surface of the microsphere and the inviscid flow (where inertia is dominant) is present beyond the viscous layer, but the inviscid flow is still largely affected by the presence of the microsphere because $\delta / R_s \sim 1$. The flows inside and outside the boundary layer collaboratively create the Basset force with a phase delay of

$\frac{\pi}{4}$ from the added mass force. The magnitude of the Basset force is approximately

$$F_{Basset} \sim \left(6\pi\rho R_s^3 \left|\frac{du}{dt}\right|\right)\left(\frac{\delta}{R_s}\right) = \left(12\pi^2 \rho R_s^3 f \sqrt{\frac{I}{\rho c}}\right)\left(\frac{\delta}{R_s}\right) \tag{5.11}$$

However, these linear forces act on a microsphere with different temporal phases, so that for some parts of the cycle time they may partially cancel and for some other parts they add up. Therefore, in order to be physically consistent (i.e. include phase difference), all the linear forces should be represented by their resultant force. The resultant force combines all the linear forces with a phase adjustment as shown schematically in Figure 5. 4; the added mass force and Basset force have the phase leads of $\frac{\pi}{2}$ and $\frac{\pi}{4}$, respectively, relative to the drag force. The resultant force is given by

$$T_{removal} = (e) \times \sqrt{F_{mass}^2 + F_{drag}^2 + F_{Basset}^2 + 2F_{Basset}\sqrt{F_{mass}^2 + F_{drag}^2}\cos(\theta)} \tag{5.12}$$

where $\theta = \frac{\pi}{4} - tan^{-1}\left(\left|\frac{F_{mass}}{F_{drag}}\right|\right)$. As another vertical force, the radiation force can also be included. However, this force is nonlinear so that the magnitude is constant, but it is also small compared to the oscillatory linear forces. The magnitude of the axial radiation force on spheres much smaller than the wavelength of the traveling waves is given[19] by

$$F_{radiation} \sim 64\rho\left(\frac{2\pi f}{c}\right)^4 R_s^6 |u|^2 \frac{1 + \frac{2}{9}\left(1 - \left(\frac{\rho}{\rho_p}\right)^2\right)}{\left(2 + \frac{\rho}{\rho_p}\right)^2} \tag{5.13}$$

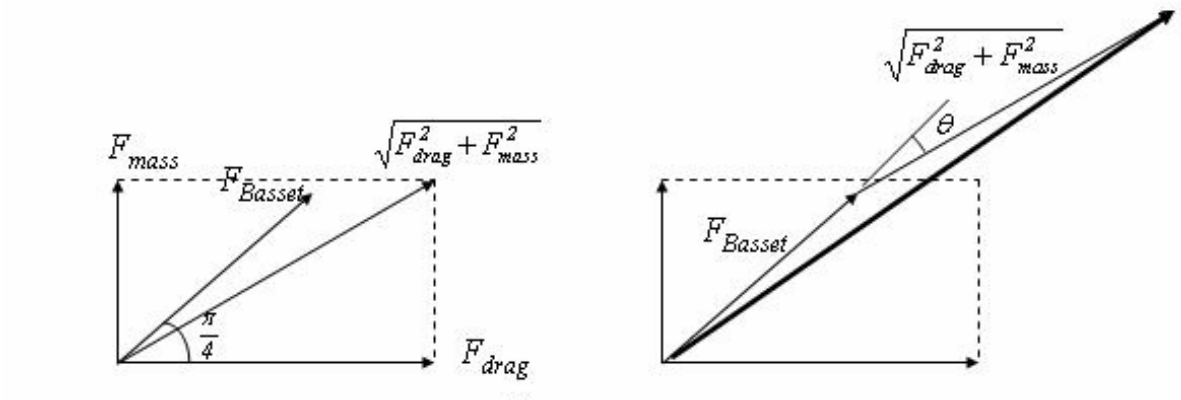

(a) (b)

Figure 5. 4 Schematic of adding linear oscillatory forces with different phases in magnitude-phase plot. (a) Basset force and the resultant force of added mass force and drag force are presented. (b) The resultant force of added mass force, drag force and Basset force presented with a thick solid line and an angle $\theta = \frac{\pi}{4} - tan^{-1}\left(\left|\frac{F_{mass}}{F_{drag}}\right|\right)$.

where ρ_p is the density of the microsphere. As seen in eq (5.13)., the radiation force goes as the sixth power of the radius, and is thereby expected to be extremely small in the present set-up where the wave length of the ultrasound is on the order of 1 mm and the size of the microsphere is on the order of 1μm. However, if the frequency were higher and the wavelength were smaller, which is not the present case, this force would increase. When the wavelength is comparable to the size of microsphere, the size dependence vanishes and eq. (5.13) is no longer valid. Instead, when the wavelength is comparable to the size of the spheres, which it is not in the present case, the radiation force is given by

$$F_{radiation} \sim \frac{\rho}{89}\left(\frac{uc}{2\pi f}\right)^2 \frac{95 - 48\left(\frac{\rho}{\rho_p}\right) + 36\left(\frac{\rho}{\rho_p}\right)^2}{5 + 6\left(\frac{\rho}{\rho_p}\right) + 2\left(\frac{\rho}{\rho_p}\right)^2} \tag{5.14}$$

Radiation force is also present perpendicular to the wave's direction of propagation, but it is much weaker than in the axial direction. It was also found that for particles smaller than 15 μm, acoustic streaming, which is discussed in the following paragraph, is much greater than the lateral radiation force.[27] Therefore, the lateral radiation force is excluded from the present discussion.

A parallel force is created by acoustic streaming flow.[18] Acoustic streaming arises 1) due to energy absorption in the bulk phase or 2) due to energy dissipation at the interfaces between the solid and fluid. The first type of acoustic streaming is found in an unbound media and is also named Eckart streaming.[28] Generally, its length scale associated with energy absorption is much greater than the wavelength of the ultrasound. The flow of Eckart streaming exerts a vertical force on the microspheres, but its magnitude is usually much weaker than the second type of acoustic streaming. The second type of acoustic streaming is found when the flow field is restricted by solid surfaces, and its length scales are either in the same order of magnitude as the wavelength (Rayleigh streaming[29]) or much smaller than the wavelength (Schlichting streaming[30]). Schlichting streaming is

prominent especially in the boundary layer on the surface. Schlichting streaming is also termed boundary layer acoustic streaming, and its flow direction is parallel to the surface. In the present assembly experiments, the sphere size was found to be comparable to the boundary layer thickness on the surface of the template, which therefore allows the boundary layer acoustic streaming at the surface to effectively provide drag on the sphere in the boundary layer at the surface. The drag can be estimated as Stokes flow because the flow by acoustic streaming is in the laminar regime. The magnitude of the resulting torque on a sphere in contact with the substrate is given by

$$T_{acoustic} \sim 6\pi\mu R_s^2 u_{acoustic} = 6\pi\mu R_s^2 \frac{|u|^2}{fa} \tag{5.15}$$

where $u_{acoustic}$ is the mean flow velocity of the acoustic field and a is the characteristic length of the oscillatory tangential velocity surface gradient. Here, the tangential velocity is simply estimated as the oscillatory velocity u by assuming that the oscillatory flow field is incompressible and solenoidal at the solid surface. The details are given later in Section 6.3.4 in the context of the circulation issue. The characteristic length a is taken to be the half wavelength of the ultrasound (~0.8mm) based on the pitch of the concentric annular bands of microspheres observed on the surface, which results from standing wave induced in the bottom plate of the inside beaker by the ultrasound wave (also refer to Section 6.3.4

for the details). Then, torque is estimated instead of force because spheres are more likely to roll than slide at the surface. The selection of the characteristic length is discussed in detail in Section 6.3.4.

The criterion of irreversible removal limits the forces and mechanisms that can contribute to selective removal. Only the radiation force could cause direct lift-off, since it is the only nonlinear vertical force. All of the listed forces may contribute to roll-off: the added mass, viscous drag, Basset, radiation, and acoustic streaming forces. After selecting forces based on the irreversibility criterion, the requirement that the retention and removal forces or torques have comparable magnitude limits the possible force and mechanism further. The force magnitudes were calculated for the proof-of-concept experiment described in Chapter 4 using equations (5.9-12, 15) and summarized in Table 5. 1. For the material constants of the force calculation, typical reported values are used. The constants used are $\mu_{mixture} = 2.57 \times 10^{-4} kg/ms$, $\rho_{mixture} \cong \rho_{acetone} = 789 kg/m^3$, $\rho_p = \rho_{microsphere} = 2330 kg/m^3$, and $\upsilon_{mixture} \cong \upsilon_{acetone} = 0.326 \times 10^{-6} m^2/s$. Based on the constants, the oscillatory velocity was calculated as $u \sim \sqrt{\frac{I}{\rho_{mixture} c}} \approx 0.0043 ms^{-1}$. The oscillatory velocity u of the wave is directly converted from the intensity as expressed above. However, since the intensity can not be directly assessed in the present assembly

Table 5. 1 Fluidic forces and torques

	Force	Torque
Radiation	7.1×10^{-22} N	1.4×10^{-28} Nm
Acoustic streaming	6.7×10^{-15} N	5.4×10^{-21} Nm
Added mass	3.8×10^{-11} N	7.7×10^{-18} Nm
Viscous drag	1.7×10^{-11} N	3.3×10^{-18} Nm
Basset	1.9×10^{-10} N	3.8×10^{-17} Nm
Resultant	2.3×10^{-10} N	4.6×10^{-17} Nm

system, the intensity was computed based on additional measurements and wave interference theory. The initial power from the transducer was estimated first with a calorimeter set-up as explained below. Then, the transmitted power (the portion of the initial power that survives through the bottom plate of the assembly beaker and the template) is calculated based on a wave interference theory. Finally, an adjustment of the transmitted power was made based on a predicted spatial distribution of the wave on the bottom surface of the assembly beaker. In Appendix C, the steps of the computations and the adjustment of the power intensity are presented in detail. For the liquid properties such as density $\rho_{mixture}$ and viscosity $\mu_{mixture}$, the properties of acetone are used because the host liquid in the proof-of-concept is mostly acetone (95%), and the difference

between acetone and water is small.

The calculated radiation force of approximately 7 x 10^{-22} N is much smaller than both the lift-off retention force of about 10^{-8} N and the gravitational force of about 10^{-14} N. Therefore, it is clear that the components are not removed by a direct lift-off mechanism. This leaves only a roll-off mechanism. The three linear forces (added mass, drag, and Basset) can contribute to roll-off based on the rolling mechanism as proposed in Figure 5. 1. The roll-off torque is calculated as the product of the magnitude of the resultant force of the linear forces and the load eccentricity of about 0.2 μm, which is related to the distance up the hole sidewall at which the sphere sits. It was found that the removal torque calculated based on the resultant force of eq. (5.12) is *comparable* to the previously calculated retention torque of $1.5x10^{-17} \sim 4.4x10^{-17}$ Nm, which, therefore, satisfies the first criterion as well as the second criterion.

In conclusion, a removal theory is proposed in which *the torque induced by the linear forces rolls microspheres out of mismatched holes irreversibly, with magnitudes that are competitive with the retention torques.* The acoustic streaming drag force, which is nonlinear, and thereby irreversible, can also contribute to removal by roll-off, but does not have sufficient magnitude to be the dominant removal mechanism for the present case as shown in Table 5.1. Among the individual forces, the Basset force is the dominant

contributor to the resultant torque for the first, proof of concept experiment with 1.6 micron spheres. However, a different force could drive the roll-off mechanism for other component sizes or ultrasound frequencies. The scalability issue is discussed in Section 5.2.

Two indicators, the net removal torque and the ratio of retention torque to removal torque based on the proposed removal theory, were chosen to quantitatively examine the correlation of the assembly rate with removal torque and retention torque. In Figure 5. 5 (a), the assembly yield rate is plotted versus the net removal torque, which was computed by subtracting the retention torque from the resultant removal torque. The net removal torque varies from -0.5×10^{-17} Nm to 2.5×10^{-17} Nm as the assembly yield increases from 0% to 100%. However, in the calculations of the retention torques, the removal torques, and the net removal torques, the values for interfacial energy (γ), characteristic length of the hydrophobic force (d_c), and power efficiency of the transducer (η) are adopted with uncertainties such that d_c=1.5 +/-0.5 nm, γ=5 +/– 0.5 mJ/m^2, and η =0.2 +/-0.1. The given uncertainties of the values above do not indicate a statistical range from this experiment but rather a quantity that is either variably reported in the literature (d_c) or difficult to characterize in the experiment (γ, η). The characteristic length of the hydrophobic force d_c uses the typical range chosen in literature.[16,22] The variation of

interfacial energy γreflects the variation observed in the contact angle measurement. The variation of the power efficiency of the transducer reflects the uncertainty of experimentally estimating the efficiency. All these uncertainties are combined and presented with error bars for the net removal torques in Figure 5. 5(a). The range of the error bars is +/- $3x10^{-17}$ Nm, and the error bars are set between the minimum and the maximum torque values that can be calculated based on the uncertainty ranges given above. The uncertainties associated with assumptions for the roughness calculation were not included because they are not quantitatively assessable. In Figure 5. 5 (b), it was also found that the ratio of the retention torque to removal torque varies over the range of the proof-of-concept experiment. The error bars of these ratios correspond to the error bars of the net torques, which are based on the limits of the uncertainties. As expected from the first assembly criterion, the two indicators (the net torque and the ratio) demonstrate that the variation of the assembly rate was significant only when the retention and the fluidic removal effects are commensurate (the ratio between 0.6 and 1.5) in magnitude.

The theory described above was proposed for spheres that are smaller than the holes, but it is expected to apply equally to the assembly of the larger spheres into smaller holes. The configuration of the contact area will simply be different for the larger sphere-small hole case. When a microsphere is larger than a hole, the contact of the microsphere with

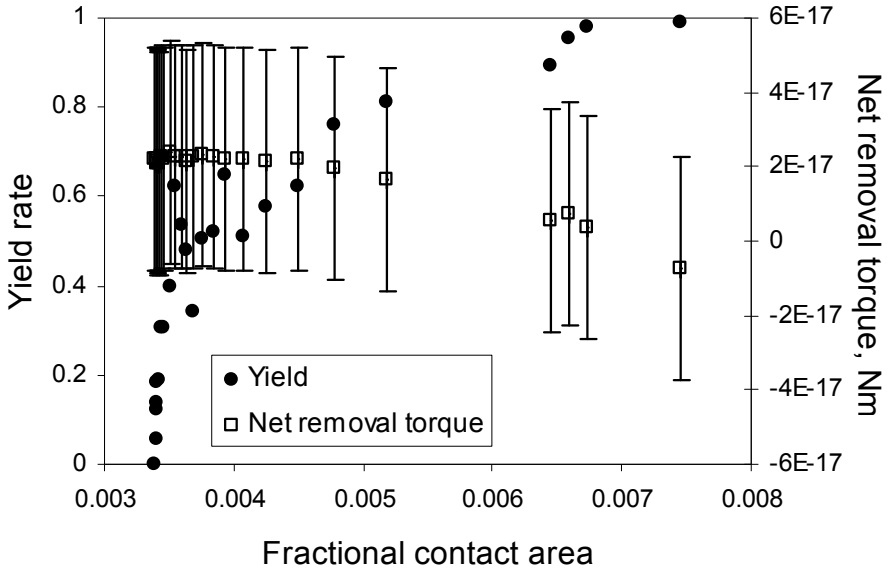

(a)

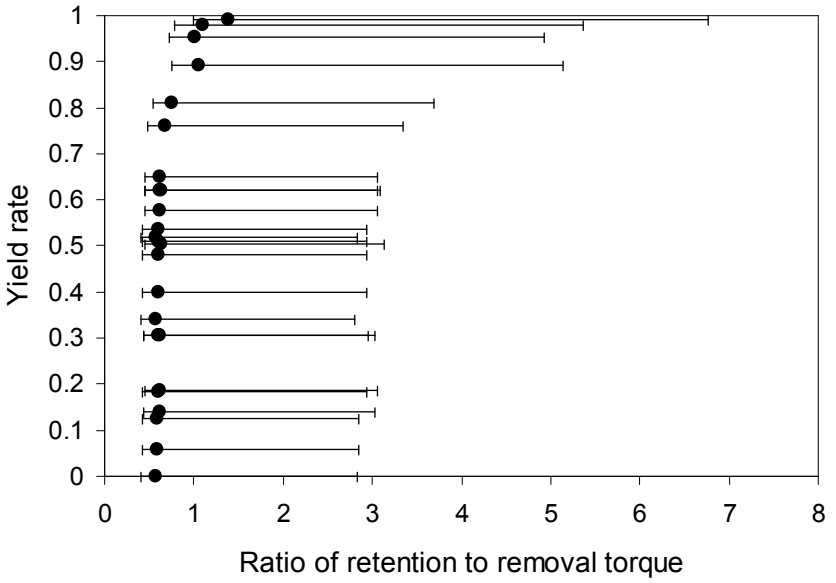

(b)

Figure 5. 5 (a) Measured yield versus nominal fractional contact area (left axis) and calculated net removal torque versus nominal fractional contact area (right axis) with the error bar of +/- $3x10^{-17}$ Nm. (b) Yield versus ratio of retention torque to removal torque with the corresponding error bar.

the hole follows the circular line of the brim of the hole, whereas a microsphere sitting inside a hole makes contact to an area that is locally confined to the effective contact point. A large microsphere in contact with a hole has a contact area that follows the perimeter of the hole, forming a circular band (Figure 5. 6). When a large microsphere rolls off of a small hole, there is a large rate of change of contact area because of the large distance of the contact surface from the rolling point. As a result, the removal of large spheres from small holes may entail fluidic forces/torques of greater magnitude than for the case of microspheres smaller than holes. The validity of the proposed theory for this case must be verified by experiments. The assembly experiments, in which the microspheres are larger than the holes, were carried out and are presented in Chapter 6. It will be seen that the proposed theory adequately predicts the results of these experiments.

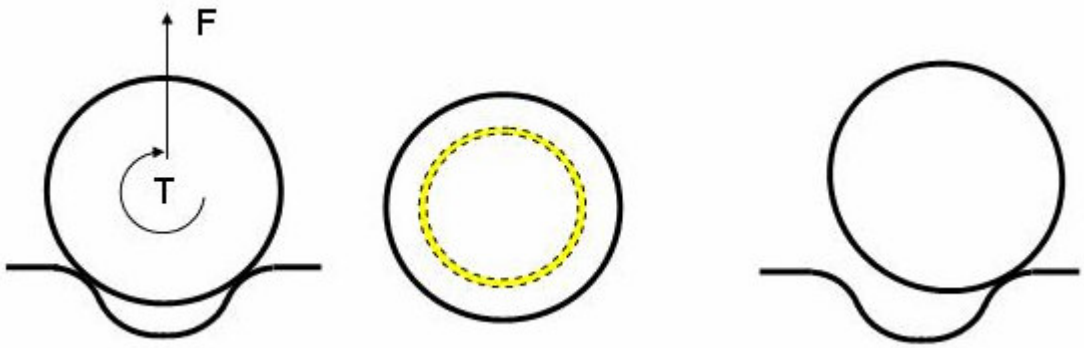

Figure 5. 6 Schematic of microsphere greater than hole. (a) Side view (left) and top view with contact area indicated by the ring of dashed lines (right). (b) Roll-off of the microsphere.

5.2 Model verification

The theory is supported by the fact that yield is seen to increase when retention effects become dominant over removal effects. However, due to the considerable difficulty of inspection into the mechanism at the micron length scale and the microsecond time scale, a visual and direct verification for the removal mechanism proposed in the theory was not available. The theory, therefore, was indirectly verified by addressing these other mechanisms and establishing that the other mechanisms could not explain the observed selectivity. Capillary force needs to be most carefully examined for the present assembly system because this force has been used to drive assembly into templates at the intermediate scale in experiments that have some similarities to the present assembly system. In the previous work using capillary forces, the contribution of the capillary forces was usually made when the liquid contact line swept across the surface on removal of the substrate from the assembly fluid.[4,11,12] The question with the present assembly is whether capillary forces drive assembly of components when the substrate is removed from the beaker.

It was seen experimentally that when the ultrasound conditions are appropriate for selective assembly, the holes that should be empty are empty after the substrate is removed

from the liquid. In addition, increasing ultrasonic intensity was seen to reduce assembly rate. Therefore, capillary forces on substrate removal do not add excess components. This is as expected, because the substrate is removed from the upper surface of the liquid, where the population of components is small. Few components would be available to be assembled by capillary forces. A second question is whether capillary forces are responsible for the observed selective removal. To experimentally investigate the contribution of capillary forces to selectivity, assembly was conducted without ultrasonic excitation. In the absence of ultrasound, a large number of holes were filled with spheres, but not selectively. Spheres in poorly matched C and D holes remained partially assembled, in contrast to the mostly empty C and D holes when ultrasound was applied. This shows that capillary forces do not selectively remove randomly-assembled spheres against the retention force. Therefore, capillary forces cannot account for the observed selectivity.

5.3 Scalability of assembly approach and model

The theory was proposed based on the assembly experiment with 1.6 μm microspheres. However, removal forces and retention forces vary with size and, therefore, the limits of the theory need to be explored. This section is dedicated to the study of theoretical

predictions of the scalability based on the dependence of each force on the size of the microsphere. Assembly experiments on different scales are presented in Chapter 6 to verify the predictions. In this theoretical study, the retention force is assumed to be proportional to the size of the microsphere for simplified quantification of the retention force. Also, along with the resultant force, each removal force contributing to the torque is individually examined with the retention force in order to understand the contribution of each fluidic force and identify the dominant mechanism at each different scale.

First, for the Basset force, the ratio of retention torque to removal torque for spheres can be roughly expressed as

$$\frac{\mathrm{T}_{\mathrm{Retention}}}{\mathrm{T}_{\mathrm{Removal}}} \propto \frac{\gamma R_s^2}{R_s^3\sqrt{If}} = \frac{1}{R_s}\frac{\gamma}{\sqrt{If}} \tag{5.16}$$

where the proportionality constant does not depend on frequency or intensity. For the retention torque it should be noted that the contact area is roughly proportional to the radius of the spheres rather than the radius squared; the definition of the contact area involves both the radius and the characteristic length of the hydrophobic force, so that the contact area must be proportional to both force characteristic length and radius to be dimensionally correct, and further if the contact area is a very small fraction (a few percentages) of the total surface area of a microsphere, which was found in the present case, then the contact

area can be easily estimated by $\frac{2\pi d_c R_s R_h}{R_h - R_s}$ where $\frac{R_s R_h}{R_h - R_s}$ is the equivalent radius of two surfaces in contact as shown in Figure 4. 8 (or reciprocal of the relative curvature of the two surfaces) and R_h is a local radius of a hole. As indicated in (5.16), the contribution of the Basset force is proportional to the radius squared and will diminish with smaller size. In contrast, the viscous drag force is linearly proportional to the radius of the sphere, so the ratio of retention torque to removal torque for the viscous drag is independent of the component size, with

$$\frac{\mathrm{T}_{\mathrm{Retention}}}{\mathrm{T}_{\mathrm{Removal}}} \propto \frac{\gamma R_s^2}{R_s^2 \sqrt{I}} = \frac{\gamma}{\sqrt{I}}. \tag{5.17}$$

For the roughly 1 μm scale components of the experiment presented in 5.1, the ratio for viscous drag is only about ten times less than the ratio for Basset force. Holding all else constant, the ratio for viscous drag will equal the ratio for Basset force when the component radius is reduced by a factor of ten to the roughly 100 nm scale, and removal by viscous drag will be dominant for further reductions in component size. The added mass force may be neglected for small R_s based on

$$\frac{\mathrm{T}_{\mathrm{Retention}}}{\mathrm{T}_{\mathrm{Removal}}} \propto \frac{\gamma R_s^2}{R_s^4 f \sqrt{I}} = \frac{\gamma}{R_s^2 f \sqrt{I}}. \tag{5.18}$$

Removal by acoustic streaming may also be neglected because the resulting torque has been shown to be orders of magnitude smaller than the torques due to the other forces.

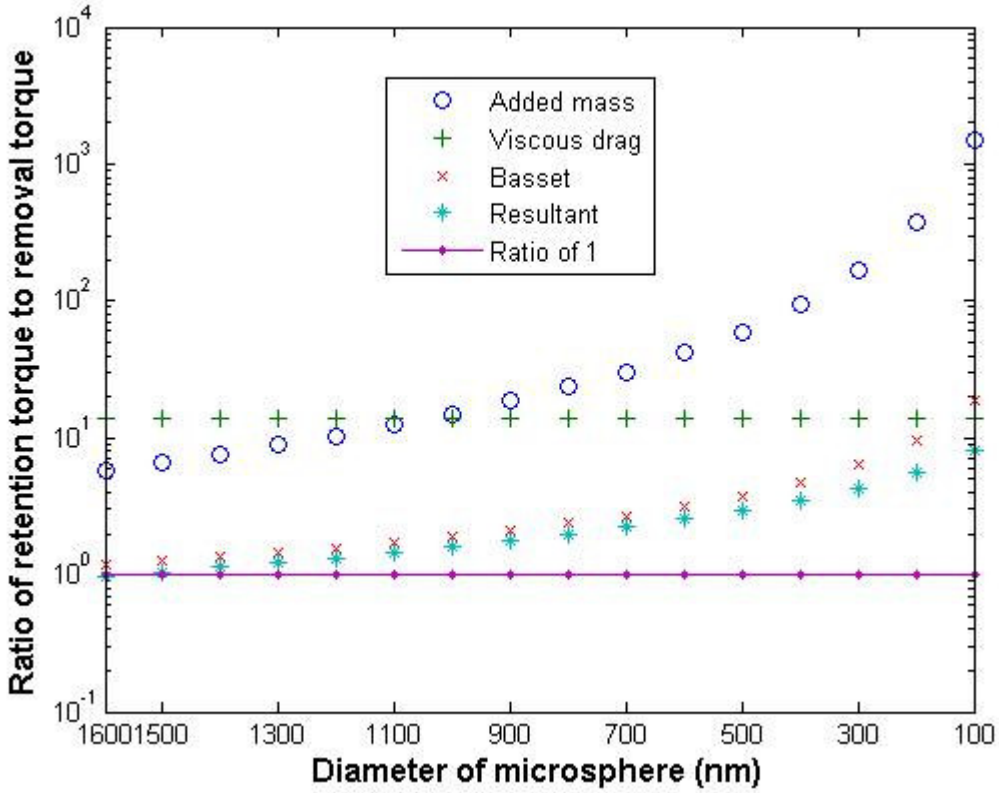

Figure 5. 7 Ratios of retention torque to removal torque. The line of Ratio 1 is a guide to the eyes and demonstrates how comparable each fluidic torque is to the retention torque. .

Finally, the resultant force is almost close to the Basset force with a small deviation, which increases with smaller size. The dependence of $\frac{T_{Retention}}{T_{Removal}}$ for individual forces and the resultant force on component size is demonstrated in Figure 5. 7.

The dependence of $\frac{T_{Retention}}{T_{Removal}}$ of each fluidic force on component size determines what drives selective removal at size scales below those demonstrated in the proof of concept experiment; for selective removal, the ratio of $\frac{T_{Retention}}{T_{Removal}}$ should be close to one, which is equivalent to the magnitude criterion in Section 5.2. Although the resultant torque is the

one that truly acts on a microsphere, each fluidic force and its ratio with the retention force needs to be examined to be able to effectively control the removal torque at each different scale. As demonstrated in Figure 5. 7, the resultant force mostly stems from the Basset force down to 100 nm. Therefore, it can be argued that any deficiency of removal force at smaller scale down to 100nm as observed in Figure 5. 7 needs to be adjusted basically by tuning the Basset force with its control parameters, which is in the form of $\gamma/\sqrt{If}$. As R_s decreases by a factor of about ten to the 100 nm scale, $\gamma/\sqrt{If}$ must be adjusted to keep $\frac{T_{Retention}}{T_{Removal}}$ due to the Basset force close to one, for example by decreasing interfacial energy by using less water or increasing ultrasound intensity. Although this tuning method has some limitations, such as reduced intensity at higher frequencies, the necessary order of magnitude increase in $\gamma/\sqrt{If}$ is feasible. For further reductions in component size, viscous drag makes more contribution and it equals the Basset force at the microsphere diameter of 100nm. In the vicinity of 100 nm, therefore, the Basset force and the drag should be collaboratively controlled. Much below 100nm, the viscous drag becomes dominant. Because $\frac{T_{Retention}}{T_{Removal}}$ due to viscous drag is independent of component size, smaller components may be removed without any additional power or frequency increase as far as the drag force and the retention force are comparable at 100 nm. In order to verify the scalability, assembly experiments were conducted with microspheres of the

diameters of 1.6 μm, 0.88 μm and 0.432 μm. The results are presented quantitatively assessed as shown in Section 6.3.

6 Experimental validation of the model

Additional experiments were conducted in order to explore the limits of applicability of the present assembly technology as well as to verify the validity of the proposed selective removal mechanism, which was proposed based on the first proof-of-concept experiment. Topics to be explored in this chapter include changes in the experimental set-up for this second set of experiments (Section 6.1), repeatability of the experiments (Section 6.2), scalability to smaller sizes and circulation of components (Section 6.3), sensitivity to ultrasonic power level (Section 6.4), and assembly of spheres into holes that are smaller than the spheres (Section 6.5). On each topic, the relevant experimental results are presented and correlated with the proposed selective removal mechanism.

6.1 Experimental set-up

The layout of the pattern for this experiment is basically similar to those for the proof-of-concept experiment (see Section 4.1). The main difference is that nine different exposed sizes were introduced into each array in order to observe the gradual transition of yield rate between the nine different match qualities within a single array (Figure 6. 1). This layout can minimize the spatial non-uniformity in the assembly set-up, while also providing enough data (9 pairs of yield rate and hole size) to capture the assembly

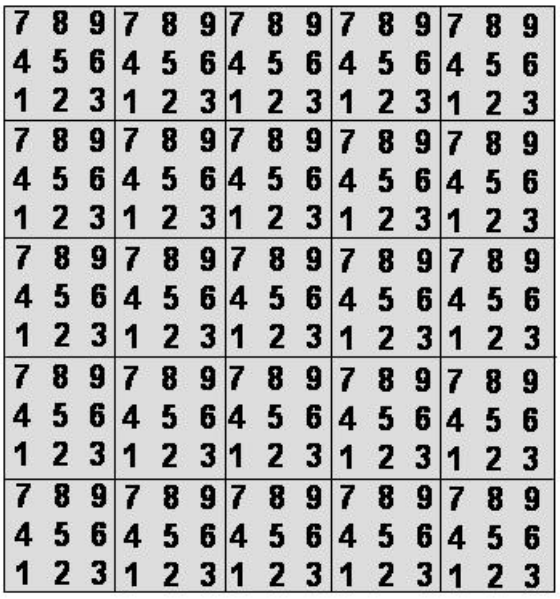

(a)

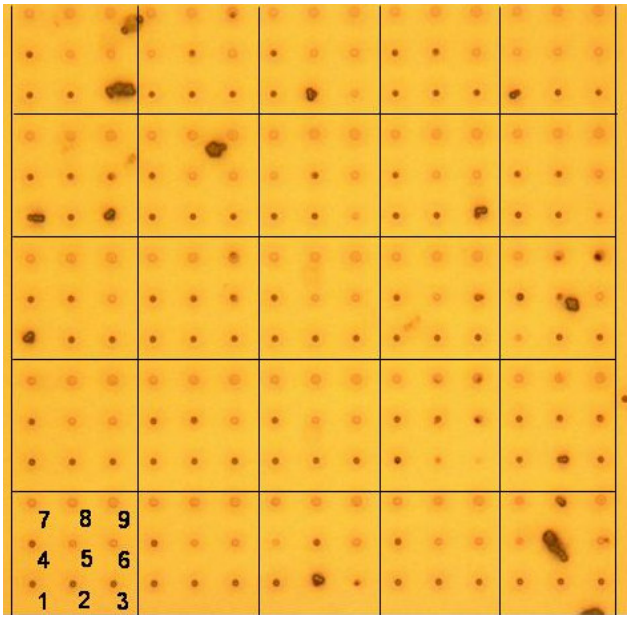

(b)

Figure 6. 1 Layout of repeated pattern of 9 hole shapes (1, 2, 3, 4, 5, 6 7, 8, 9). (a) Schematic of the array of a repeated pattern of 9 holes shapes. Grid lines are guides to eyes and identify groups of type 1, 2, 3, 4, 5, 6 7, 8, and 9 holes. (b) The pattern on template corresponding the layout of (a). Grid lines are drawn to identify the corresponding group of type 1, 2, 3, 4, 5, 6 7, 8, and 9 holes of (a). Big blotches are images of clusters of microspheres.

selectivity. The smallest type number, 1, indicates the minimum exposure spot and the largest type number, 9, indicates the maximum exposure spot. The nominal exposed spot sizes for each hole type are as follows: 1=50nm, 2=75nm, 3=100nm, 4=150nm, 5=200nm, 6=300nm, 7=400nm, 8=550nm, 9=700nm. Therefore, after etching, the hole shape of type 1 becomes the most hemispherical (and thereby, the most matched to a microsphere), whereas the hole shape of type 9 has the largest opening width and the poorest match to the hemisphere shape. To create the template substrate, a silicon wafer was thermally oxidized to form a silicon dioxide layer of 1 μm, as presented in Chapter 3. A 100nm layer of PMMA for e-beam lithography was spun on the surface. It was found that exposure dose has a weak effect on the size of holes for this thin PMMA layer, so exposure variation was not included for the design of the pattern. Etching of the silicon oxide to create near-hemispherical holes followed the same procedure as in the proof-of-concept experiment. However, the difference from the proof-of-concept experiment is that different templates have different etching times. The different etch times create different depths (0.23 μm, 0.415 μm, and 0.8 μm) of holes commensurate to microspheres of different diameters (0.216μm, 0.44μm, and 0.8 μm) for the scalability study presented in Section 6.3. The surfaces of the templates and the microspheres were coated with octadecyltrichlorosilane and octyltrichlorosilane respectively in the same way as presented

in Chapter 3. Experiments under different sets of assembly conditions were carried out in the assembly system presented in Chapter 3 to observe the effects of varying the assembly parameters. For the repeatability test, multiple experiments under a nominally identical set-up were repeated and their results were compared. For the study of dependence on ultrasonic power, the assembly yields were measured after assembly experiments were conducted at four different power levels. For the study of scalability, experiments were carried out with microspheres of each different size.

6.2 Assembly repeatability

This study measures repeatability of the assembly experiment. The diameter of the microspheres used for this study was 880nm. All other experimental and layout details are set as explained in Section 6.1. The repeatability experiments were all performed on the same template to exclude the possibility of manufacturing variation between templates. This template was patterned with holes commensurate to the 880 nm microspheres. Microspheres were assembled into the template as described previously for the proof of concept experiment. After each experiment, the results were recorded with an optical micrograph, and the assembled components were counted to determine yield. The assembled microspheres were completely removed from the template by immersing the

template in ethanol and sonicating it for 30 seconds after each run, and the template was then reused for the next run. Four runs of the assembly experiment were conducted under the same assembly conditions. The variation between the nominally identical experiments is demonstrated in Figure 6. 2. The variance of the yield rate reflects the combination of non uniformity of the fluid field and the reproducibility of the experimental set-up. If there is a small spatial displacement of the template in the beaker from one run to the next, there will be a corresponding variance of the assembly yield rate because the fluid field is not spatially uniform, as will be discussed in detail in Section 6.3.4. Therefore, in order to minimize the variance, the assembly system should be more tightly controlled with control parameters to be identical at each set-up. Alternatively, the assembly system could be designed to make the fluid field more spatially uniform, or the template could move slightly during the assembly, in a controlled pattern, in order to average across the different parts of the fluid field. It should be also noted that in Figure 6. 2 (b), the variation of the yield rate peaks at an averaged assembly rate of 45 %, which corresponds to type 5 holes. The near 50% assembly rate for these holes indicates that the averaged retention torque of type 5 holes matches the fluidic removal torque in magnitude i.e. the averaged net removal torque (averaged retention torque subtracted by the fluidic torque) is zero. Assuming that the retention torque of each hole type follows a normal distribution, where most of hole

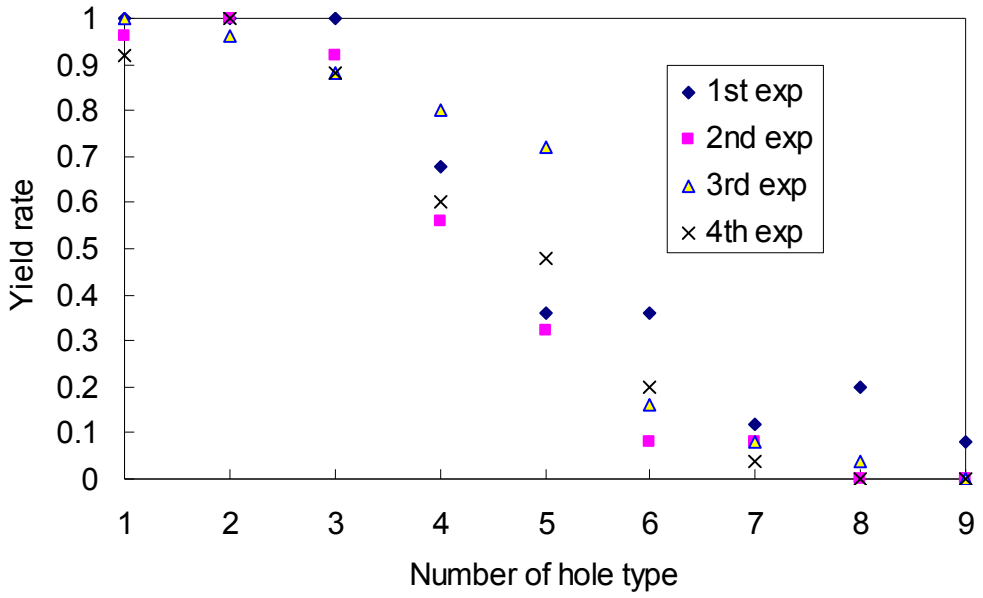

(a)

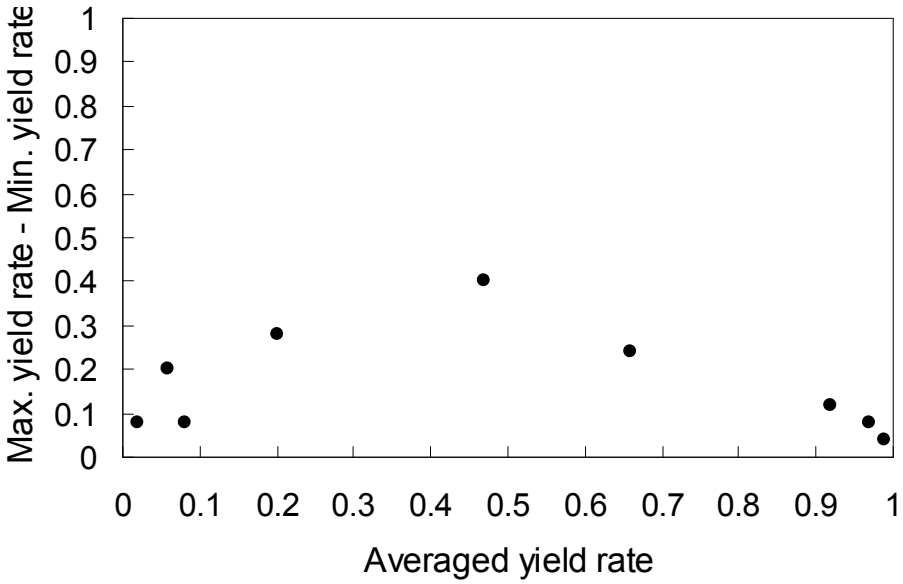

(b)

Figure 6. 2 Repeatability of yield rate. (a) Yield rate versus number of hole type. (b) Maximum yield rate subtracted by minimum yield rate versus the corresponding average yield rate from (a).

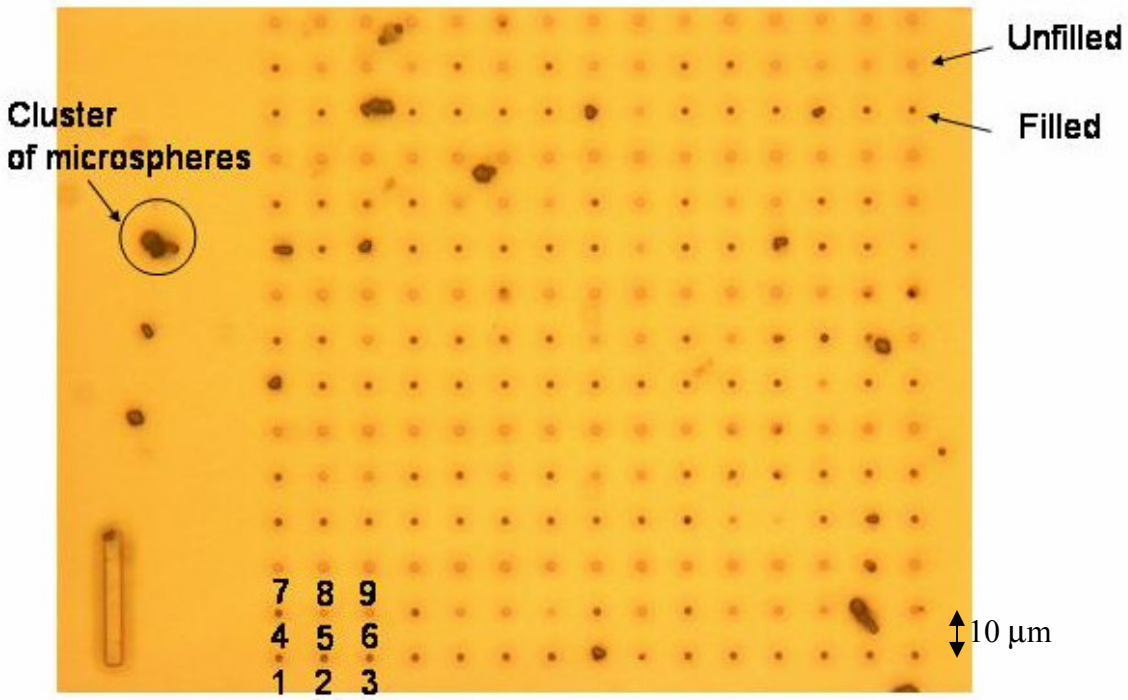

(a)

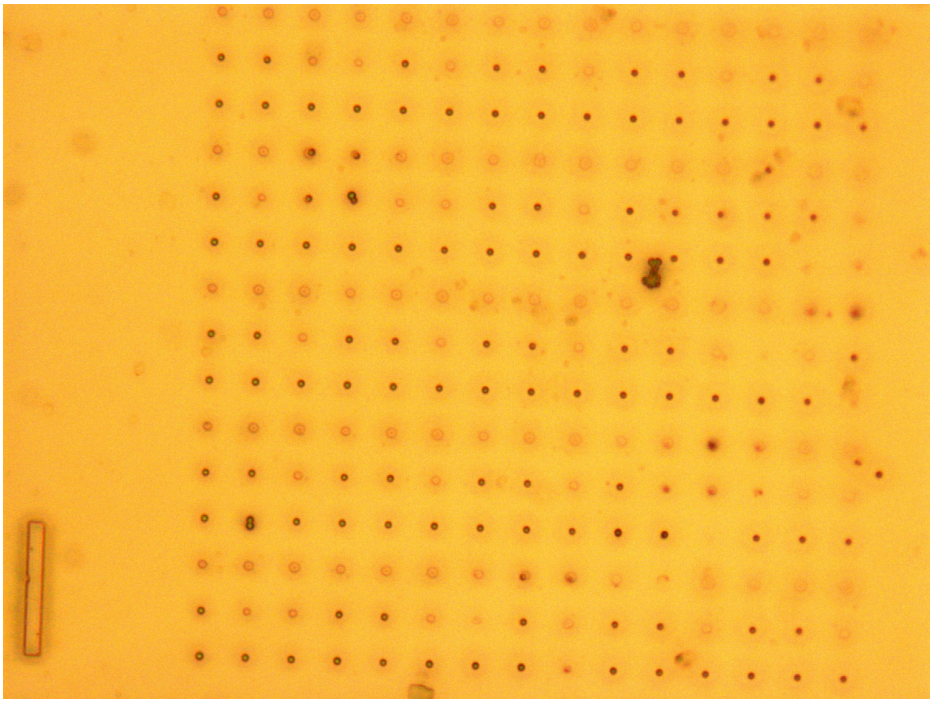

(b)

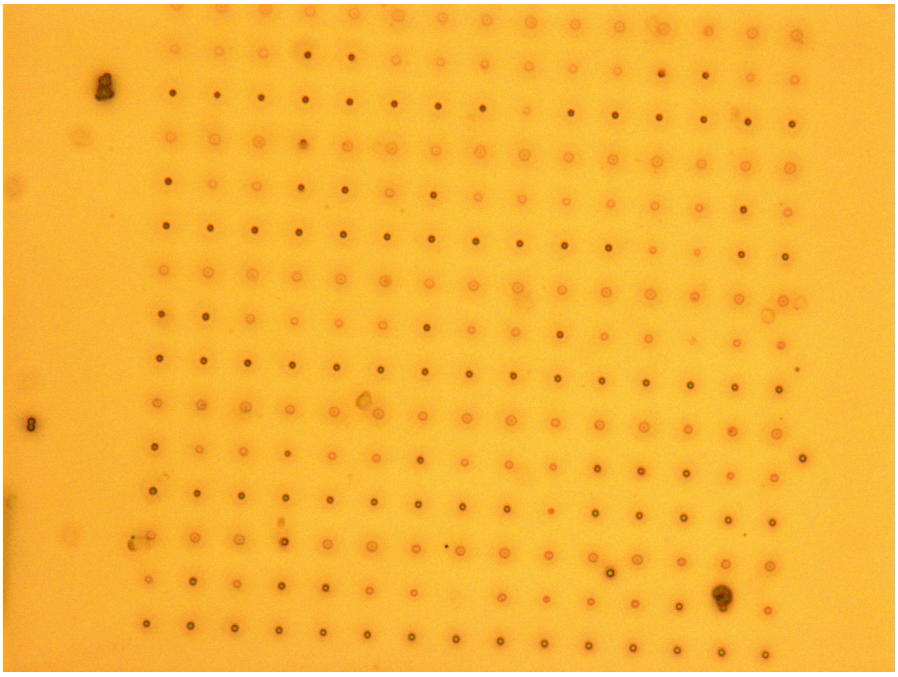

(c)

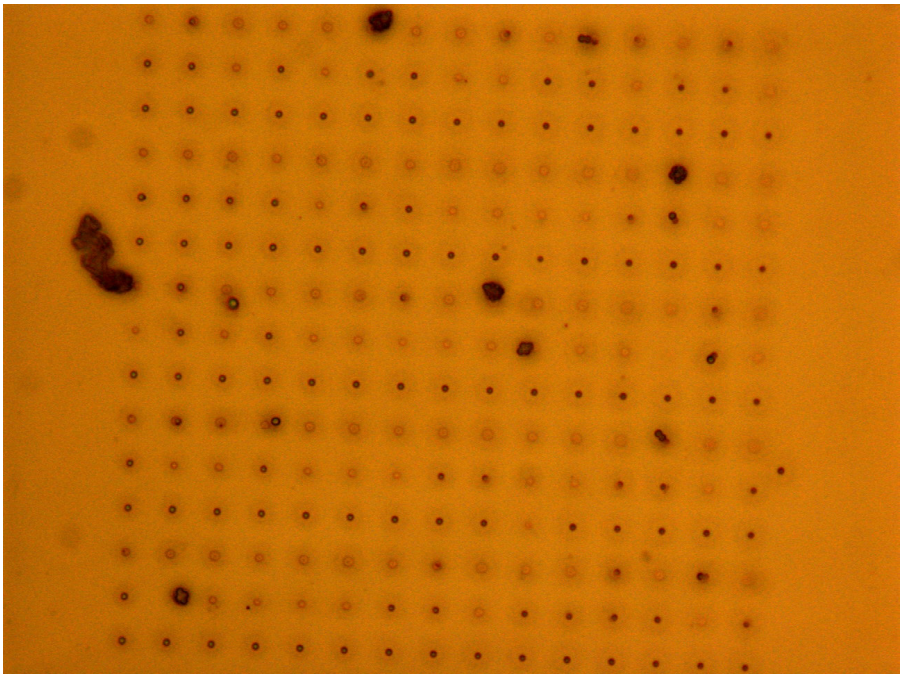

(d)

Figure 6. 3 Template after each repeatability experiment. Filled holes appear darker as indicated in (a). Clusters of microspheres are also shown. (a) 1st experiment. (b) 2nd experiment. The image is tilted. (c) 3rd experiment. (d) 4th experiment.

population lies around the average, then, most of type 5 holes have their retention torques equal to or close to the fluidic torque (i.e. their net removal forces/torques are equal to or close to zero). Therefore, in response to a small perturbation, many of the net removal forces/torques of type 5 holes would be subject to a sign change, thereby potentially creating large variation in the yield rates of the repeatable experiments (i.e. less repeatable). With respect to each individual hole, the assembly was more repeatable at the holes of the bottom row (holes type of 1, 2, and 3) and the top row (hole type of 7, 8, and 9) of the repeated pattern as shown in Figure 6. 3; their yield rates are closer to 0% or 100%, which are expected from the previous discussion. Figure 6. 4 shows the yield rate versus fractional contact area of the repeatability experiments. The scattering ranges of the yield rates as shown in Figure 6. 2 (b) can be incorporated with the assembly results in the following sections.

6.3 Assembly experiments with various size microspheres

Three different assembly experiments for three different sizes of microspheres were conducted in order to explore the scalability of the approach and validate the proposed theory. Results and discussion are presented for each size. It is shown below that the previously-proposed selective removal model does not fully describe the results of these experiments, particularly for the smallest components. This discrepancy is attributed to

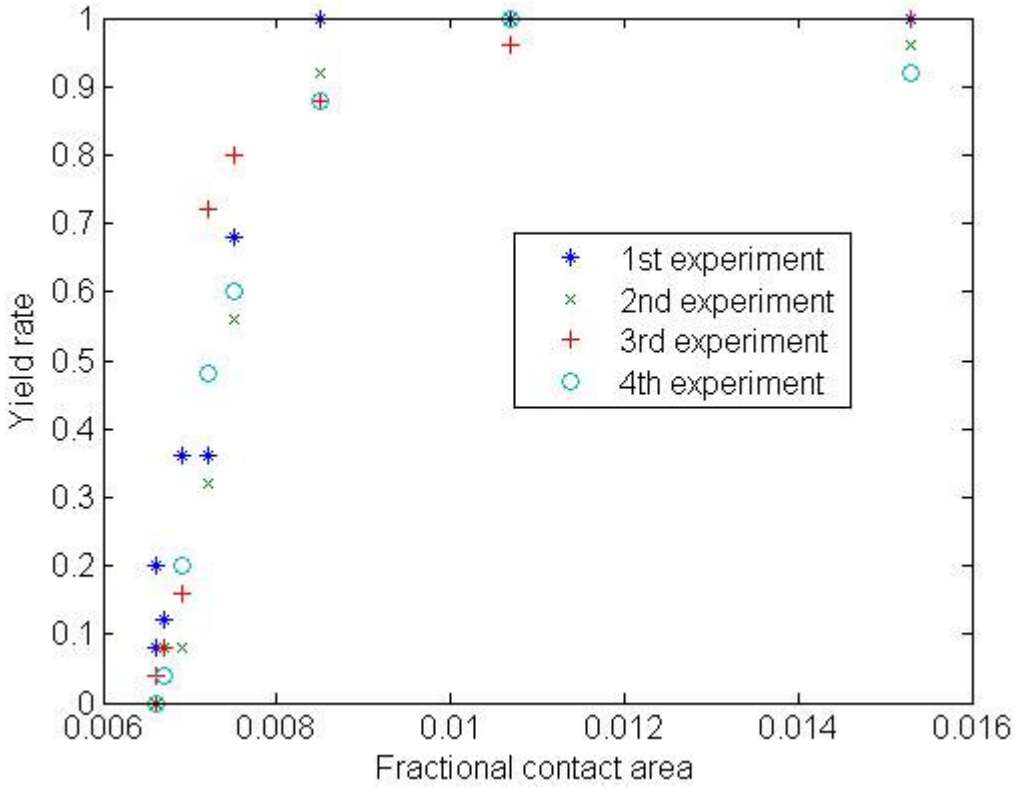

Figure 6. 4 Yield rate versus contact area in a repeatability test.

the difficulty of circulating the smallest components in the assembly fluid. If the components do not circulate, it can not be assumed that the components contact potential binding sites frequently. In this section, the mechanism of component circulation is added, and its dependence on size is discussed in order to adequately describe the observations with the smallest scale components (diameter 0.432 μm).

6.3.1 Microspheres of 1.6 μm

The diameter of the microspheres used in this experiment is 1.6 μm and the depth of

the hole in the template is nearly the radius of the sphere, which is 0.8 μm. Although the experimental results are similar to those of the proof-of-concept experiment, which used microspheres of the same size, the present assembly experiment was conducted in order to provide a more consistent reference to compare with the assembly results at smaller sizes. For the present experiment, the mixture of the assembly fluid consists of 25% water and 75% acetone, and the transducer generating the ultrasound was set to a higher power level than in the proof of concept experiment with an 85 volt input. The rest of the experimental details follow Section 4.1. With nine data points, the gradual transition of

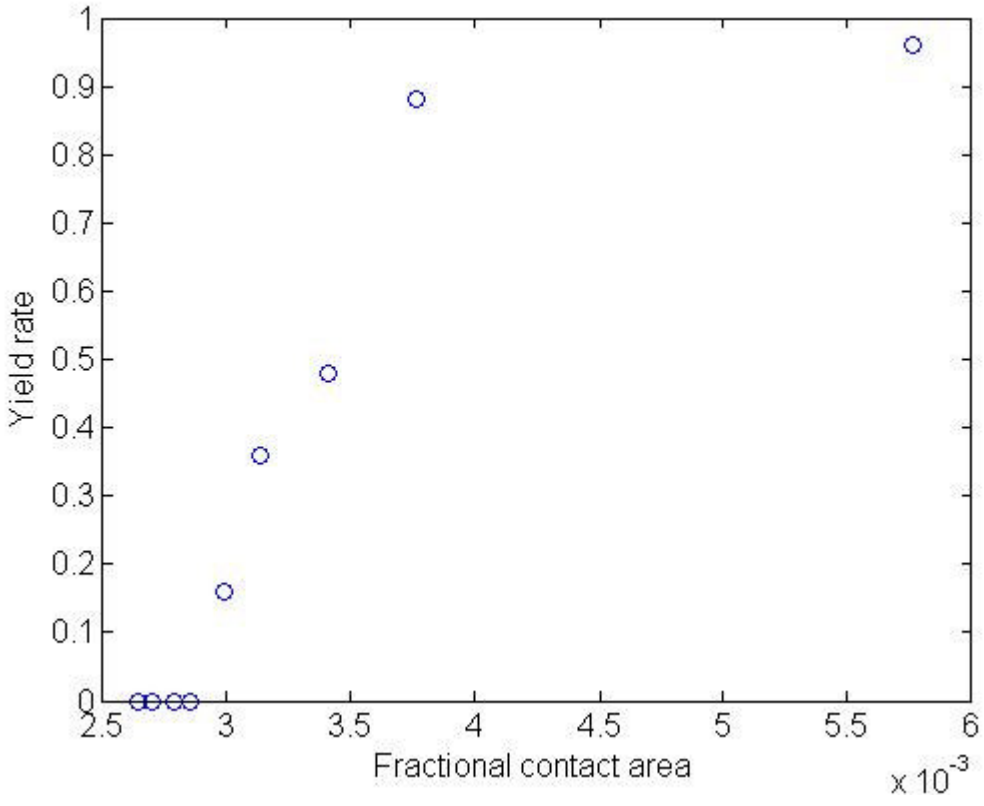

Figure 6. 5 Yield rate versus fractional contact area with microspheres of 1600nm.

the assembly yield with respect to contact area (which was estimated as previously explained) is demonstrated in Figure 6. 5. The results are similar to those that were observed in the proof-of-concept experiment.

6.3.2 Microspheres of 0.88 μm

The diameter of microspheres used in this experiment is 0.88 μm, and the depth of the hole in the template is 0.42μm, which is close to the microsphere radius of 0.44 μm. The present experiment used the same mixture ratio of the assembly fluid and the same power from the ultrasonic transducer (85 volt input) as were used in the assembly experiment with 1.6 μm microspheres. With nine data points, the gradual transition from near 0% to 100% yield rate with respect to contact area is demonstrated in Figure 6. 6

6.3.3 Microspheres of 0.432 μm

The diameter of the microspheres used in this experiment is 0.432 μm, and the depth of the hole in the template is 0.23μm, which is close to the microsphere radius of 0.216 μm. The experimental set-up used the same mixture ratio of the assembly fluid as in the previous experiments with larger microspheres. With the input voltage of the ultrasonic transducer set at 85 volts, no assembly was observed. However, when the voltage was increased to 95 volts, the yield increased. This experimental result was unexpected based.

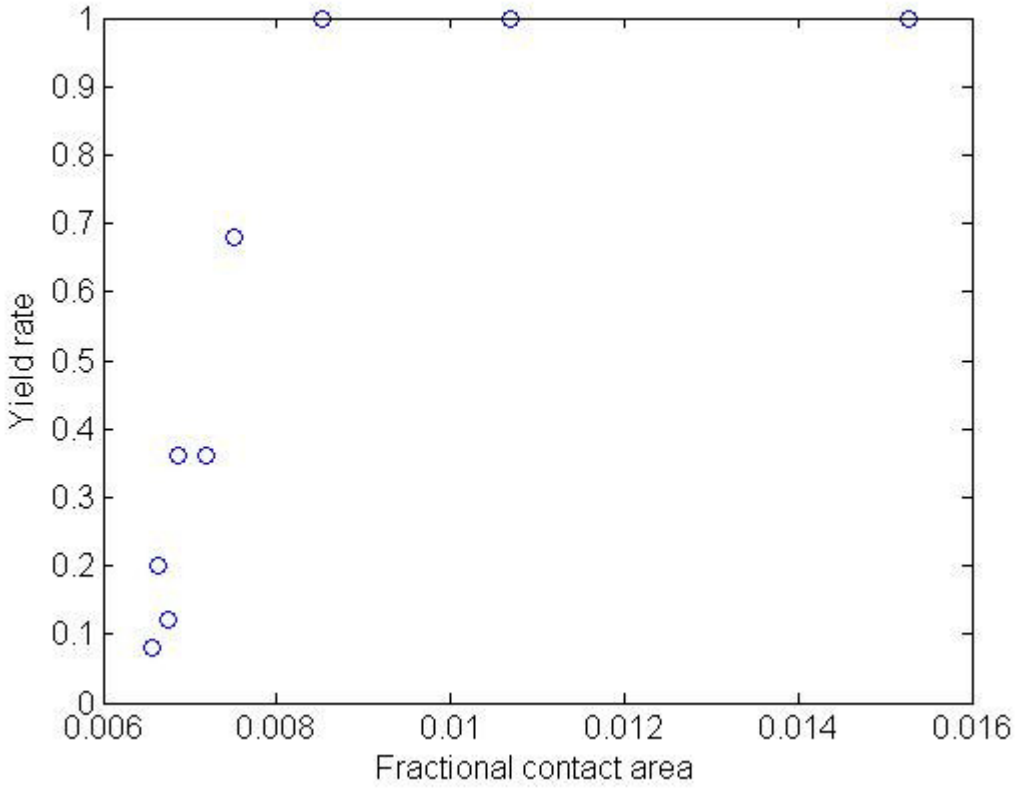

Figure 6. 6 Yield rate versus fractional contact area with microspheres of 880nm.

on the theory and theoretical scalability study. The theory states that retention force increases with smaller size. Therefore, theoretically, yield rates are expected to be higher for microspheres of smaller size at the same input power level. This inconsistency required an adjustment to the theory, namely a study of the role of component circulation. The study of component circulation will be presented in detail later, in association with acoustic streaming.

With nine data points, the gradual transition of the assembly yield with respect to

contact area is demonstrated in Figure 6. 7 for a transducer input voltage of 95V. It should be noted that the range of the transition is limited compared to those of the larger microspheres. The low yield rate is 30%, and the high yield rate is 85 %. The ratio of $\frac{T_{Retention}}{T_{Removal}}$ based on the resultant force lies between 1 and 3.1, implying that retention effects are dominant over removal effects. This limited range of yield rate can not be fully explained by the removal theory, which is deterministic with the ratio of $\frac{T_{Retention}}{T_{Removal}}$ only when the assumption of random component circulation is valid. The removal theory implicitly assumes that a random mixing (turbulent-like) flow ensures the encounter of a microsphere with each hole, as long as there are excessive numbers of microspheres. However, as seen in the real time observations presented later, it was found that the component circulation is determined instead by mean flows. By detailed investigations presented later, the flow field induced by acoustic streaming is identified as the most prominent mechanism for in-plane circulation on the template surface, and further it was found that it seems to control the encounter of microspheres with holes through in-plane circulation. This also suggests that the assembly theory needs to be expanded to include the mechanism of the encounter as well as the mechanism of the removal. The details of the circulation mechanism are presented below, and the dependence of its contribution to the assembly on size is discussed in Section 6.3.4.

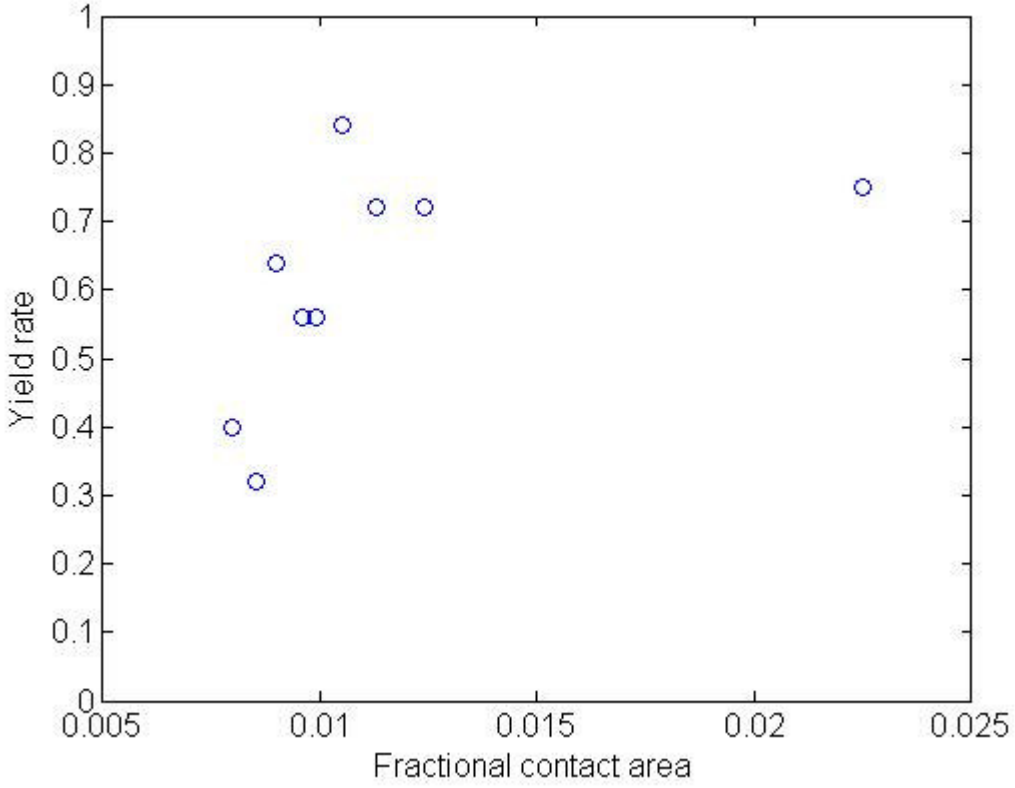

Figure 6. 7 Yield rate versus fractional contact area with microspheres of 432nm.

6.3.4 Circulation

This section is dedicated to identifying the dominant flow field for component circulation from several candidate flow fields. It then demonstrates how component circulation by acoustic streaming occurs and then contributes to the assembly. Finally the dependence of component circulation on size is discussed.

Circulation flows could possibly arise from either acoustic streaming or radiation pressure, which are all nonlinear flows with non zero means. Radiation pressure is

exerted on a body when the incident wave is reflected on the surface of the body. In the present assembly system, the direction of the radiation pressure is vertical because the wave travels vertically. However, based on the order of magnitude analysis given in Chapter 5, the radiation pressure is outbalanced by gravity and, therefore, circulation by radiation pressure is disregarded here.

As for the acoustic streaming, two types of flow fields may be induced in the assembly system. One flow field is associated with large scale Eckart streaming, and the other is similar to the field demonstrated by Kolb, Jackson and Nyborg,[31,32] where the first order flow field (oscillatory flow field) is treated as incompressible and the acoustic streaming flow is mostly induced by the gradient of tangential velocity on the surface. As shown in Figure 6. 8 and Figure 6. 9, the two fields are different in directions, and only one is the proper candidate circulation field with the present assembly system. Based on the works of Spengler and Jekel[33] showing that a short length along the traveling direction of the ultrasound wave prevents the large scale streaming, the large scale Eckart streaming is found to be unlikely in the present assembly system where the liquid contained in the assembly beaker bears only a short height (3 mm) compared to its width of 22mm. The elimination of Eckart streaming left only the field predicted by Jackson and Nyborg.[31] In the field of Jackson and Nyborg, two distinctive flows are expected. One is induced at the

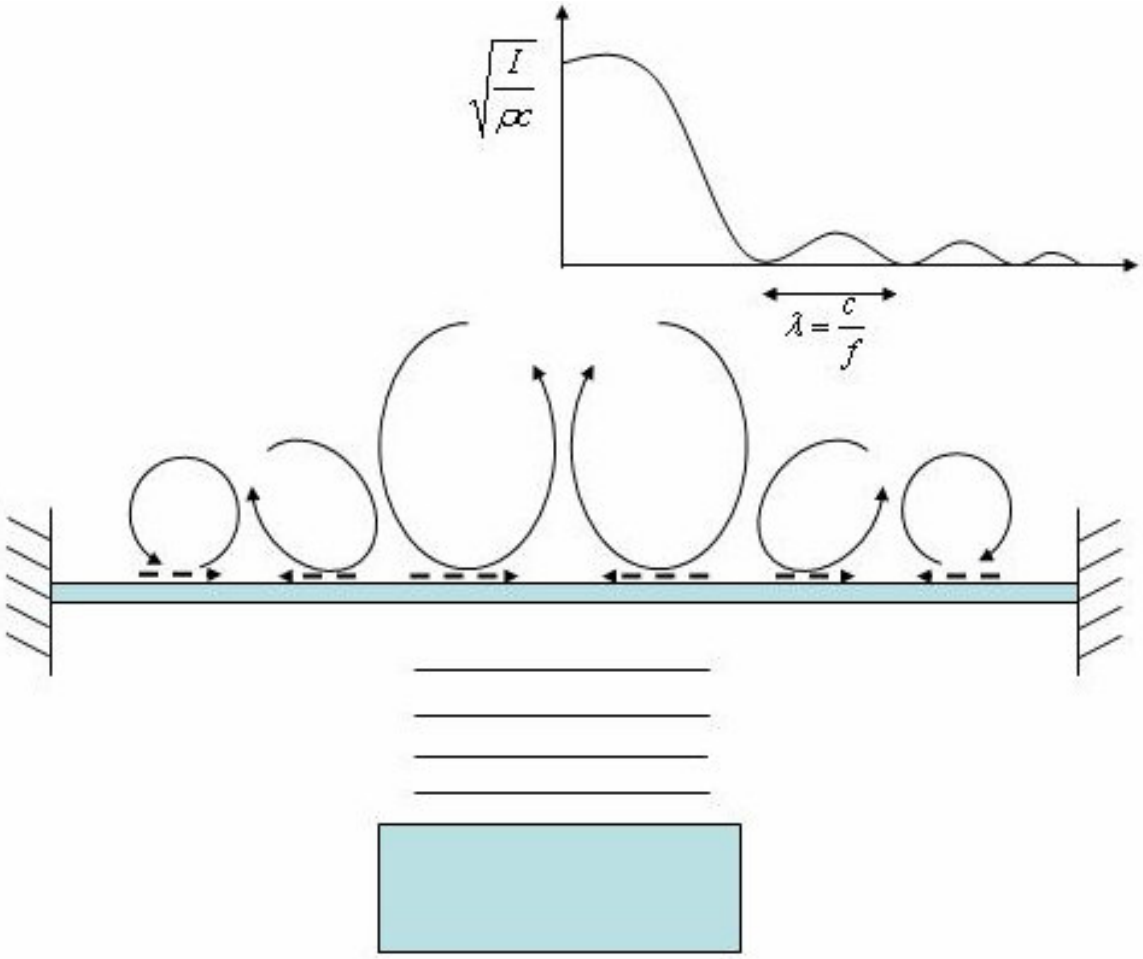

Figure 6. 8 Schematic of the Jackson and Nyborg flow field[31] of the assembly system. The top inset shows a distribution of ultrasonic intensity (or the displacement of the membrane) from the center. The intensity decays with distance from the center and a standing wave is introduced in association with the rigid assembly beaker sidewall. The solenoidal lines indicates the oscillatory flow velocity in the liquid and the dashed lines indicates the direction of acoustic streaming flows on the surface in accord with the oscillatory flow velocity.

periphery of the central driven area where the intensity of ultrasound is relatively high, and the other is associated with standing waves outside the driven area as shown in Figure 6. 8. With this flow field, the circulation of components is broken into two successive steps. First, microspheres follow the path of the circulation, which is downward to the surface,

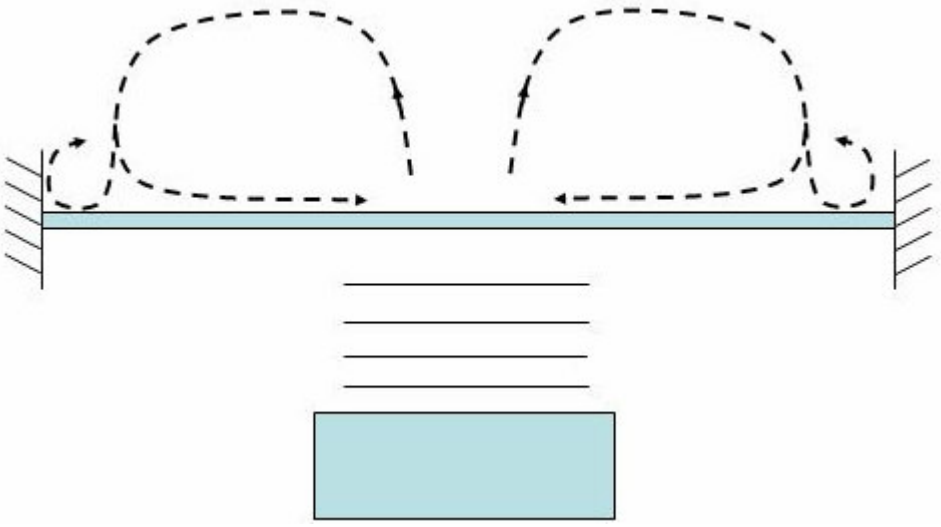

Figure 6. 9 Schematic of the Eckart flow field[28] in the assembly system. The dashed lines indicate the acoustic streaming flows.

and land on the surface at a few spots where the circulation flows meet with the surface. Then, after deterministically landing in a few specific spots, the microspheres begin to move laterally to the circular nodal lines of the standing wave (shown in Figure 6. 8) by boundary layer streaming. The beaker and the vibration pad of the ultrasonic transducer are both circular so that the nodes are set in a concentric pattern. In the flow field at the nodal points, two flows from two opposite directions meet and bend upward, which could lift the microspheres off the surface and back to the bulk liquid if the drag of the lifting flow outbalances gravity and hydrophobic interactions with neighboring microspheres. Figure 6. 10 shows a photograph of the assembly beaker from above. This image shows that the microspheres are distributed in a concentric pattern following the nodal circular

lines at the surface in the outer regions with the input voltage of the ultrasonic transducer set at 55 volts. This verifies the presence of the standing waves and, further, the validity of the predicted flow field. The observation of the pattern also indicates that microspheres remain at the nodal lines on the surface instead of being lifted away. The rings of the concentric pattern are separated by one half of the wavelength of the standing wave (0.8mm) and can affect the spatial uniformity of the assembly results. However, with higher input voltages, the concentric pattern is visually less distinctive. This implies that

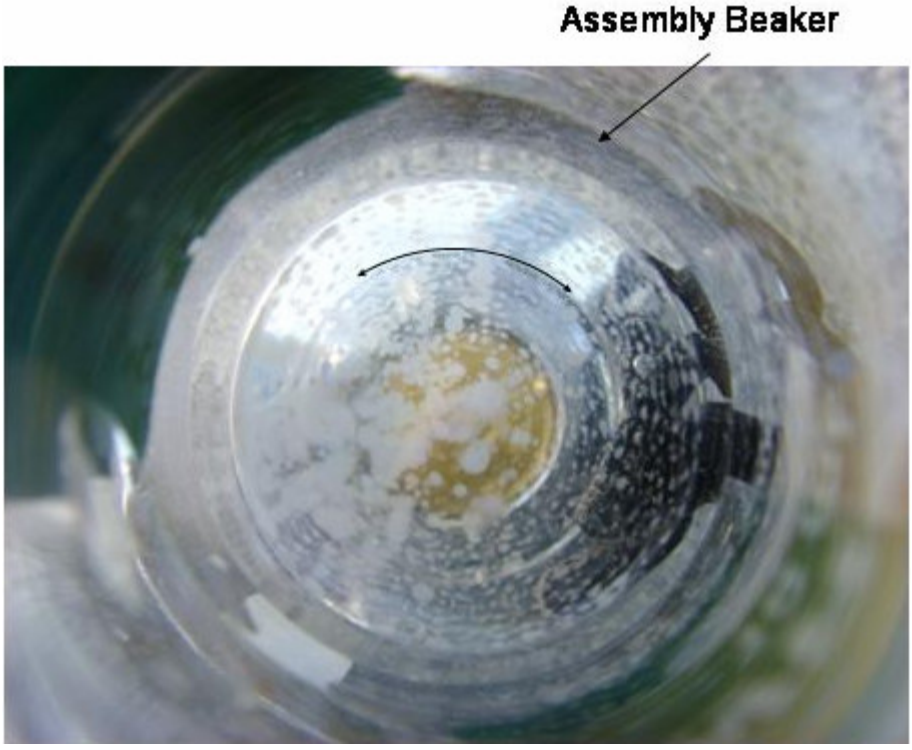

Figure 6. 10 Top view of an aggregation pattern of microspheres at the bottom surface of the assembly beaker during ultrasound excitation. A curved arrow is drawn to highlight the concentric pattern of the aggregation at the peripheral region of the bottom surface. The pitch between the rings is 0.8 mm. The image of the yellow circular part transmitted through the beaker glass indicates the vibration pad emanating the ultrasound wave into the beaker. The input voltage was set to 55 volts.

the lifting flows at higher input powers enable the lift-off of microspheres, and, therefore, provide full circulation.

During the in-plane motion on the surface, assembly occurs when the microspheres encounter the holes. There are two possible impedance forces that act against the in-plane motion of the microspheres. One acts on the flat surface and the other acts at the edges of the holes.

1) Those impedance forces can be addressed as follows. Spatial variation of the roughness on the flat surface leads to a minimal change of contact area, which in turn generates retention force. This minimal retention force on the surface then may impede the in-plane circulation of microspheres on the surface before they reach the holes.

2) The surface curvature change from a flat surface to a convex surface at the opening edge of a hole introduces a high contact area reduction rate, thereby providing a local energy barrier to the microspheres about to step over the edge and enter the hole as shown in Figure 6. 11. The local convex surface is necessarily present to connect a flat surface to a concave surface (inside a hemispherical hole).

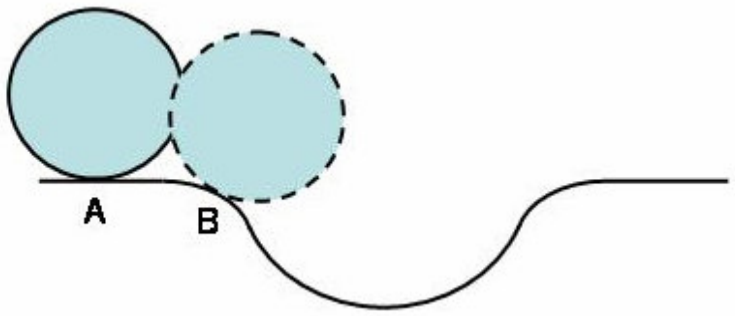

Figure 6. 11 Local energy barrier at the opening edge. The contact area at B on a convex surface (locally present at the opening edge) is smaller that the contact area at A on a flat surface, resulting in a local impedance force to the assembly motion.

These impedance forces can be in competition with the drag exerted by the acoustic on the microspheres, and as a result, they may affect the assembly. An exact quantitative assessment of these impedance forces would be non-trivial, but the impedance force and drags may be roughly characterized in order to qualitatively understand how the competition between them varies with different size scales. First, the impedance force is characterized as follows. For both cases presented above, the impedance forces come from surface adhesion and are proportional to the contact area (or its rate of change), which is in turn linearly proportional to the radius when the radius is much greater than the characteristic length, d_c. Therefore, *the impedance forces vary linearly with the radius,* R_s. The impedances forces are opposed by acoustic streaming drag on the microspheres. The acoustic streaming circulation drag may be estimated as given by eq. (5.13). However, the drag will depend not only on the radius of the microspheres, but also on the velocity profile

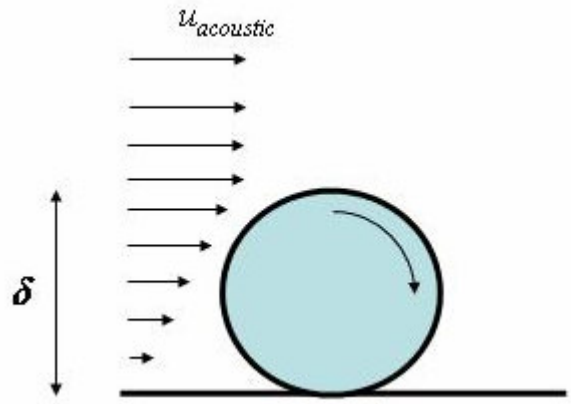

Figure 6. 12 Velocity profile of acoustic streaming flow and the boundary layer thickness, δ_p.

associated with height from the surface inside the boundary layer. The velocity profile of the acoustic streaming is shown in Figure 6. 12. It is zero at the surface based on the non-slip condition and grows with separation from the surface. Based on a linear velocity profile as shown in Figure 6. 12, acoustic streaming drag on the microspheres can be given by

$$F_{acoustic} \sim 6\pi\mu R_s\left(\frac{R_s}{\delta}u_{acoustic}\right) = \frac{6\pi\mu u_{acoustic}}{\delta}R_s^{\,2}. \tag{6.1}$$

Therefore, the ratio of the impedance force $F_{impedance}$ to the acoustic streaming force $F_{acoustic}$ is given by

$$\frac{F_{impedance}}{F_{acoustic}} \sim \frac{Constant}{R_s}. \tag{6.2}$$

The ratio given by eq. (6.2) indicates that the impedance forces become more dominant as the size (radius) decreases, so that the circulation of the components becomes

less effective. In the experimental observations of 0.432 μm diameter microspheres, the dependence of circulation on size is manifested. First, the maximum yield rate was only 85 %, as compared with 100% for the experiments with the 1.6 μm and 0.88 μm diameter microspheres. Second, achieving even this yield rate required 95 V supplied to the transducer (as compared with 85 V for the larger microspheres), because no assembly was observed for 85 V and its weaker circulation. These observations clearly indicate that the circulation provided by the ultrasonic transducer becomes insufficient at small sizes, either reducing the assembly rate, or increasing the power needed to ensure that the circulation is effective. The statistical and quantitative assessment of the contribution of in-plane circulation to the assembly is not considered here because of the considerable complexity of the mechanism.

In order to verify the presence of the boundary layer streaming, an immersed lens was adopted as shown in Figure 6. 13. For these real-time assembly observations, the assembly beaker was left uncapped, allowing the lens to be placed inside the beaker. Because the experiment was conducted with the top of the beaker open, the assembly beaker was filled with ethanol, which it is less volatile and less toxic than acetone. Only the central part of the beaker bottom was visible because the placement of the lens inside the beaker is restricted by the beaker and lens geometries. The typical assembly template

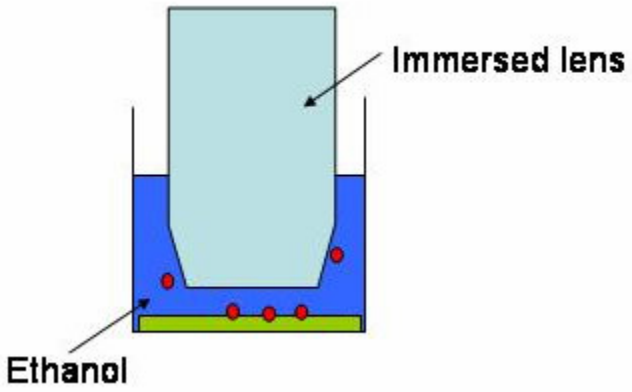

Figure 6. 13 Real time observation set-up

chips are small and rest at the edge of the assembly beaker, but chips at the beaker's edge can not be viewed by the immersed lens. To ensure that the assembly region would be visible, the template for this experiment was made 21mm x 21 mm so that it covered most of the bottom of the beaker. In this large template, the arrays of holes were patterned at the center of the chip. The microscope image as shown in Figure 6. 14 was captured and recorded by a camera, which was connected to the microscope. The streaks visible in the left region of the image indicate microsphere circulation by boundary layer streaming. This image certainly proves the presence of boundary layer streaming on the surface; however it should be noted that the component circulation might be different at the periphery of the beaker where the templates for the original assembly experiments were placed.

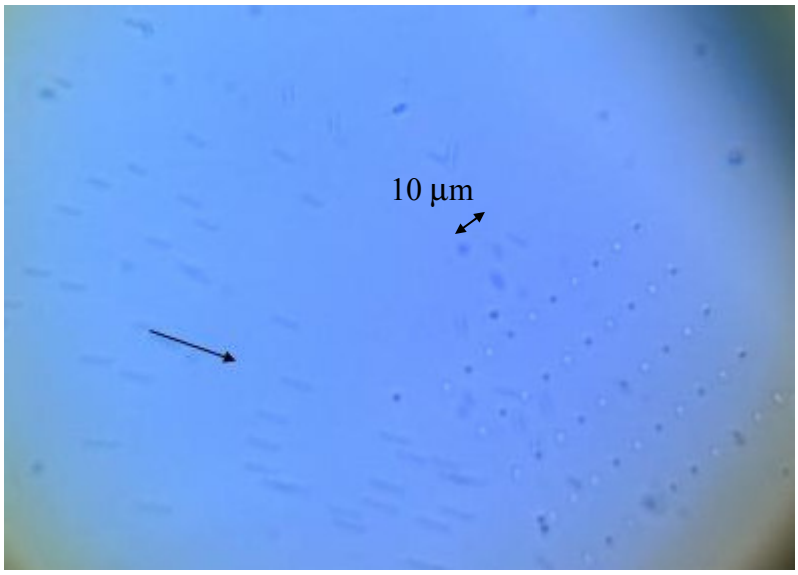

Figure 6. 14 Micrograph of in-plane circulation of microspheres caused by acoustic streaming flow. Circulations appear as streaks in the images. Circulation direction is indicated by the arrow. A pattern of holes is also shown at the bottom left of the image.

6.3.5 Model verification

The theory states that the competition between retention torque and removal torque determines the yield rate and the assembly selectivity. Figure 6. 15 demonstrates the correlation between yield rate and the ratio of removal torque/retention torque. It was found that among the other indicators of this competition, such as the difference between retention and removal torque, the ratio of the retention torque to the resultant removal torque is the most adequately correlated with yield rate. The major benefit of using the ratio value compared to using the net value is that it allows all the yield data on the three different scales to be presented on the same plot. Retention torque was computed based on the rate of change of the contact area as described in Chapters 4 and 5. Removal

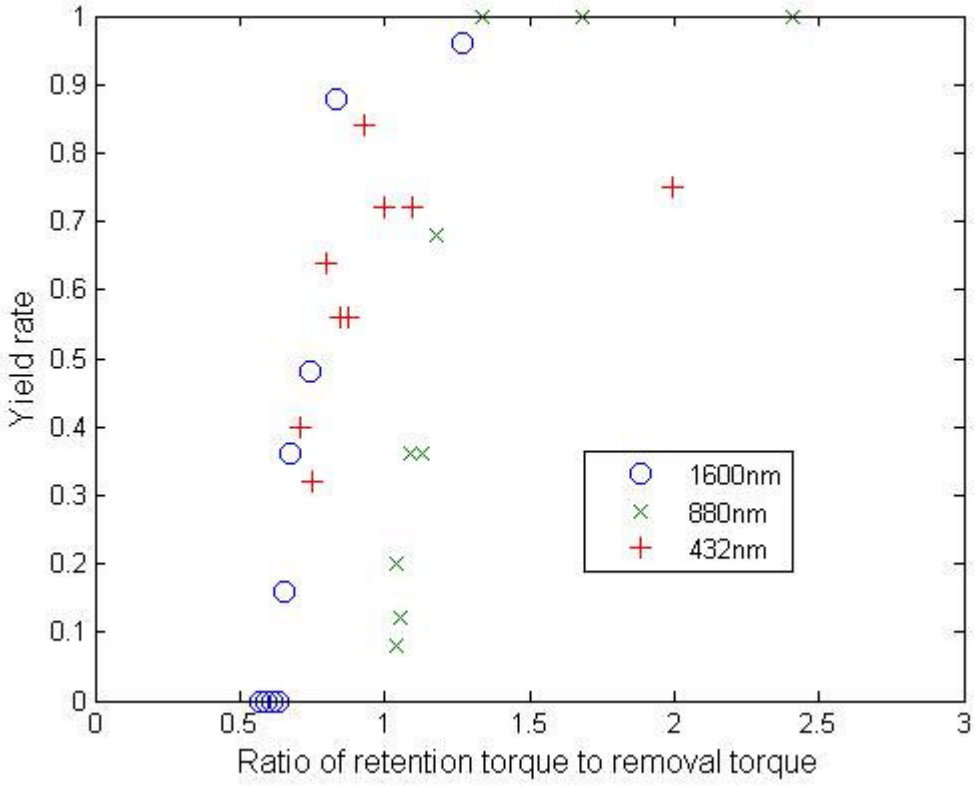

Figure 6. 15 Yield rate versus ratio of retention torque to removal torque for the assemblies of microspheres with diameters of 1600nm, 880nm, and 432nm

torque was calculated based on the roll-off removal mechanism using the resultant torque as described in Chapter 5. Also, the uncertainty of the values of the ratios of retention torque to removal torque was calculated based on the uncertainties of the interfacial energy, the characteristic length of hydrophobic force, and the efficiency of the transducer as described in Section 5.1. When the yield rates for the three different size spheres are plotted versus this ratio on the same plot, the results converge onto a single curve, to within the certainty quoted above. The ratios at which the yield rates changes from 0 to 100% encompass one,

which is consistent with the selective removal theory presented earlier. The role of circulation will also be significant for smaller sizes, but that effect was not fully integrated into the comparison with the theory presented here. The assembly of large microspheres does not seem to be affected by circulation as much.

6.4 Assembly with ultrasonic power variation

The purpose of this experiment is to investigate and show sensitivity of the assembly rate to ultrasonic power. The size of microspheres used for this study is 880nm. Except ultrasonic power variation, all other experimental and layout details are set as explained for 6.1.2. Assembly results with different input voltages (50 V, 55 V, 70V, and 85V) are illustrated in Figure 6. 16. The intensities (power values) of the ultrasound at the surfaces of the templates, corresponding to the given voltages, were calculated as presented in Appendix C, and here the intensity is assumed to be proportional to the voltage squared. In Figure 6. 16, the number on the x- axis represents the number of hole type as presented in Figure 6. 1, which increases with the size of the exposed area in the PMMA; higher numbers represents the larger exposure spots. With higher power, the yield rate is reduced, which can be expected based on the proposed model in which higher power enhances removal torque. Along with the variable contact area data and the variable microsphere

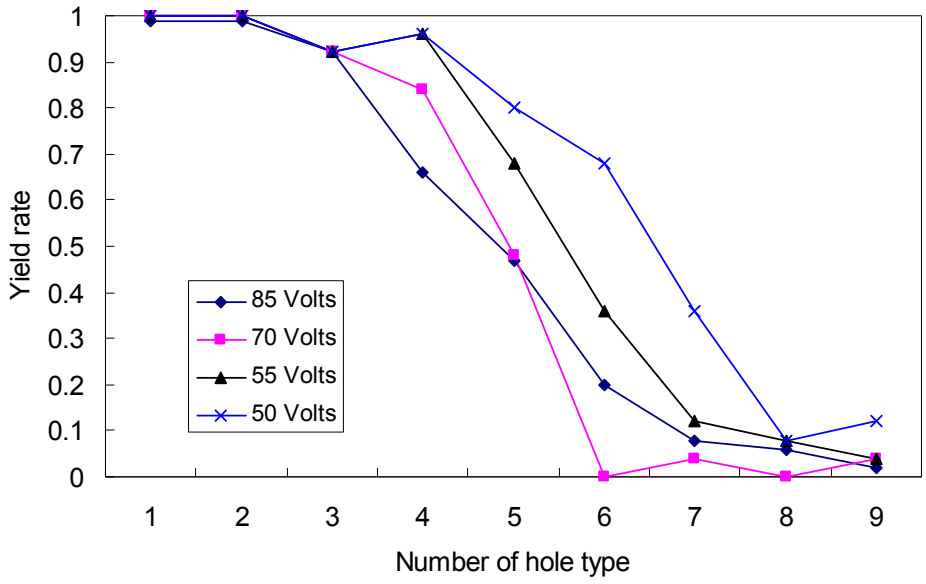

Figure 6. 16 Yield rate versus number of hole type with various voltages driving the ultrasonic transducer (and hence with various powers).

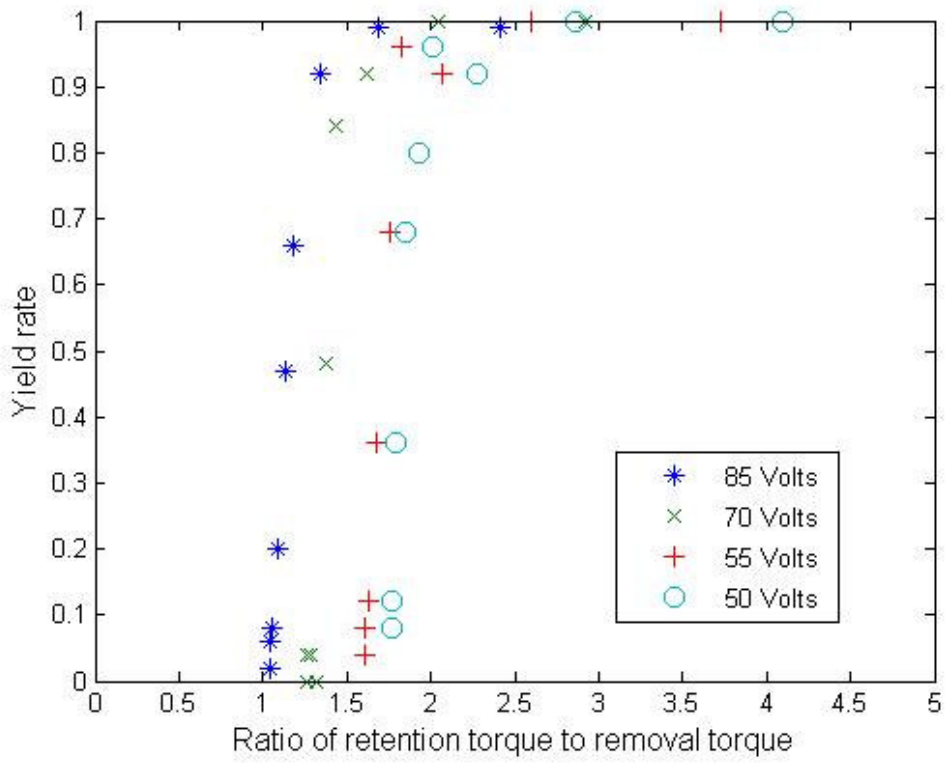

Figure 6. 17 Yield rate versus ratio of retention torque to removal torque with various voltages driving the ultrasonic transducer (and hence with various powers).

size data presented above, these results can be used to verify the theory. The ratio of retention torque to removal torque was calculated for each set of experimental conditions. The yield rates are also plotted versus the ratio of retention torque to removal torque as shown in Figure 6. 17; the error bars of the presented ratios have the same ranges as shown in Figure 5. 7. Figure 6. 17 also manifestly demonstrates the role of component circulation in the assembly decoupled from the removal theory. This observation is based on the fact that the yield rates are found to be higher with higher input voltages at the same ratio of retention torque to removal torque. Conclusively, it can be argued that more circulation is induced with higher power, increasing the chance of assembly and, therefore, increasing the yield rates. The integration of component circulation into the theory remains to be accomplished in future study.

6.5 Assembly with microspheres greater than holes

The experiments described so far have demonstrated that microspheres will assemble selectively into holes that are well-matched to their size rather than into holes that exceed their size. To demonstrate complete assembly selectively, the case in which components are larger than some of the holes was examined by conducting additional assembly experiments. In the previous assembly examples, the microspheres are smaller than holes

in width because of the flat hole bottoms resulting from the finite exposed spot sizes of the lithography patterns. To examine the selective removal of oversized microspheres from smaller holes, first experiments were conducted and then retention torques were computed and compared with removal torques.

Two experiments were separately conducted. The first experiment used microspheres of 1.6 μm with the same template as used in Section 6.3.3 (for 0.432 μm spheres), and the second experiment used microspheres of 1.6 μm with the template used in 6.3.2 (for 0.88 μm spheres). The rest of details of the assembly experimental set-up are described in Section 6.1.2. First, when the 1.6 μm microspheres were introduced to the template that matches 0.432 μm diameter spheres, no holes were filled (Figure 6. 18), as expected from theory. However, when the 1.6 μm microspheres were introduced to the template that matches 0.88 μm diameter spheres, the hole are found to be partially filled with the microspheres. This was unexpected, and a further analysis was carried out in order to determine whether this was as predicted by the theory. The peak of the yield rate is located at the type 3 holes in Figure 6. 19. The depth of these holes is 0.42 μm, which is smaller than the 0.8 μm radius of the microspheres. However, the opening width of the holes varies from 1.2 μm to 1.7 μm, depending on the size of the exposure spots. Due to the variation in the opening widths of the holes, configurations of a microsphere in contact

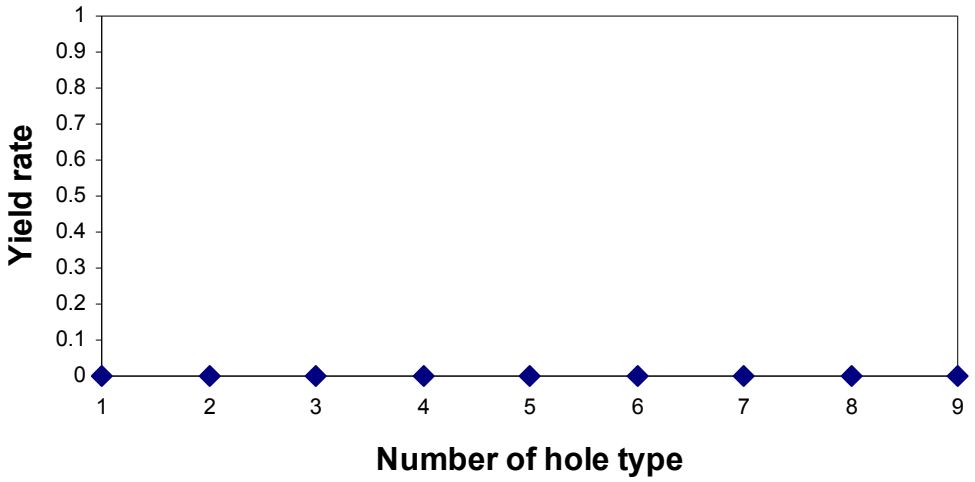

Figure 6. 18 Yield rate versus number of hole type for the assembly of microspheres of 1.6 μm into the template of the holes commensurate to a microsphere of 0.432 μm.

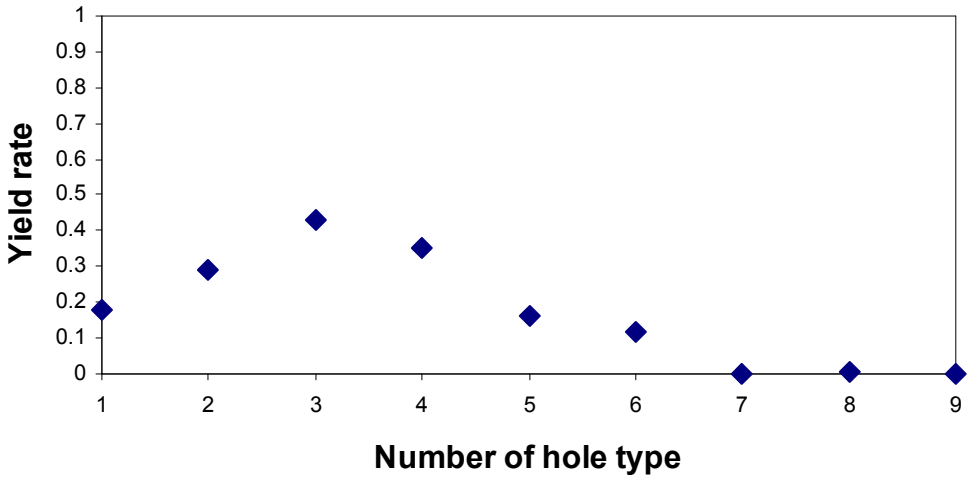

Figure 6. 19 Yield rate versus number of hole type for the assembly of microspheres of 1.6 μm with the template of the holes commensurate to a microsphere of 0.88 μm.

with the holes also vary. Figure 6. 20 schematically demonstrates the matching qualities of a microsphere in contact with holes with different opening widths and the same depth.

In Figure 6. 20 a microsphere can sometimes contact a hole of median size not just at the rim, but also on the bottom, which introduces higher retention torques, and therefore is more favorable to assembly than the other two. The geometric criterion for a microsphere to contact a hole in this way is illustrated in Figure 6. 21. Using the equation in Figure 6. 21, the opening width of a hole (depth =0.44 μm), where a microsphere of 1.6 μm can be fixed-in, is estimated at 1.4 μm. Among the hole types, it was found that the holes of type 3 and type 4 most closely match those dimensions, which therefore explains the anomalous peak of the yield rates in the holes of type 3 and type 4. The proposed theory was also applied to the assembly data by calculating retention torques. For the torque computation, it is assumed that the pivotal point of the rolling is fixed during the rolling because the rolling point is at the edge, which is geometrically a vertex (or highly convex) as shown in Figure 6. 22. Using this assumption, the retention torque is computed in the same manner as described in Chapter 5, based on the rate of change of contact area with respect to the rotational angle; however, it should be noted that the equations of (5.4) and (5.5) should not be used here because the term of $\frac{dA}{ds}$ is undefined at the vertex contact point. Figure 6. 23 shows that the plot of yield rate versus the ratio of retention torque to removal torque agrees moderately with the model. Further, the verified validity of the proposed model in this case allows the mismatched assembly of larger microspheres into smaller holes to be

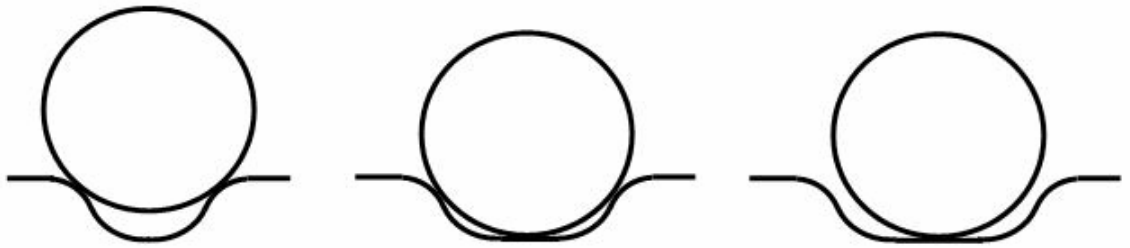

Figure 6. 20 Schematic of a microsphere in contact with a hole with depth smaller than the radius of the microsphere. (a) A microsphere with a hole of small exposure spot (lower hole type number). (b) A microsphere with a hole of medium-sized exposure spot (median hole type number). (c) A microsphere with a hole of large exposure spot (higher hole type number).

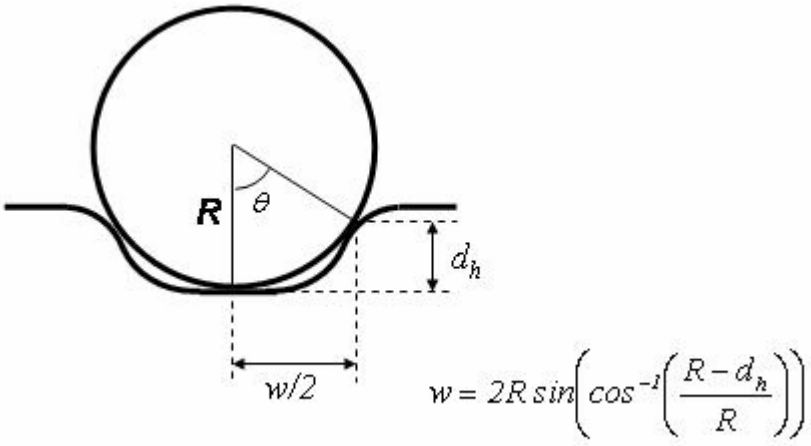

Figure 6. 21 Geometric relation between the radius of a microsphere, *R*, and the depth of a hole, d_h, and the opening width of a hole, *w* when the a microsphere is best fit into a hole with the depth smaller than the radius of microsphere.

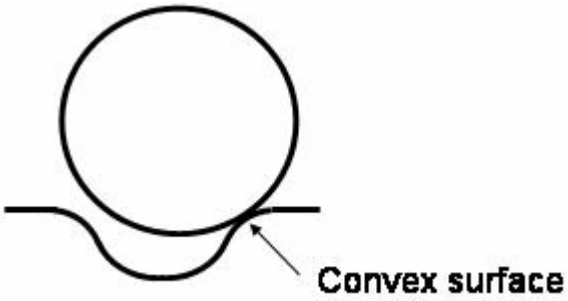

Figure 6. 22 A microsphere tips over the convex surface at the opening edge of a hole.

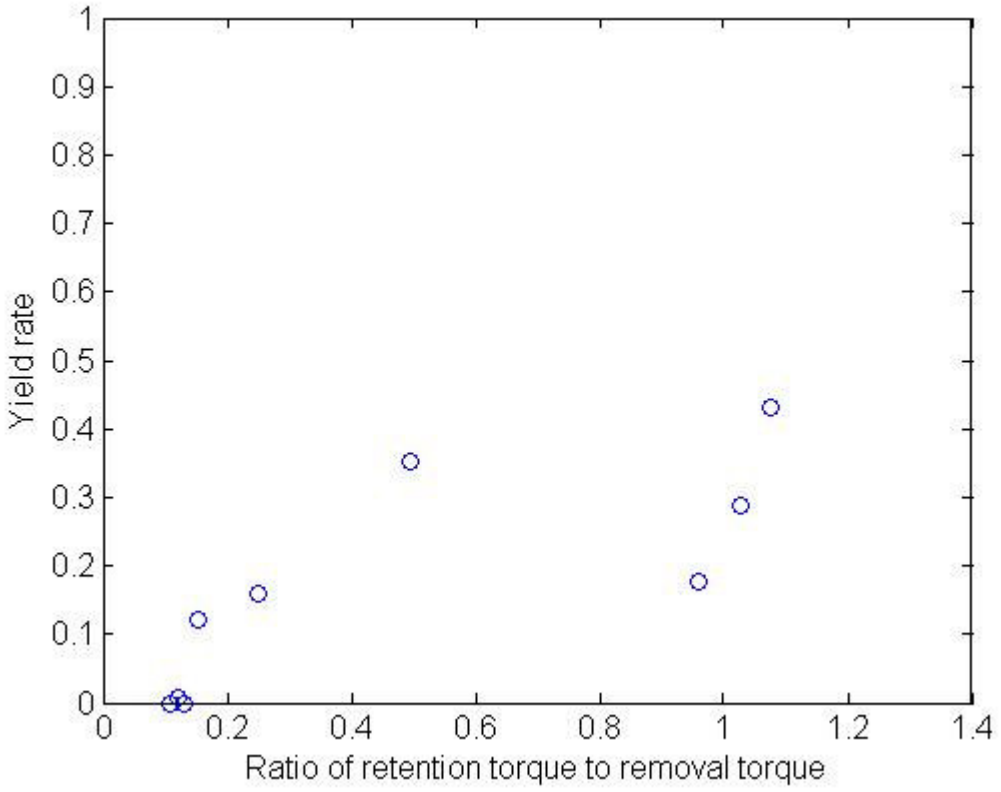

Figure 6. 23 Yield rate versus ratio of retention torque to removal torque for the assembly of microspheres of 1.6 μm with the template of the holes commensurate to microspheres of 0.88 μm.

predicted and avoided by careful template design.

6.6 Summary

In this section, various topics to expand the applicability of the present assembly approach were addressed and examined with relevant experimental results. The experiments with different sizes of microspheres successfully show the size selectivity of the present approach at size scales as small as 216 nm radius; physical size limitations of the assembly will be discussed in Chapter 7 in the context of thermal energy. Circulation

of microspheres by acoustic streaming was observed, and its size-dependent role in the assembly was described. Size selective assembly was demonstrated for the case when the microspheres are smaller than the holes as well as for the case when the microspheres are larger than the holes. Anomalous assembly was found in the case where the microsphere is greater than the hole for certain sphere-hole geometries. However, the theory can predict the anomaly, so it can be avoided by careful preparation. After repeating experiments based on the same set-up, it was found that the variation ranges from 0% to 40%, with the largest variations being observed near 50% yield and the smallest variations being observed at 0% and 100%. Also, as expected, the assembly results are affected by power variation. However, these power variation experiments also demonstrate some degree of discrepancy between the yield versus retention/removal torque ratio curves. This observation indicates that the component circulation can significantly affect the assembly in some cases and therefore needs to be fully integrated to improve the accuracy of the theory.

7 Conclusions and Future Work

7.1 Summary

Selective self-assembly of microspheres into a three-dimensionally shape-matched template has been demonstrated and quantified. The assembly is guided by a combination of a shape-matched template, attraction between functionalized components, and a high frequency ultrasonic excitation that provides controllable removal forces/torques. Firstly, two mechanisms for the selective assembly and removal process were proposed and examined (lift-off and roll-off). Based on the proof-of-concept experiment, the forces and torques that contribute to removal from and retention in a given site have been calculated. The calculation shows that the observed selectivity is consistent with a roll-off mechanism driven by ultrasonic forces, mostly by the Basset force in the size range considered here (from 0.432 μm to 1.6 μm).

Additional topics that enable the present approach to be widely used were addressed and experimentally studied. Scalability of the assembly was examined by conducting three separate experiments with each of these different sized microspheres and their commensurate templates. Excellent selectivity was observed with 0.8 μm and 0.44 μm radius microspheres, and good selectivity was observed with 0.216 μm microspheres. The

role of circulation in the assembly was also identified, and it was particularly prominent in the assembly of the smallest microspheres. The scaling of circulation was outlined, but detailed quantification of its contribution to the assembly process was not considered here. The present assembly set-up was found to be relatively repeatable, with yield rate variation between 0% and 40%. Yield rates near 0% and 100% were more repeatable while intermediate yield rates were less repeatable. Assembly experiments with power variation demonstrate that with larger removal torques, less assembly yield rate is achieved as expected. Also, they demonstrate component circulation effects on the assembly yield. The case where the microspheres are greater than target holes was studied, and the assembly results of this case were in good agreement with the model predictions (near zero yield for a poor sphere-hole match). All the results of these additional experiments are consistent with the selective removal model, which indicates that the model can offer a predictive tool to control the assembly for further works.

7.2 Conclusions

This study presents an assembly technique with excellent selectivity at the intermediate scale where capabilities (including selectivity) of many pre-existing techniques are often limited due to lack of knowledge and lack of controllability. The

excellent selectivity of the present approach potentially allows highly selective incorporation of different types (sizes and shapes) of components into a single system, thereby providing an extensive variety of architectures for microelectronic or sensor systems. Additionally, even in the presence of various uncertainties (including roughness estimation, power intensity estimation, range of hydrophobic force characteristic length, and so on), the proposed theoretical model successfully predicts the selectivity at different scales and therefore ensures that the present approach can be adopted at various scales without engaging excessive preliminary experiments and costs. Also, in the model, the fluidic forces induced by the ultrasound are thoroughly identified so that the removal forces at different size scales can be more precisely controlled by easily tuning the properties of the ultrasound. In future, the present assembly can be more widely and practically used under the guidance of the theoretical model even though many challenges remain in the present approach as discussed in the following section.

7.3 Challenges and future works

This present assembly technology offers several promising features as a manufacturing tool at the intermediate size scale. Along with the effective selective assembly capability, the rapid time-effective assembly operation would also be an outstanding feature of the

approach. However, even with the promising features, challenges of the present approach must still be addressed before the technology will be ready for real manufacturing applications. The limitations and challenges of the present technology are briefly addressed and possible solutions are provided.

7.2.1. Physical size limit of the assembly

There is a lower limit of component size below which this assembly approach will not be effective. In this section, these size limits are addressed in association with thermal energy. Thermal energy is more prominent at very small scales. At the size scale where the molecular energy is comparable to the surface energy, a component can move into or out of a hole simply by thermal energy, even in the absence of external excitation. This statistical, random motion by thermal energy will undermine the assembly selectivity, which is based on the competition between surface adhesion and fluidic forces. The lower limit on size for the present assembly approach can be estimated by setting the two energies equal.

$$C\gamma R^2 \sim kT \qquad R \sim \sqrt{\frac{kT}{C\gamma}} = \sqrt{\frac{(1.38\times10^{-23} J/K)(300K)}{(0.001)(5\times10^{-3} J/m^2)}} \approx 30nm \tag{7.1}$$

This indicates that the selectivity of the present assembly is significantly affected by

thermal energy at the scale of 30 nm or less.

7.2.2 Assembly of anisotropic components

One challenge with this approach is to assemble anisotropic components into templates at small scales. For assembly of anisotropic components such as cylinders and cubes into templates, the orientation of the components needs to be controlled as well as the position. Boundary layer acoustic streaming may offer a tool for controlling orientation based on the deterministic direction of the mean flows. With careful design of the assembly system, the flows could be induced to be able to orient the component into patterns on the surface of template.[34] The successful demonstration of assembly with anisotropic components would significantly improve the variety of architectures that could be made, thus accommodating the needs of real, complex, functional devices. In the future, shaped templates may be replicated by rapid techniques such as nanoimprinting[35] and then used to create fully functional, selectively assembled nanosystems.

7.2.3 Spatial uniformity of assembly

Achieving uniform assembly over a large area will be challenging. As indicated by the ring bands of component aggregation in the experiments (Figure 6. 10), the mean flow

fields are not uniformly present in the present assembly system. Different incidence angles of the ultrasonic wave may resolve the flow localization. For example, if the traveling direction of the wave is set parallel to the surface, it may induce a uniform flow field. However, a parallel wave would not drive the removal mechanism described here, which is driven only by the vertical wave and is based on vertical forces. Clearly, vertical forces would not be provided by the parallel wave. Therefore, any wave traveling off the vertical axis provides a relatively weak vertical force and does not fully drive the removal mechanism; on the other hand it could achieve spatial uniformity. Another option for the wave to keep the vertical direction while improving the uniformity of the field is to move the focused area of the ultrasonic source over a period of time. The progressive motion averages out the spatially uneven intensity, thereby reducing the aggregation of microspheres at a few specific stable spots. The time scale of this movement needs to be carefully controlled, taking into account the boundary layer acoustic streaming velocity and the separation distance between the bands. Also, the surface of the templates can be set to face the ultrasonic source to minimize the number of interfaces between them, thereby minimizing power loss.

7.2.4 Soft assembly components

The assembly of soft components would not be expected to differ much from that of rigid components, even though the former generally introduces more contact area (Figure 7. 1). A soft component in contact with a template would create additional contact area associated with elastic deformation, which is more pronounced with elastically soft materials. However, the free energy of the soft component in contact does not change upon elastic deformation, even with the additional change in contact area, because elastic deformation is thermodynamically a reversible process[36-38]. As a result, no additional free energy change is introduced overall and free energy change is introduced only with the hole-microsphere shape matching as described in the present study which, therefore, allows the present theory to still be extended to the assembly of soft components.

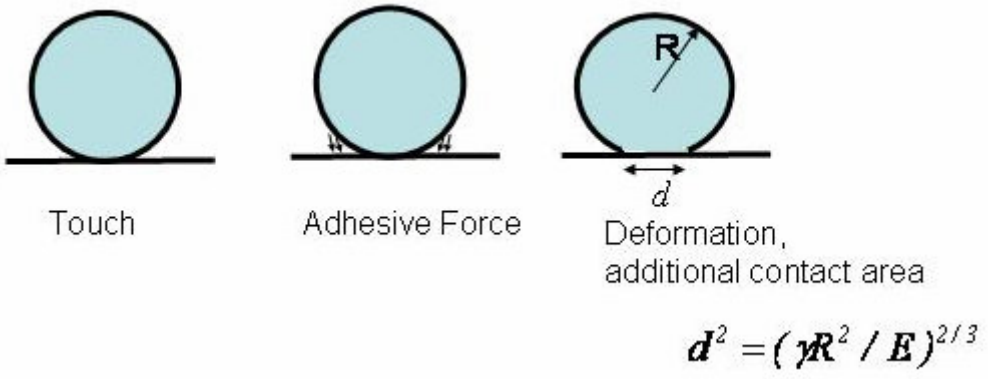

Figure 7. 1 Soft sphere deformation by adhesive force and the contact area calculation.

When the TASR approach achieves selective assembly of anisotropic components into templates along with uniform quality over extended areas, it will greatly upgrade diversity of architecture for microsystems from what is possible with spheres. It will be also ready for nanomanufacturing, where extended uniformity is highly critical. However, the assembly with anisotropic shapes, and extended uniformity are highly challenging and, therefore, additional extensive studies in ultrasonic fields still remain to be conducted for the present approach to be fully ready for practical applications

8 Bibliography

1. Aizenberg, J., Braun, P. V. & Wiltzius, P. Patterned colloidal deposition controlled by electrostatic and capillary forces. *Physical Review Letters* **84**, 2997-3000 (2000).
2. Chen, K. M., Jiang, X. P., Kimerling, L. C. & Hammond, P. T. Selective self-organization of colloids on patterned polyelectrolyte templates. *Langmuir* **16**, 7825-7834 (2000).
3. Clark, T. D., Ferrigno, R., Tien, J., Paul, K. E. & Whitesides, G. M. Template-directed self-assembly of 10-mu m-sized hexagonal plates. *Journal Of The American Chemical Society* **124**, 5419-5426 (2002).
4. Cui, Y. et al. Integration of colloidal nanocrystals into lithographically patterned devices. *Nano Letters* **4**, 1093-1098 (2004).
5. Mizuta, H. et al. Nanoscale Coulomb blockade memory and logic devices. *Nanotechnology* **12**, 155-159 (2001).
6. Murray, C. B., Kagan, C. R. & Bawendi, M. G. Self-Organization Of Cdse Nanocrystallites Into 3-Dimensional Quantum-Dot Superlattices. *Science* **270**, 1335-1338 (1995).
7. Srinivasan, U., Liepmann, D. & Howe, R. T. Microstructure to substrate self-assembly using capillary forces. *Journal Of Microelectromechanical Systems* **10**, 17-24 (2001).
8. Tans, S. J. et al. Individual single-wall carbon nanotubes as quantum wires. *Nature* **386**, 474-477 (1997).
9. Tien, J., Terfort, A. & Whitesides, G. M. Microfabrication through electrostatic self-assembly. *Langmuir* **13**, 5349-5355 (1997).
10. Tu, J. K., Talghader, J. J., Hadley, M. A. & Smith, J. S. Fluidic Self-Assembly Of Ingaas Vertical-Cavity Surface-Emitting Lasers Onto Silicon. *Electronics Letters* **31**, 1448-1449 (1995).
11. Wang, X. D., Grauganrd, E., King, J. S., Wang, Z. L. & Summers, C. J. Large-Scale Fabrication of Ordered Nanobowl Arrays. *Nano Letters* **4**, 2223-2226 (2004).
12. Xia, Y. N., Yin, Y. D., Lu, Y. & McLellan, J. Template-assisted self-assembly of spherical colloids into complex and controllable structures. *Advanced Functional Materials* **13**, 907-918 (2003).
13. Yellen, B. R. & Friedman, G. Programmable assembly of heterogeneous colloidal particle arrays. *Advanced Materials* **16**, 111-+ (2004).
14. Deheer, W. A., Chatelain, A. & Ugarte, D. A Carbon Nanotube Field-Emission

Electron Source. *Science* **270**, 1179-1180 (1995).

15. Cheng, J. Y., Ross, C. A., Thomas, E. L., Smith, H. I. & Vancso, G. J. Fabrication of nanostructures with long-range order using block copolymer lithography. *Applied Physics Letters* **81**, 3657-3659 (2002).
16. Israelchvili, J. *Intermolecular & surface forces* (Academic press, 1991).
17. Adamson, A. W. *Physical chemistry of surfaces* (Wiley, New York and London, 1976).
18. Nyborg, W. L. in *Physical acoustics* (ed. Mason, W. P.) 265-331 (Academic press, New York and London, 1965).
19. Dames, C. (Cambridge, 2003).
20. Hogg, R. V., Ledolter, J. *Applied Statistics for Engineers and Physical Scientists* (Macmullan Publishing Company, New York, 1992).
21. Johnson, K. L. *Contact mechanics* (Cambridge university press, Cambridge, UK, 1985).
22. Miki, N. & Spearing, S. M. Effect of nanoscale surface roughness on the bonding energy of direct-bonded silicon wafers. *Journal Of Applied Physics* **94**, 6800-6806 (2003).
23. King, V. L. On the acoustic radiation pressure on spheres. *Proceedings of Royal Society London Series A* **147**, 212 (1934).
24. Lawrence, C. J. & Weinbaum, S. The Unsteady Force On A Body At Low Reynolds-Number - The Axisymmetric Motion Of A Spheroid. *Journal Of Fluid Mechanics* **189**, 463-489 (1988).
25. Olson, L. G. Finite-Element Model For Ultrasonic Cleaning. *Journal Of Sound And Vibration* **126**, 387-405 (1988).
26. Qi, Q. & Brereton, G. J. Mechanisms Of Removal Of Micron-Sized Particles By High-Frequency Ultrasonic-Waves. *Ieee Transactions On Ultrasonics Ferroelectrics And Frequency Control* **42**, 619-629 (1995).
27. Spengler, J. F., Coakley, W. T. & Christensen, K. T. Microstreaming effects on particle concentration in an ultrasonic standing wave. *Aiche Journal* **49**, 2773-2782 (2003).
28. Eckart, C. Vortices and streams caused by sound waves. *Physical review* **73**, 68-76 (1948).
29. Rayleigh, J. W. S. *The Theory of Sound* (New York, 1945).
30. Schlichting, H. *Boudary Layer Theory* (McGraw-Hill, New York, 1955).
31. Jackson, F. J., Nyborg, W. L. Small scale acoustic streaming near a locally excited membrane. *The Jounral of the Acoustical Society of America* **30**, 614-619 (1958).

32. Kolb, J., Nyborg, W. L. Small scale acoustic steraming in liquids. *Journal of the Acoustical Society of America* **28**, 1237-1242 (1956).
33. Spengler, J. & Jekel, M. Ultrasound conditioning of suspensions - studies of streaming influence on particle aggregation on a lab- and pilot-plant scale. *Ultrasonics* **38**, 624-628 (2000).
34. Huang, Y., Duan, X. F., Wei, Q. Q. & Lieber, C. M. Directed assembly of one-dimensional nanostructures into functional networks. *Science* **291**, 630-633 (2001).
35. Chou, S. Y., Krauss, P. R. & Renstrom, P. J. Nanoimprint lithography. *Journal Of Vacuum Science & Technology B* **14**, 4129-4133 (1996).
36. Gui, C., Elwenspoek, M., Tas, N. & Gardeniers, J. G. E. The effect of surface roughness on direct wafer bonding. *Journal Of Applied Physics* **85**, 7448-7454 (1999).
37. Maugis, D. Adhesion Of Spheres - The Jkr-Dmt Transition Using A Dugdale Model. *Journal Of Colloid And Interface Science* **150**, 243-269 (1992).
38. Maugis, D. On the contact and adhesion of rough surfaces. *Journal Of Adhesion Science And Technology* **10**, 161-175 (1996).
39. Mathworks. (2005).
40. Hechet, E. *Optics* (Addison Wesley, 2002).

Appendix A. Method of "nominal" contact area estimation

By definition, integrating all the points of the surface of the microsphere within the distance of 1.5 nm from the surface of a hemispherical hole produces contact area. The presented contact area calculation only involves configurations that have their effective contact points on the sidewalls; the configuration of the microsphere centered at the flat-bottomed area is energetically unfavorable and, therefore, is not considered here. Here, the hole shape is assumed to be axi-symmetric so that the cross section of the hole is able to fully represent the hole shape and minimize the calculation effort. This appendix first presents the characterization of a hole profile with a polynomial and, then, presents the method of contact area calculation based on the hole characterization by the polynomial.

Hole shape characterization

1) Before the calculation, the hole shape is created with a bottom flat surface and a sidewall. The cross sectional profile of the side wall is characterized with a third order polynomial in the form of

$$y = ax^3 + bx^2 + cx + d \qquad \text{(B1)}$$

where x is the distance from the starting point of the sidewall as shown in Figure B. 1 and y

is the corresponding height. The starting point of the sidewall is set to the point whose height is 5 nm from the globally lowest point among the AFM profile data. The value of 5 nm set for the starting point of the sidewall is somewhat arbitrarily chosen, but ensures that it is higher than the maximum height of the roughness (=2.37nm), which, therefore, indicates that the point truly exceeds the range of roughness. With additional conditions, the form of (B1) is further simplified.

For simplifying the polynomial function, the x-y coordinate system is set with the origin at the starting point, A^* as shown in Figure B. 1. Then, subsequently the value of d becomes zero. Also, at the starting point, A^*, the profile of sidewall is assumed to be C1 continuous (curve/surface derivative is continuous) with the bottom flat surface so that $c=0$. As a result, (B1) is simplified to

$$y = ax^3 + bx^2 . \tag{B2}$$

Then, b uses $b = \frac{1}{2*d}$ where d is the depth of the hole as shown in Figure B. 1 (a). The expression $b = \frac{1}{2*d}$ is given by connecting the curvature equation given as

$$\kappa_{x=0} = \left. \frac{\frac{d^2y}{dx^2}}{\left(1+\left(\frac{dy}{dx}\right)^2\right)^{3/2}} \right|_{x=0} = \left. \frac{3ax+2b}{\left(1+(2bx)^2\right)^{3/2}} \right|_{x=0} = 2b \tag{B3}$$

to the isotropic etching condition, $\kappa_{x=0} = \frac{1}{depth}$.

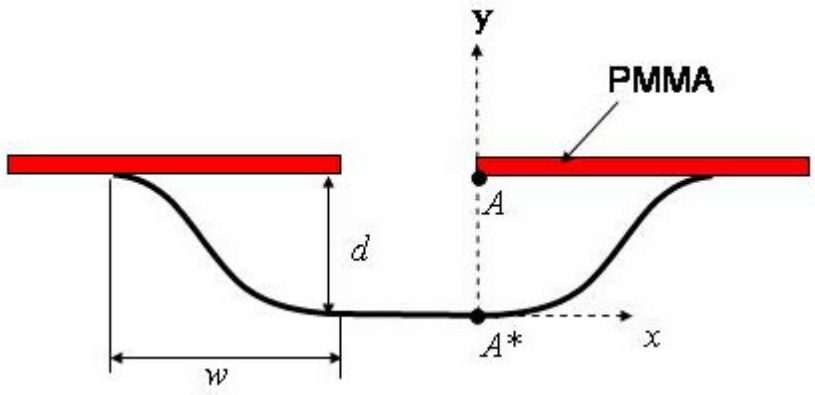

(a)

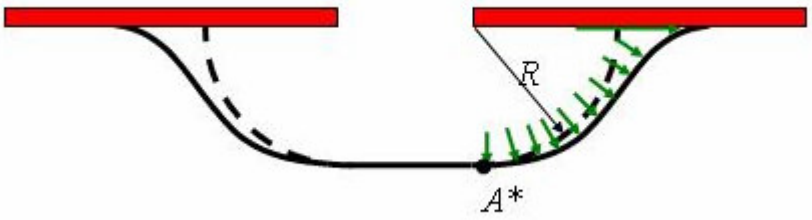

(b)

Figure B. 1 Schematic of cross sectional hole profile and PMMA layer. (a) Coordinate of the third polynomial function of the hole profile. (b) An ideal spherical shape by the isotropic etching (dashed line) is imposed on the hole profile. The velocity field of the etching rates indicated by arrows is also schematically presented with respect to the hole profile.

The estimation for the value of *b* is given based on the isotropic etching characteristic of the oxide, which is however, limited in the present case (the detail of the limitation is given in the following paragraph). Subsequently, with any additional data point of the AFM profile,

a can be determined. Here, the opening edge point is typically chosen for the additional point to determine *a*, which is then given by

$$a = \frac{d - b(w)^2}{(w)^3} \tag{B.4}$$

where *w* is the width of the sidewall from the starting point to the opening edge as shown in Figure B. 1 (a). Therefore, based on detailed understanding of the fabrication process and reasonable mathematical assumptions, the hole shape profile can be easily determined. This third order polynomial characterization of the hole shape allows the profiles of the sidewalls to be easily derived only with the depth and the sidewall width. The following paragraph addresses a limitation of the isotropic etching of bare oxide in association with a PMMA layer, and it also demonstrates how to justify the present polynomial function of the hole shape even in the presence of the limitation.

It is well known that the etching of bare oxide with BOE is isotropic. However, when it comes to the etching of bare oxide underneath a PMMA layer, a different (higher) etching rate at the interface between PMMA and oxide is found, which needs to be carefully considered for the hole profile characterization which is still largely based on the characteristics of isotropic etching. The preferential etching at the interface with the PMMA layer creates a sidewall more widen in the horizontal direction rather than the ideal spherical shape which would be created with an isotropic etch as indicated with the dashed

line in Figure B. 1 (b). Also, as a result of this preferential etching, the local curvature of the sidewall varies. As demonstrated in Figure B. 1, which is based on the observation of the AFM profiles, the topography at *A** (the starting point of the sidewall) is more spherical (locally aligned with the circle of the dashed line) whereas the topographies of the locations with larger distances from the starting point deviate from a spherical shape, with local radii always larger than the local radius at the starting point. This variation comes from the fact that the preferential etching rate at the interface with PMMA has less impact on the regions close to the end of the PMMA layer, *A*, so these regions have isotropic topography. The local radius (reciprocal to the local curvature) at the starting point of the sidewall, *A*,* still largely reflects the isotropic etching an is least affected by the preferential etching at the interface. Therefore, although the isotropic topography can not be fully applied to the sidewall, at the starting point, *A**, the local radius can be still estimated based on the isotropic shape, which leads the depth to be equal to the local radius, thereby allowing $b = \frac{1}{2 * d}$. Figure B. 2 demonstrates how the present hole shape characterization with the third order polynomial represents the real data of a sidewall profile. Here the validity of the present method was investigated in terms of how well the hole characterization captures the curvature of the real hole profile because, as previously stated in Section 5.3, when the contact area is only a very small fraction of a total microsphere surface, which was

observed in all presented cases in this thesis, the relative curvature (or equivalent radius) of

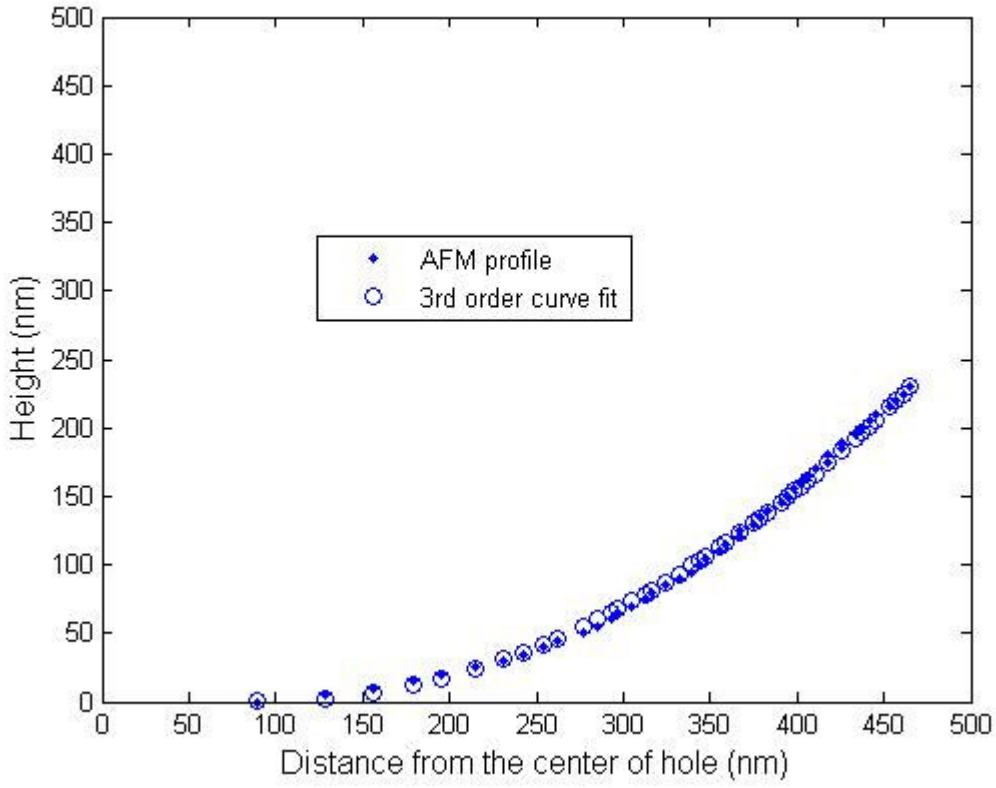

Figure B. 2 AFM measurement and the third order curve fit of a sidewall profile.

two surfaces directly engaged in contact largely determines the contact area. From the real data of Figure B. 2, the estimated curvature deviation of the hole characterization was found to be only 2.5%, which therefore confirms the validity of the third order polynomial characterization and implies that additional higher orders are not necessary.

Contact area computation

Once the holes shape is characterized as above, an ideal sphere is engaged to envision

multiple configurations of a microsphere in contact with a hole. The contact area is calculated with respect to the effective contact point at the starting point of the sidewall as shown and continuously calculated with respect to the successive effective contact points on the sidewall in Figure B. 3; the configuration of a microsphere placed at the center of the flat surface is energetically unfavorable so that this case is excluded from the computation.

Once the effective contact point is given, the contact points of the microsphere with the hole are identified by the definition, which is that if the minimum separation of each point on the surface of the microsphere from the hole surface is less than 1.5 nm, the point is identified as a contact point. Then, the identified contact points of the microsphere are integrated to provide the fractional contact area (roughness is omitted here). However, for the proper adoption of the contact point identification, the examination of the minimum separation of each point of the microsphere needs to be differently conducted for two separate regions, Part A and Part B as shown in Figure B. 4. The division is made based on border line of the flat bottom surface indicated by the dashed line in Figure B. 4.

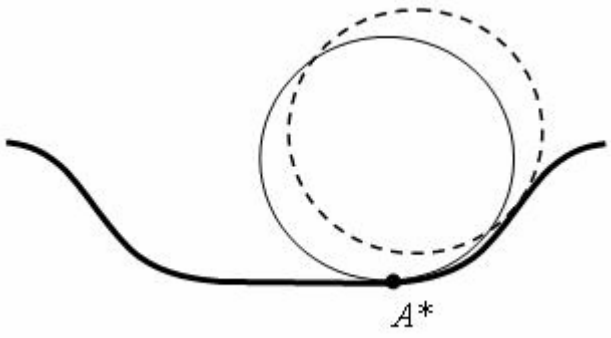

Figure B. 3 Configurations of a microsphere in contact with a hole.

If a point of the microsphere is under Part A, only the vertical separation of the point measured from the bottom flat surface, which equals the minimum separation of the point from the hole surface, is examined (Figure B. 5). If the measured separation is less than 1.5 nm, the point is included as a point in contact. With points vertically aligned with the

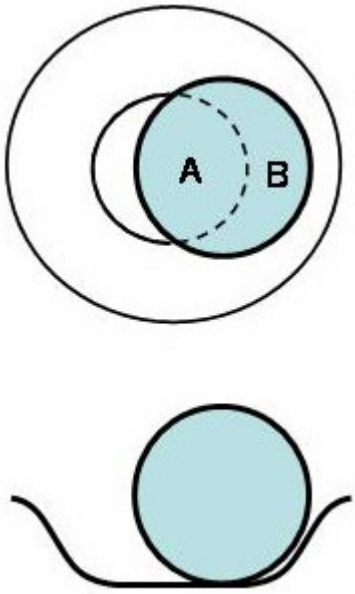

Figure B. 4 Part A and Part B and the border line of the flat bottom surface with top view (top) and side view (bottom) of a microsphere in contact with a hole. Part A and Part B only involves the lower part (the bottom half) of the microsphere.

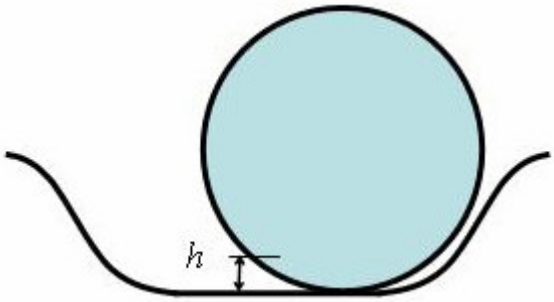

Figure B. 5 Minimum separation (*h*) of a point of Part A from the hole surface.

border line between Part A and Part B, the vertical separation from the flat bottomed surface also serves as the minimum separation from a point of the border line to the hole surface. The local radius of sidewall of the present cases ranges from 220nm to 800 nm, which is much greater than the force characteristic range of 1.5 nm; therefore, theoretically it is impossible for any other estimation of the separation to be smaller than the vertical separation. Figure B. 6 also demonstrates that no other point of the hole surface can introduce a separation from the point aligned with the border line that is smaller than the vertical separation.

The calculation of minimum separations of points of Part B from the hole surface should differently and carefully engage the specific hole profiles as described below. The minimum separation of any point under Part B from the hole surface is examined with an imaginary sphere. The imaginary sphere has the center at the point of Part B with the radius equal to 1.5 nm as shown in Figure B. 7. The characterized cross sectional profile in the form of the third order polynomial is then engaged with the sphere to determine if any point of the cross sectional profile is inside the sphere of the radius of 1.5 nm. Because the hole shape (as well as the imaginary sphere) is axis-symmetric, only the cross sectional profile needs to be introduced in the engagement of the hole surface with the

imaginary sphere. Then, the imaginary sphere is represented by a 2-dimensional circle as

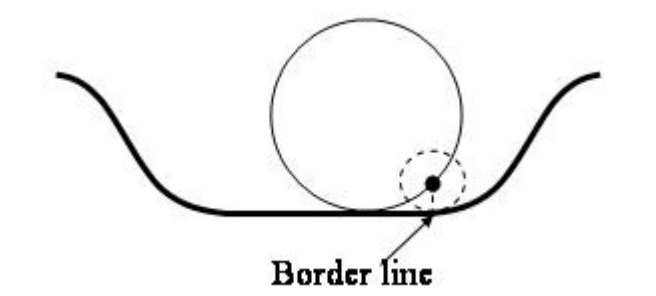

Figure B. 6 Engagement of a point (small circular dot) of a microsphere (aligned with the border line) with the sidewall profile in association with the characteristic range of the hydrophobic force of the point indicated by the circle of the dashed line.

shown in Figure B. 7, and the engagement of the whole surface is limited tothe cross sectional profile, which greatly reduces the computational effort. For the engagement with the sidewall profile, the center of the imaginary circle (reduced from the imaginary sphere) is adjusted with respect to the coordinate system of the cross sectional profile shown in Figure B. 1 (a). Therefore, the expression of the imaginary sphere is given as

$$(x - x_c)^2 + (y - y_c)^2 = 1.5^2 \tag{B5}$$

where the x_c and y_c are coordinate values of a point based on the coordinate system of the cross sectional profile of the sidewall; the imaginary circle is also schematically presented in Figure B. 7. (B2) and (B5) are set to be equalized through the variable of either y or x and, then, the characteristic of the roots to satisfy the equality is inspected. If the roots are found to be all imaginary numbers, then this finding indicates that the

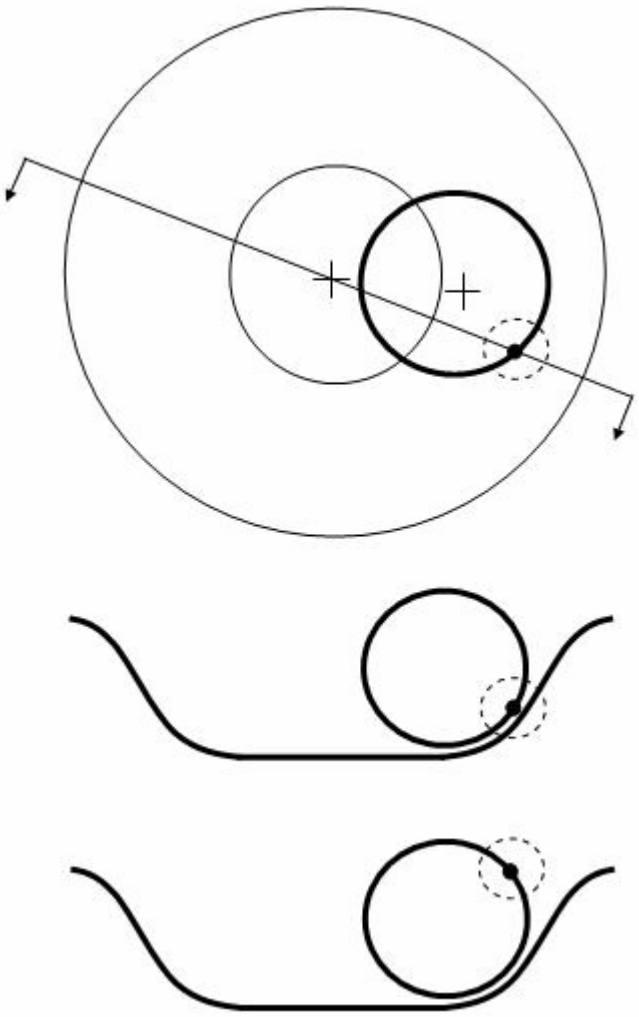

Figure B. 7 The schematics of points of Part B in the engagement with the sidewall. Top view (top) with a line for a cross section and an imaginary sphere of the point set by the characteristic length of the hydrophobic force (=1.5nm). Cross sectional views of points of Part B, one is in contact (middle) and the other is out of contact (bottom). The cross section line does not meet the center of the microsphere, therefore, the cross section does not include the effective contact point.

surface of the hole is completely outside the imaginary sphere, which equally means that the point of the microsphere is separated from the surface of the hole by more than 1.5 nm. Otherwise, i.e. if any of roots is a real number, the point is included as a contact point. The roots are calculated and provided by using predefined subroutines of the MATLAB

software. [39]

The examination of the separation begins with the single effective contact point, which is the point theoretically known to be in contact with the hole. Theoretically, the microsphere and the hole surface is contacted only through single point because the local radius of the hole surface is always greater than the radius of the microsphere; also it should be noted that, because the hole is axis-symmetric, the effective contact point of the microsphere is on the line connecting the center of the hole and the center of the microsphere. Therefore, only one single effective contact exists with the current configuration. From the single effective contact point, the examination of the separation proceeds with discrete points on all the discrete lines of the latitude of the microsphere as shown in Figure B. 8; for discrete numerical computations, the discrete lines of the latitude are set apart by 1/360 degrees ($=\Delta\phi$) and the discrete points on each line of the latitude are set apart by 1/180 degrees ($=\Delta\theta$). The increments can be adjusted in accord with the desired accuracy. The number of points for the examination is adjusted in response to a required accuracy. After all the points of the microsphere in contact with the hole are identified, then the integration of all the contacted points is integrated as

$$A_n = \sum_{j=1}^{360} \sum_{i=1}^{n_j} R_s^2 \, sin(i\Delta\theta)\Delta\phi \qquad \text{(B6)}$$

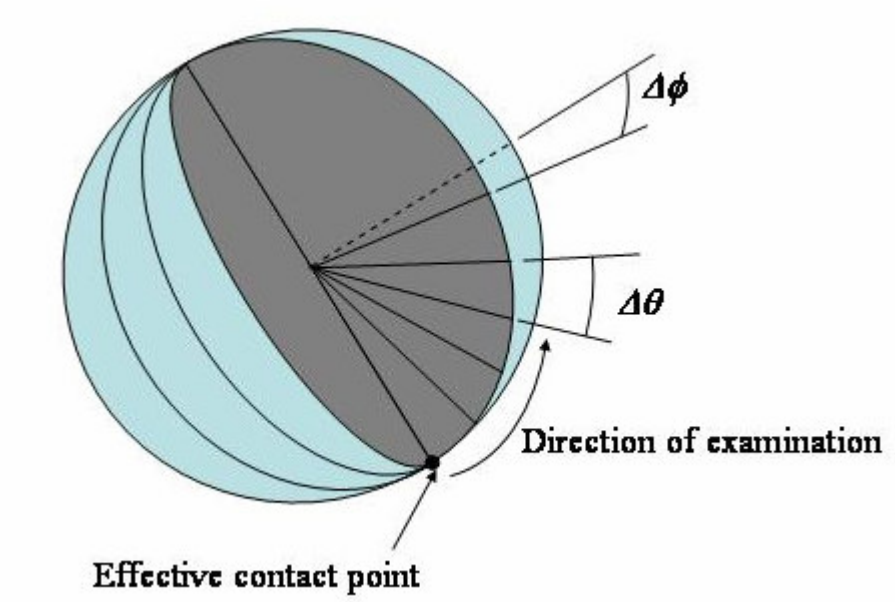

Figure B. 8 Discrete points on a microsphere with respect to the effective contact point and increments of the angles adopted for describing the positions of the discrete points.

where $n_j \Delta\theta$ is the angle of the point, which is the most apart from the effective point on each discrete line set by $\Delta\phi$. Further, the hole shape and the microsphere are both axis-symmetric and, therefore, the contact area is symmetric with respect to the effective point as shown in Figure B. 9, which allows the half side of the microsphere to be considered.

The contact area varies with various locations of the effective contact point on the sidewall, and the variation of the contact area with the template engaged for the assembly of 1.6 μm microspheres is demonstrated in Figure 5. 3. At each effective contact point on the sidewall, the center of the microsphere has to be adjusted corresponding to the location on the sidewall. The center is located on the line normal to the local surface of the effective point, and it is apart from the effective point by the radius as shown in Figure B.

10. The algorithm was coded with MATLAB and the subroutine is appended below.

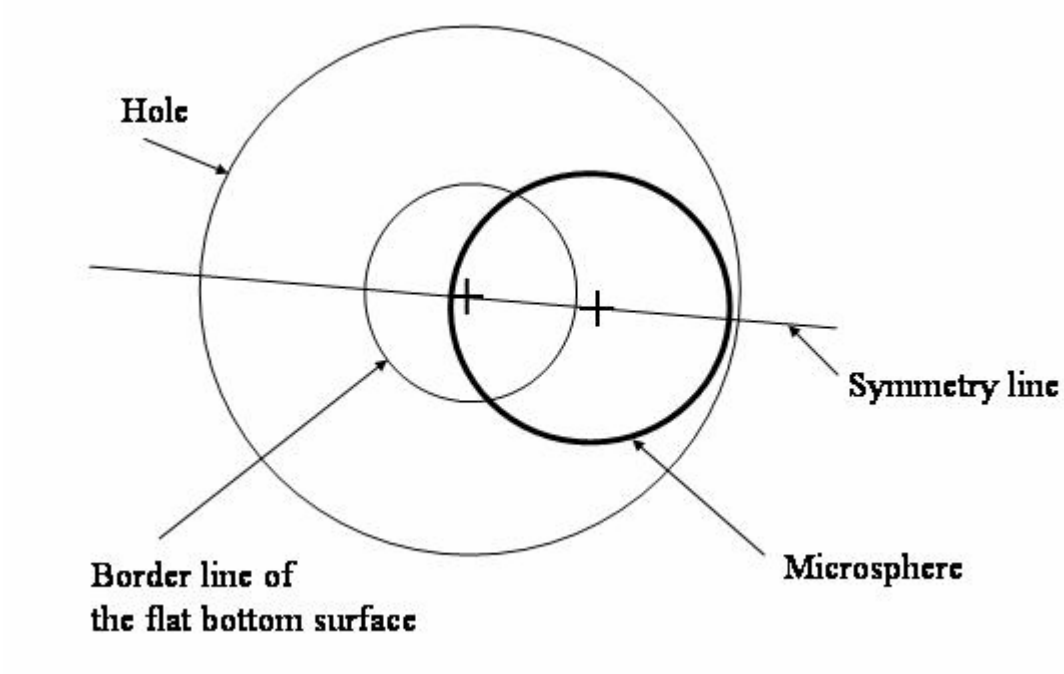

Figure B. 9 Symmetry line of the contact area.

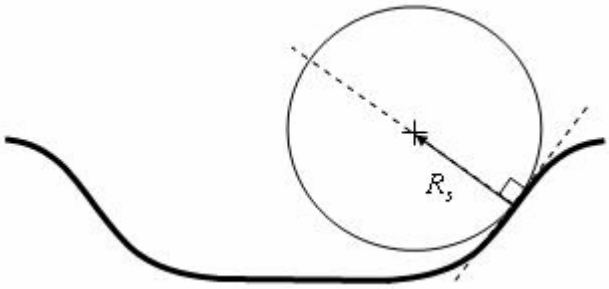

Figure B. 10 The center of the microsphere on the sidewall

Appendix B MATLAB subroutine for contact area calculation

```
%%%%%%%%%%%%%%%%%%%%%%%%%%%%%%%%%%%%%%%%%%%%%%%%%%%%%%%%%%%%%%%%%%%%%%%%%%%%%%%%
sda(1)=1.5;

for kk=1:20

    ditot=1000*(-0.0015*(kk)^2+0.0583*(kk)+2.4676);
    di(kk)=ditot;
    depth=850;
    sidew=1200;
    rb =(ditot-2*sidew)/2;
    rp =800;  % rp: particle size (nm)
    b=1/(2*depth);
    a=(depth-b*sidew^2)/sidew^3;
    c=0;
    sd =sda(1);   % SAM length

    % Contact points along the sidewall
    check=zeros(sidew);
    for iw=1:sidew

        xo=iw-1;
        yo=a*xo^3+b*xo^2;
        fx=3*a*xo^2+2*b*xo;
        thiw=atan(fx);
        xc=rp*cos(pi/2+thiw)+xo+rb;
        yc=rp*sin(pi/2+thiw)+yo;
        ycc(iw)=yc-rp;
        yoo(iw)=yo;
        xiw(iw)=iw;
        itot=360 ;
        jtot=180 ;
        ta=0;
```

```
f=zeros(itot,jtot);

for i=1:itot
    ti= (i)/itot*pi;
    for j=1:jtot
        tj=(j)/jtot*pi/2;
        xi=0;
        yi=-rp;
        zi=0;
        vi=[xi yi zi];
        am=[cos(thiw) -sin(thiw) 0; sin(thiw) cos(thiw) 0; 0 0 1];
        bm=[cos(ti) 0 -sin(ti); 0 1 0; sin(ti) 0 cos(ti)];
        cm=[cos(tj) -sin(tj) 0; sin(tj) cos(tj) 0; 0 0 1];
        dm=am*bm*cm*vi';
        x1=sqrt(dm(1)^2+dm(3)^2);
        x11(i,j)=x1;
        y2=dm(2)+yc;
        x2= sqrt((dm(1)+xc)^2+dm(3)^2)-rb;
        jc(i)=j;
        if x2 >= 0
            c1=a^2;
            c2=2*a*b;
            c3=b^2+2*a*c;
            c4=2*b*c-2*a*y2;
            c5=c^2-2*b*y2+1;
            c6=-2*y2*c-2*x2;
            c7=x2^2+y2^2-sd^2;
            v = [c1 c2 c3 c4 c5 c6 c7];
            p = roots(v);
            nump=6;
            for ii=1:nump
                ff(ii)= any(imag(p(ii)));
                f(i,j) = f(i,j)+ff(ii);
            end
            jc(i)=j;
            if f(i,j) == nump
```

```
                    break;
                end
            else
                f(i,j) = 5;
                if y2 >= sd
                    break
                end
            end
        end

        if (((x2+rb)-xc) >= 0) & (ycc(iw) < sd)
            check(kk,iw)=1;
        end

        daa=0;
        for jj=1:jc(i)
            thj1=(jj-1)/jtot*pi/2;
            thj2=jj/jtot*pi/2;
            da=     rp     *     (pi/2/jtot)*     (pi*rp/itot)     *
((sin(thj1)+sin(thj2))/2);
            daa= daa+da;
        end
        ta = ta + daa;
    end
    rta(kk,iw)=2*ta/(4*pi*rp^2);

end
plot(xiw,rta)
%%%%%%%%%%%%%%%%%%%%%%%%%%%%%%%%%%%%%%%%%%%%%%%%%%%%%%%%%%%%%%%%%%%%%%%%%%%%
```

Appendix C Power intensity estimation

The output power directly from the transducer at the operating voltage of 45 volts was estimated from calorimetry as follows. In the measurement set-up, the transducer was immersed in water contained in a styrofoam cup, and the whole set up was then sealed by another piece of styrofoam to prevent heat loss as shown in Figure A. 1. A thermometer was inserted into the set-up to measure temperature change. Then, the transducer was turned on for 10 minutes and the temperature change was detected by the thermometer. The temperature changes were measured at two different voltages; one is120 volts, where the power into the transducer, P_{120}, is known as 36W in the specs of the transducer, and the other is the operating voltage of 45 volts. Then the power ratio was set equal to the ratio of temperature change between two runs (equally timed) for the same amount of water as given by

$$\frac{P_{45}}{P_{120}} = \frac{\dfrac{m_{water} c_{water} \Delta T_{45}}{\Delta t}}{\dfrac{m_{water} c_{water} \Delta T_{120}}{\Delta t}} = \frac{\Delta T_{45}}{\Delta T_{120}} \qquad \text{(A1)}$$

where ΔT_{45} and ΔT_{120} are measured temperature changes at 45 volts and 120 volts respectively, m_{water} and c_{water} are the mass of the water and specific heat of water respectively, and Δt is the run time. From the ratio, the power into the transducer at 45 VP_{45} was estimated at 2.5 W. Additionally, by considering the power leak from the

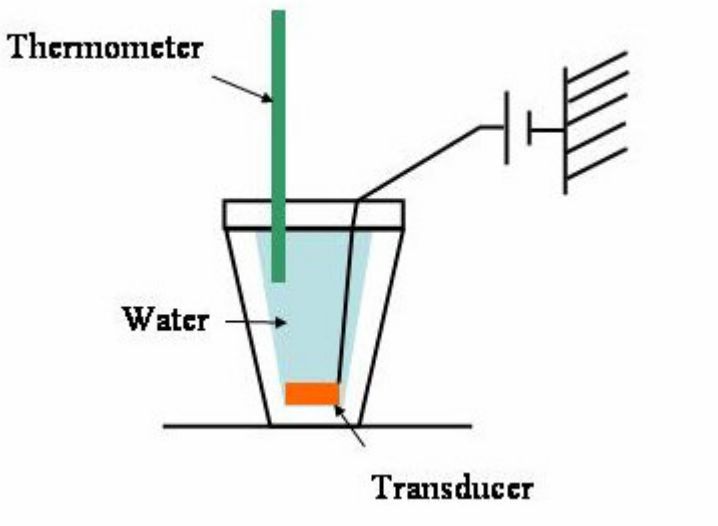

Figure A. 1 Cross sectional Schematic of Calorimeter. The water is contained and sealed inside a styrofoam cup to prevent heat loss.

transducer (estimated at 80 % by its manufacturer), the ideal power of 36 W given in the manufacturing specifications is re-adjusted and, therefore, P_{45} is reduced down to 0.5W.

The estimated power from the transducer was then adjusted by a wave interference theory at the solid and liquid interfaces. When the ultrasound wave encounters the interface of water and the solid surface (when it enters the assembly beaker) and then the interface of the solid and the mixture of water and

acetone (in the assembly beaker), some of the power is transmitted and the rest is reflected. This configuration was simplified here as a solid plate between two separate liquid media, and the transmitted wave was confined to one dimension. The transmitted power of the one-dimensional wave of the simplified configuration is given[40] as

$$P_t = \frac{P_{45}}{1+\left(\frac{2r}{1-r^2}\right)^2 sin^2\left(4\pi\frac{t}{2\lambda}\right)} \quad \text{(A2)}$$

where r is reflectivity at the solid and liquid interface, t is the thickness of the solid plate, and λ is wavelength of ultrasound wave. The reflectivity r is given as

$$r = \frac{1-v_1/v_2}{1+v_1/v_2} \quad \text{(A3)}$$

where v_1 and v_2 are the wave velocities of the two media involved at the interface. With the velocities of water and silica, which are 1453m/s and 6800 m/s respectively, r is estimated at 0.6479. The thickness of the solid plate was set to the sum of those of the template and the bottom plate of the assembly beaker, which is 1.36 mm. The wavelength λ of the wave in the solid medium is 3.9mm. With all the design parameters, the ratio of $\frac{P_t}{P_{45}}$ is estimated at 0.28.

Then, P_t is divided by the area of the bottom surface of the assembly beaker (3×10^{-4} m^2) to order to convert it to intensity (spatially unadjusted), I_o and then adjusted with a spatial distribution of intensity to obtain the local value of the intensity at the location of the pattern area of the template. The spatial distribution adopts the work by Jackson *et al.*[31] Based on the previous study,[31] the true power intensity I_{true} at the pattern area of the template was found to be only 20% of I_o, which is given by

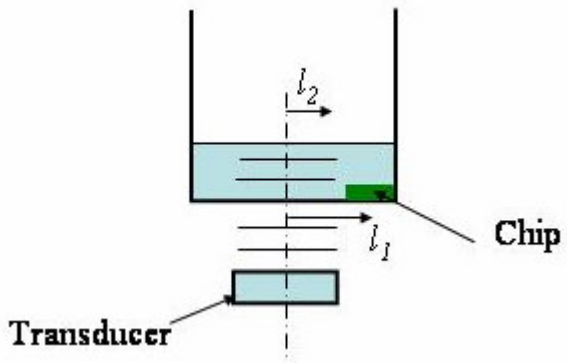

Figure A. 2 Schematic of the location of the pattern area, l_1, from the center of the assembly beaker and the location of the edge of the area directly driven by the ultrasound, l_2 from the center of the beaker.

$$\frac{I_{true}}{I_o} = \frac{1}{\pi^2}\left(ln\left(\frac{l_2 + l_1}{|l_2 - l_1|}\right)\right)^2 \qquad \text{(A4)}$$

where l_1 is 5mm and l_2 is 8 mm as shown in Figure A. 2. Then the true power intensity was input to the velocity calculation as shown above.